Synthesis and Characterisation of Nanocomposite Coatings for Antibacterial/Antifouling Applications

Thesis submitted in accordance with the requirements of the University of Liverpool for the Degree of Doctor in Philosophy by

Marios Michailidis

April 2018

Supervisor: Prof. Dmitry Shchukin

Contents

Abstract

Biofouling can occur everywhere water is present and is a major problem for a wide variety of materials and devices such as biomedical devices and implants, as well as industrial and marine equipment. After the ban of the efficient but environmentally harmful antifouling paints based on tributyltin, the creation of new, effective and low-toxic antifouling paints is a major challenge. The aim of this thesis is to develop novel modified nanoparticles (NPs) as functional fillers for low toxic and environmentally friendly antibacterial/antifouling coatings for mobile and stationary applications in maritime, hospitals, industries, etc. Application of mesoporous silica nanoparticles (MSNs) as antifouling/antibacterial carriers attracted a few attention so far, specifically with a dual synergetic effect. In the present work, MSNs modified with quaternary ammonium salts (QASs) and loaded with the active agent DCOIT were synthesized as functional fillers for antifouling/antibacterial coatings.

From the family of the MSNs, MCM-48 was selected as a carrier because of its cubic pore structure, high surface area, and high specific pore volume. Chapter 3 details the synthesis and characterisation of spherical MCM-48 MSNs with two different average sizes; 400 nm and 120 nm. As revealed from the X-ray diffraction and nitrogen isotherms, both types of MSNs showed highly ordered cubic mesostructure, high BET surface area, high pore volume and narrow pore size distribution. From the morphological studies using scanning electron microscopy and transmission electron microscopy, the MCM-48 with average size of 400 nm exhibited spherical morphology and some aggregates or fused together particles were present, while the MCM-48 with average size of 120 nm showed spherical morphology and all the NPs were monodispersed.

Chapter 4 documents the surface modification of MCM-48 NPs with two different types of QASs; dimethyloctadecyl[3-(trimethoxysilyl)propyl]ammonium chloride and dimethyltetradecyl[3-(triethoxysilyl)propyl]ammonium chloride. The QAS modified MCM-48 revealed strong covalent bonds between the QAS and the surface of the NPs. The surface functionalization was confirmed by diffuse reflectance infrared Fourier transform spectroscopy, thermogravimetric analysis, elemental analysis, and ζ-potential measurements. Additional loading of the QAS modified MCM-48 with a commercially available biocide (Parmetol S15) resulted in a synergetic dual antibacterial/antifouling effect. Either loaded or unloaded QAS-modified MSNs exhibited high antibacterial performance confirming their dual activity. In the case of the modified NPs with average size of 400 nm, the loaded QAS-modified MCM-48 (dual functionalised) killed all exposed bacteria after 3 h of incubation and presented 100% reduction at the antibacterial tests against Gram-negative and Gram-positive bacteria. Furthermore, the QAS-modified MCM-48 (single functionalised) presented 77−89% reduction against the exposed Gram-negative bacteria and 78−94% reduction against the exposed Gram-positive bacteria. Furthermore, spherical MCM-48 NPs with smaller average size of 120 nm were surface modified with the two types of QASs and tested against Gram-negative and Gram-positive bacteria in order to investigate if there is size-dependency at the antibacterial properties of silica-QAS core-shell NPs. The smaller sized modified

NPs showed increased antibacterial properties (83-94% reduction against Gram-negative bacteria and 87-97% reduction against Gram-positive bacteria) compared to their counterparts with average size of 400 nm implying that smaller size of modified NPs could provide better antibacterial properties.

In chapter 5, the modified NPs were homogeneously added in coating formulations. The nanocontainer-doped paints showed good distribution of the functionalised nanocontainers in the coating matrix, increased hydrophobicity and similar roughness values with the pristine coating formulation. In the antibacterial tests, the formulated paints revealed excellent antibacterial properties where all the bacteria were dead after 16 hours of exposure. Additionally, the nanocontainer-doped paints presented high anti-macrofouling properties against mussels. The paints containing the dual functionalised NPs presented 100% inhibition of mussels' attachment after 72 hours exposure of mussels in culture plates coated with the nanocontainer-doped paints. Furthermore, all of the nanocontainer-treated paints illustrated low toxicity against the Red Sea mussels *Brachidontes pharaonis* and the brine shrimps *Artemia salina*. Finally, PVC panels were coated with the formulated paints (containing either 2 or 5 wt % modified nanoparticles) and immersed in Red Sea (Eilat, Israel) for field test. After six months of exposure, the paints containing the NPs with dual effect showed significantly lower biofouling coverage (below 10%) compared to the biofouling coverage of pristine paint (50%) indicating their high antifouling properties in real sea water conditions.

The results of this work show that (i) the dual functionalised MCM-48 can be used as functional fillers for coating formulations providing excellent antibacterial/antifouling properties to the coatings, (ii) the dual functionalised MCM-48 can be used as environmental-friendly low-toxic alternatives for tin-based paints and (iii) the covalently attached QASs on the surface of the nanoparticles remain active even after complete release of the biocide, which considerably increases their functional lifetime in the coating formulations.

Acknowledgements

First of all, I would like to express my gratitude to my supervisor Prof. Dmitry Shchukin for his endless support, guidance and advice over the past 4 years of my PhD and for giving me the opportunity to develop not only as a scientist, but also as a person. Regardless his busy schedule, he was always there for me to give some good advice and make difficult and stressful situations to look simple and easy. I would also like to thank Dr Alexey Sergeev for agreeing to be my 2nd supervisor.

Many thanks to all these people of Shchukin's group over the past four years who were there to help me, provide training to equipment and have fun time in the lab: Paula, Zhaoliang, Mike, Maria, Daniel, Xiaolei, Claudia, Hongqiang, Lorena, Vicente, Mar, Yanli and Qian Bei.

During my PhD studies, establishing collaborations within EU BYEFOULING project, the University of Liverpool and other institutions across Europe was very critical and fruitful. Many thanks to Prof. Yehuda Benayahu, Dr Eldad Gutner-Hoch and Reut Wengier from Tel Aviv University for their help with the antifouling and toxicity tests, and the field test trial in Red Sea. Dr Rob Onderwater for his help with the antibacterial tests for the painted substrates. Dr Raechelle D'Sa and Dr Jenny Aveyard for providing me training and valuable help with antibacterial bio-assays in their facilities in the University of Liverpool. Prof. Rasmita Raval and Ioritz Sorzabal-Bellido for their assistance with testing antibacterial properties of our synthesised materials. Dr Heil Tobias and Dr Karl Dawson from the nanoinvestigation centre in Liverpool for their assistance with the FIB-SEM cross-section images and TEM images, respectively. Dr Dmitry Grigoriev from Fraunhofer institute in Potsdam-Golm, Germany for his assistance with the nitrogen isotherms for the mesoporous materials. Of course, I thank EU BYEFOULING project and ERC Consolidator grant Enercapsule for providing the funding to carry out my research and the University of Liverpool for providing good facilities and working environment.

During my PhD studies, I was lucky enough to work in a great environment as is the Stephenson Institute and meet great people and make good friends, thus I would like to thank all of them. Special thanks to my good friends who never said no to a nice cup of coffee, pint of beer after work or a lovely meal in order to discuss and share our thoughts and problems, and of course to have great fun: Apostolos, Christos, Ebenezer, Enzo, Eri, Giorgos, Iain, Ivan, Jose, Margarita, Pepe, Silvia, Spiros and Thanasis.

Ένα από τα πιο μεγάλα ευχαριστώ, θα ήθελα να το αποδώσω στους αγαπημένους μου γονείς Τάσο και Βέτα που όλα αυτά τα χρόνια έκαναν αμέτρητες οικονομικές, και όχι μόνο, θυσίες για να μην μου λείψει τίποτα στην ζωή μου και να καταφέρω να προοδεύσω και να σπουδάσω. Επίσης, ένα μεγάλο ευχαριστώ και στους "δεύτερους γονείς μου" Θάνο και Ευγενία για την αμέριστη αγάπη και υποστήριξη που μου έδειξαν όλα αυτά τα χρόνια και συνεχώς επιδίωκαν να επενδύουν στην εκπαίδευση μου.

Finally, my utmost gratitude goes to my beautiful fiancé and life partner Eva. Without you, I do not think that I would be in the position that I am today and it would be much more difficult to complete my thesis and cope with the difficulties of my life in general. Thank you for always supporting and standing next to me in every challenge of my life, listening my complaints and providing me a life full of joy and happiness for more than 10 years!

List of Figures

List of Tables

List of Abbreviations

^{1}H-NMR - Hydrogen nuclear magnetic resonance

alkynyl-poly(META) - alkynyl-functionalized 2-(methacryloyloxy)ethyl trimethyl ammonium chloride-based polymer chains

azido-poly(PEGMA) - azido-functionalized poly(ethylene glycol) methyl ether methacrylate-based polymer chains

BET - Brunauer - Emmett - Teller method

BF - bright field

BJH - Barrett-Joyner-Halenda

CDP - controlled depletion polymer coatings

CFU/mL – colony forming unit per mL

CMC - critical micelle concentration

CMT - critical micelle temperature

CO_2 - carbon dioxide

CP - cloud point value

CTAB - Hexadecyltrimethylammonium bromide

Cu_2O - dicopper oxide

DCOIT - 4, 5-dichloro-2-octyl-4-isothiazolin-3-one

DMOAP - dimethyloctadecyl[3-(trimethoxysilyl)propyl] ammonium chloride

DRIFT - Diffuse reflectance infrared Fourier transform spectroscopy

EG - ethylenglycol

ENPs - engineered nanoparticles

EPA - Environmental Protection Agency

EtOH - ethanol

FIB-SEM - Focused ion beam scanning electron microscopy

FSW - filtered seawater

H_2O - water

HAADF - high angle annular dark field

HK - Horvath-Kawazoe

IEP - isoelectric point

LB - Luria Broth

LbL - Layer-by-layer

LCST - lower critical solution temperature

LCT - liquid-crystal template mechanism

MCM - Mobil Crystalline of Materials

MIC - Minimum Inhibitory Concentration Determination

MSNs - mesoporous silica nanoparticles

NB - nutrient broth agar

NLDFT - nonlocal density functional theory method

NPs - nanoparticles

PBS - buffer solution phosphate-buffered saline

PEG - poly(ethylenglycol)

PNIPAAm - poly(N-isopropylacrylamide)

PVC - Poly(vinyl chloride)

QASs - quaternary ammonium salts

QC14 - dimethyltetradecyl [3-(triethoxysilyl) propyl] ammonium chloride

QC18 - Dimethyloctadecyl [3-(trimethoxysilyl) propyl] ammonium chloride

SEM - scanning electron microscope

SPC - self-polishing copolymer coatings

STEM - Scanning transmission electron microscopy

TBT - tributyltin

TEM - Transmission electron microscopy

TEOS - tetraethyl orthosilicate

TGA - Thermogravimetric analysis

XRD - X-ray powder diffraction

Chapter 1: Introduction

1.1. Definition of the problem; Biofouling

Biofouling is a natural process that refers to the accumulation and growth of microorganisms, algae or plants on any natural or artificial wetted surface.[1] The first establishment by microorganisms and unicellular algae occurs within the first minute of immersion of the surface in seawater.[1,2] This initial stage allows the formation of a conditioning film consisted of physically adsorbed organic molecules followed by the settlement and growth of bacteria, protozoa and diatoms creating a complex biofilm matrix within the first 24 hours of immersion (microfouling). The existence of this complex biofilm provides sufficient food for the formation of microscopically visible algae, spores, seaweeds and invertebrates after 2-3 weeks of immersion (soft macrofouling). Finally, the increased capture of microscopically visible organisms stimulates the settlement of larvae of marine organisms such as mussels, barnacles, and sponges as well as spores of macroalgae after several weeks of immersion.[3–5]

It is often stated that the surface colonisation follows a linear successional model (**Figure 1.1**). According to this model, everything starts with the formation of bacterial biofilm which is followed by the settlement of spores of macroalgae (seaweeds), fungi and protozoa. After several weeks, the colonisation process continues with the settlement of larvae of invertebrates such as barnacles and mussels.[5,6] However, this model is not accurate for every marine microorganism since some motile spores of seaweeds are capable to settle within minutes on a clean surface, while larvae of some species of barnacles or bryozoans are able to settle within a few hours of immersion.[1]

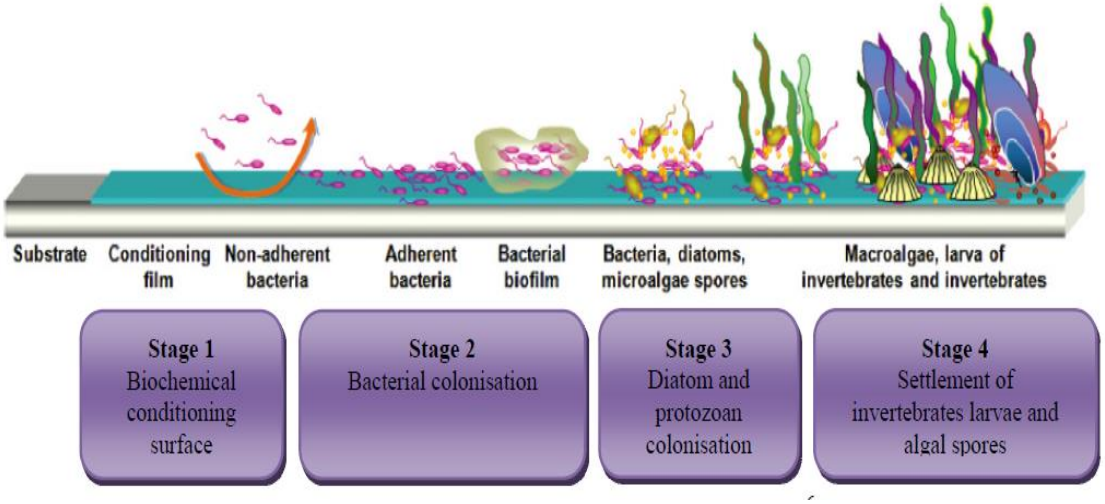

Figure 1.1. Colonisation process of marine fouling[7].

Even though, the above-mentioned timeline is an acceptable overview of the colonisation process, there is not a universal agreement for type of species attached and the precise timeline of the settlement.[4] This could be explained from the influence of various sea water features such as temperature, pH, salinity, dissolved salts and oxygen concentration on the fouling of immersed solid surfaces.[8] There is a big variation on the species and their attachment time depending on the location, as the environmental conditions such as the temperature, salinity, density of ocean water and nutrients can vary from place to place. Even if the location remains the same, the fouling colonisation process can change with the season due to differences in the temperature of the water and variations in the daylight irradiation.[9] This justifies the diversity of fouling in different areas of the globe, as well as why equatorial and tropical regions are richer in certain species in comparison with other

colder regions. Furthermore, it is estimated that more than 4000 different fouling organisms have been identified in the oceans on fouled structures. Because the diversity of fouling organisms is vast and the range of adhesion mechanisms is correspondingly broad, creating an effective fouling resistant coating is a real challenge. This huge diversity of species, together with the influence of the environmental conditions on different geographical locations, render biofouling as a global issue that needs to be addressed.

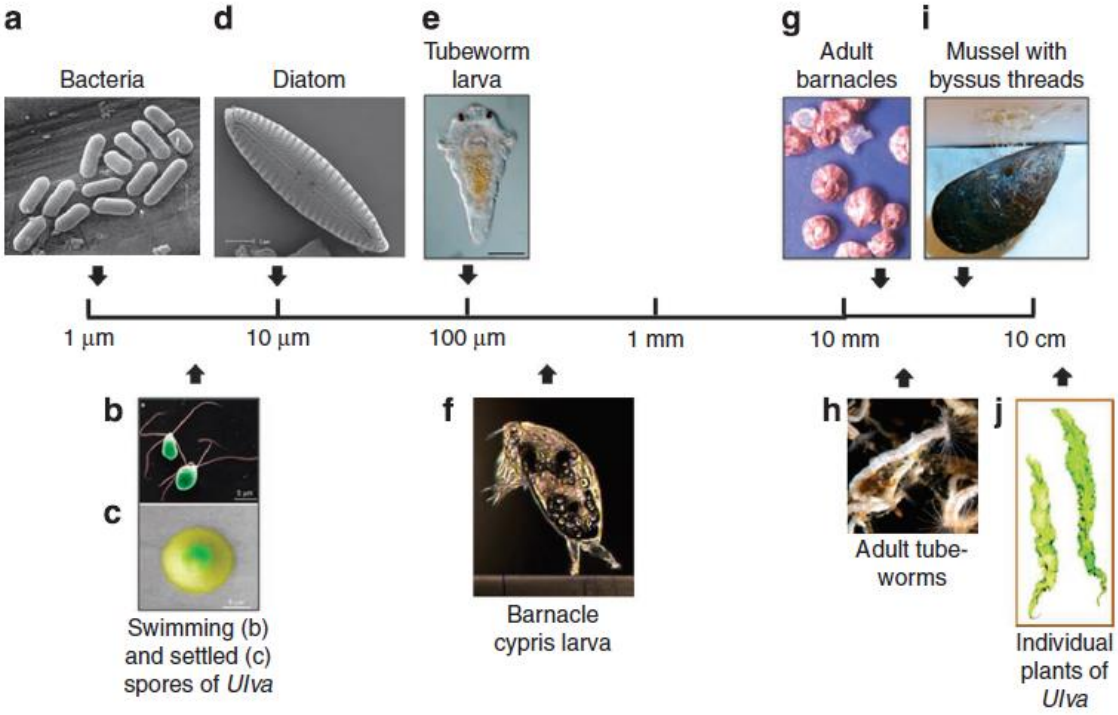

Figure 1.2. Diversity and size scales of a range of representative fouling organisms. (a) Bacteria, (b) swimming spores of the green alga (seaweed) *Ulva*, (c) settled spore of *Ulva*, (d) diatom *Navicula*, (e) larva of tube worm *Hydroides elegans*, (f) barnacle cypris larva *Amphibalanus amphitrite*, (g) adult barnacles, (h) adult tubeworms *H. elegans*, (i) adult mussels showing byssus threads attached to a surface, (j) individual plants of the green alga (seaweed) *Ulva*. The diagram intends to indicate relative scales rather than absolute sizes; individual species within a group can vary significantly in absolute size.[1]

1.2. Impact of biofouling

Biofouling in the maritime milieu can result in severe economic disturbances to the marine industries, as well as in a negative environmental impact. Biofouling is estimated to cost US$ 150 billion annually, a cost that is a result of the maintenance and cleaning of submerged man-made surfaces on buoys, membrane bioreactors, desalination units, cooling water systems and oil pipelines.[10,11] It also constitutes a significant problem for all the aquaculture industry, the broadest and the most documented impact being in marine finfish aquaculture, in particular sea cage-based aquaculture. The settlement of marine invertebrates on the hulls of ships results in increased erosion, reduction of speed, increased fuel consumption and therefore increased air pollution and CO_2 production. Most of the structural materials used in maritime industry are metals/metal alloys and therefore bio-corrosion (also called microbially influenced corrosion, MIC), which is a result of metal degradation due to the presence of biofilms at coating/solution interface, may occur. Microbial activity within biofilms can intervene in the kinetics of redox reactions associated with corrosion at the metal substrate and modify the chemistry of the protective layers. In spite of extensive studies over the past 50 years and several proposed models intended to explain the mechanisms governing MIC, the details are still poorly understood.[12] The following sections outline the consequences of biofouling on the different areas of maritime industry.

1.2.1. Biofouling impact in maritime transportation

Transportation is necessity for all business activities and despite the presence of on land and air transport, big part of the foreign trade in Europe and other continents is conducted by sea using bulk containers as carriers. Owing to increased international trade, due to the transportation of goods, the environmental impacts of sea transportation are becoming increasingly important. During the transportation of products by ships, the protection of the ship's hull from the growth of a vast range of marine organisms constitutes a major issue.

Figure 1.3 shows examples of heavily fouled ship hulls, which have become rough due to the growth of algae, barnacles, seaweeds, etc. One of the parameters that influence the energy consumption of a vessel is the condition of the underwater hull, which can affect significantly the total ship resistance. In general, biofouling on hulls increases the hydrodynamic volume of a vessel and the hydrodynamic friction during the movement through water.[13] Consequently, the maximum achievable speed is decreased and is accompanied by 40% increase in fuel consumption. This additional fuel consumption in turn promotes the emission of harmful compounds such as CO_2, SO_x and NO_x into the environment.[10] It is estimated that the total emissions from international shipping constitutes 2.7% of the global CO_2 emissions.[14]

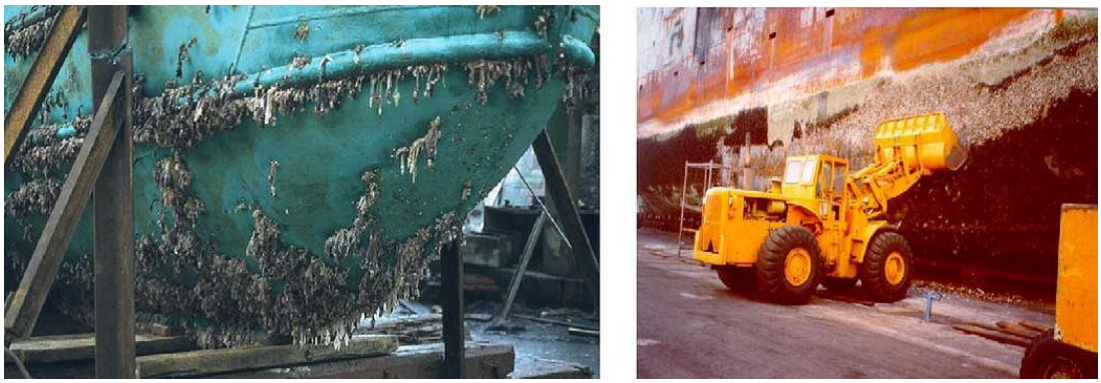

Figure 1.3. Examples of heavily fouled ship hulls.[15]

Furthermore, the biodiversity and ecology of sensitive marine environments can be severely affected by the marine organisms which are attached on the ship hulls, during the transportation from sea to sea, thus invading the habitat of native species. A similar issue can be caused by the ballast water, which is used by cargo vessels and passenger ships to increase their stability and decrease the centre of gravity during sailing. These commercial ships carry enormous amounts of seawater for ballasting between their voyages; these vessels usually load and unload the water ballast, which is rich in biological material at each port of call. The ballast water is naturally populated with several animals, bacteria, plants and viruses which are non-native or exotic and can thus invade the habitat of native species.[16]

1.2.2. Biofouling impact in marine aquaculture

Aquaculture constitutes an industry of global importance, as it provides essential protein food supplies to a growing world population, especially to countries with low

income. Some of the most common cultivated marine shellfish in aquaculture include oysters, scallops and mussels, while the most common cultivated marine fish are salmons, tunas, mullets, sea basses and sea breams. The production of all these marine species requires the use of a complex assortment of submerged man-made constructions such as cages, nets, floats and ropes.[17] Biofouling in open sea fish-farming can induce high maintenance costs and reduced return-on-investment, since the preservation of the normal operation of the fish farm requires strenuous control and expensive clean up routines. It is estimated that 5-10% of the production cost in aquaculture industry is associated to biofouling control.

Figure 1.4. Common fouling organisms associated with aquaculture operations: (A) *Ciona intestinalis* (vase tunicate); (B) *Ectopleura crocea* (pink mouthed hydroid); (C) *Mytilus edulis* (blue mussel); (D) *Ectopleura larynx* (ringed tubularia).[11]

Biofouling growth in the fishnets quickly leads to the blocking of the nets opening, which in turn can cause a restriction of the water exchange with the surrounding environment. Therefore, the biofouling of the fishnets results in: poor quality of water inside the nets, reduced level of oxygen-rich water into the fish enclosure and reduced waste elimination from the cage to the surrounding environment. All these negative effects from the occlusion of the fishnet openings can lead to reduced growth performance in the fish, increased mortalities, increased disease risk and generally reduced well-being of the fish.[18–20] Moreover, biofouling growth can increase significantly the weight and drag of the nets, thus affecting the structural integrity of the fish farm and limits its ability to cope with extreme weather conditions.[21] Additionally, there are several effects of biofouling on marine shellfish aquaculture. For example, growing of biofouling can take place on the shell of shellfish causing physical shell damage. Fouled shellfish are visually unattractive for consumers and are subsequently devalued or discarded, leading to economic loses for the growers. In extreme cases, shellfish become vulnerable to fouling parasites experiencing severe shell damage and mortality.[11] Furthermore, shellfish are experiencing biological competition with the fouling species for food and space inside the sea cages. Both shellfish and fouling organisms are primarily filter feeders, thus limitation of food resources in fouled sea cages can lead to reduced growth of shellfish and decreased product value for the growers.[22] In general, controlling biofouling in fish and shellfish farming is very challenging and expensive; routine checks and cleaning are essential tasks, as well as the replacement of fish nets and structural components of the aquacultures.

1.2.3. Biofouling impact in marine sensors and floating devices

During the last 30 years, many marine sensors and floating devices have been developed, in order to monitor and collect data for: the calibration of satellite observations, the assessment of the coastal water quality and the real-time monitoring of aquatic species for fishing vessels. Most of these devices are surface buoys equipped with sophisticated sensing equipment, which is subject to fouling problems.[23] The satellite buoys are also exposed to adhesion of fouling: (i) on the bottom part, which lowers the efficiency of the integrated sonar and sensors by lowering the buoy into the water and (ii) on the upper part, which results in reduced solar panel efficiency.[24] These buoys are designed to drift in the open sea, but the adhered fouling on their bodies decreases their speed resulting in slower control of the areas to be screened. Furthermore, the marine buoys are equipped with antennas for communication purposes and can lose efficiency if water mass is present between the dome of the buoy and the air. A loss of communication makes the recovery of the buoy impossible.[25] Subsequently, the loss of the buoys can lead to two types of economic loss: the buoy-owners have to replace the lost equipment and valuable information recorded during the exposure period of the buoy will be lost.

1.3. Antifouling strategies

1.3.1. Historical development of antifouling systems from ancient years to 19th century

The problem of biofouling had been recognised since ancient years as humankind started using ships as means of transport. The early Phoenicians and Carthaginians are credited to be the first who used pitch and possibly copper sheathing for the bottom of their ships since 700 B.C. in order to prevent biofouling.[26,27] Later in the 3rd century B.C., ancient Greeks and Romans used wax, tar and lead sheathing for their ships. When lead sheathing was used, copper or gilt nails were used to attach it to the ship's hull.[15,26] Several centuries later, the Vikings of the 10th century were using a "seal tar" to protect their ships from sea worms. Between 13th and 15th centuries, pitch was commonly used and sometimes was mixed with tar, oil, resin or tallow. The great Venetian fleets were using tar for their ship hulls during the 15th century, while another example comes from Columbus's ship that its bottom may have been covered with a mixture of tallow and pitch in the hopes of discouraging barnacles and shipworms.[26] Another example of biofouling prevention comes from the time of Vasco da Gama (1469-1524) where the Portuguese used to char the outer surface of their ship's hull to a depth of several inches. The British adapted a similar concept two centuries later, in 1720, and they built at least one ship (the *Royal Williams*) entirely from charred wood.[26]

A usual procedure during the early 16th century was the wooden sheathing, put on over a layer of animal hair and tar. Although the building cost of the ships was

significantly increased, it was reported to prevent sea worms from penetrating to the planking. However, during that time and prior to the 18th century, lead sheathing was perhaps the material most frequently used for the protection of ships' hulls. In spite of its corrosive action and poor antifouling performance, lead sheathing was good enough to protect the wooden ship hulls against the threat of ship worms.[15,26,28] The lead sheathing was adopted widely from England, Spain and France during that period but it was abandoned officially from the British Admiralty in 1682 due to its corrosive effect on iron components of the ships.

The first successful antifouling surface that received general recognition was copper sheathing. The first certain use of copper in ships was used from the Phoenicians as bronze-shod rams for their warships and as fastenings in the Greek and Roman ships. Although, there is no clear evidence that it was used as sheathing on ships' hulls. The first evidence for the use of copper as antifouling compound comes from the British patent of William Beale in 1625 by using a mixture of cement, powered iron and probably some form of copper (copper sulphide or copper arsenic).[15] In spite these first evidence of copper's antifouling properties, the first authenticated use of copper as sheathing was reported on a conducted experiment from the Royal Navy in 1759. A 32-gun frigate named *HMS Alarm* was sheathed with copper and sailed for a voyage to West Indies. Upon her return to England, the ship hull was clean, and as good as when the ship started its journey.[26] In the following years, copper was widely used throughout the British Navy and was followed by the United States Navy.

After the establishment of the iron ships at the beginning of the 19th century, the use of copper sheathing in direct contact with the ship's hull was abandoned. The two main reason was that the antifouling performance of the copper sheathing had corrosive effect on iron. In the following years, many copper-alternatives were tried such as muntz metal, galvanised iron, sheet lead, nickel, as well as alloys of lead and antimony, and of zinc and tin but most of them never passed beyond the experimental stage. Non-metallic alternatives were also tried as insulators between the iron hulls and the copper sheathings, including canvas, rubber, cork, paper and wood. All these problems related to iron ships, eventually led to the development of the modern paint systems with antifouling compositions. Some early attempts for development of antifouling paints were based on the idea of toxicants/antifoulants in polymeric matrixes. At that time, popular antifoulants were copper oxide, arsenic and mercury oxide. Solvents could include naphtha, turpentine oil and benzene, while common binders were linseed oil, tar, shellac varnish and several types of resins.[15]

1.3.2. Biocide-realising antifouling paints

Historically, the most successful antifouling paints were biocide-based self-polishing coatings based on the well-known organotin compounds, especially tributyltin (TBT), a biocide with wide application for wood preservation, antifungal applications in industrial processes and marine antifoulings. Unfortunately, due to its high toxicity on humans and the negative environmental impact led to the worldwide direct banning of the TBT compounds usage by the International Maritime

Organisation in 2008.[28,29] Therefore, the antifouling paint manufacturers have been forced to study and develop TBT-free environmentally friendly antifouling paints. Past established biocides such us copper which is known for its antifouling properties since 300 B.C. from the ancient Greeks and Romans were resurrected and the current functioning of the most antifouling paints is based on copper as the main component of tin-free alternative biocidal compounds.[30] The biocide-releasing antifouling paints can be divided in three main categories: contact leaching coatings, controlled depletion polymer coatings (CDP) and self-polishing copolymer coatings (SPC).[7] All of these technologies are based on the same objective; controlled and slow release of bioactive molecules incorporated in a polymeric matrix.

1.3.2.1. Contact leaching coatings (insoluble matrix paints)

This type of antifouling paints rely on insoluble polymeric matrixes in seawater which are made of polymers with high molecular weight such as acrylics, epoxy, vinyls or chlorinated rubber polymers.[15] These type of paints have high mechanical characteristics and high amount of toxicants and active molecules can be incorporated. As the active compounds are released to the surrounding environment, seawater penetrates in the created pores from the empty space and goes on deeper to dissolve more active compounds (**Figure 1.5**). As the active compounds are deeper, in the insoluble matrix, it is harder for them to be released and, as a result the release rate is getting slower and slower. After certain time, the release rate of the active compounds becomes lower than the minimum value required in order to provide the

necessary antifouling protection.[31] Therefore, the main disadvantage of this type of paints is their short lifetime, typically ranging between 12 and 18 months.[4]

1.3.2.2. Controlled depletion polymer coatings (soluble matrix paints)

Controlled depletion polymer coatings are soluble matrix paints which contain biocides mixed with non-toxic seawater-soluble binders. Usually, these paints are formulated using a blend of natural rosin obtained from the exudation of pine and fir trees, and man-made synthetic resin.[32] They are partially soluble, meaning that as sea water passes across the surface of the coating, the soluble binder and the incorporated biocide are dissolved and released simultaneously. The physical action for water over the surface of the paint steadily reduces its thickness providing a continuous availability of fresh biocide on the surface. Therefore, the lifetime of these coatings strongly depends on the thickness of the applied paint.[3] Typically, the main binder of these systems is the natural rosin which dissolves relatively fast, thus the CDP paints are reinforced with synthetic organic resins which are more resistant than rosin derivatives and control the hydration and dissolution mechanism of the soluble binder.[7] The lifetime of this type of coatings is usually three years and they are widely used on leisure boats and small ships.[28] The main disadvantage of these systems is that by increasing the speed of the vessel, the erosion of the paint can increase exponentially.

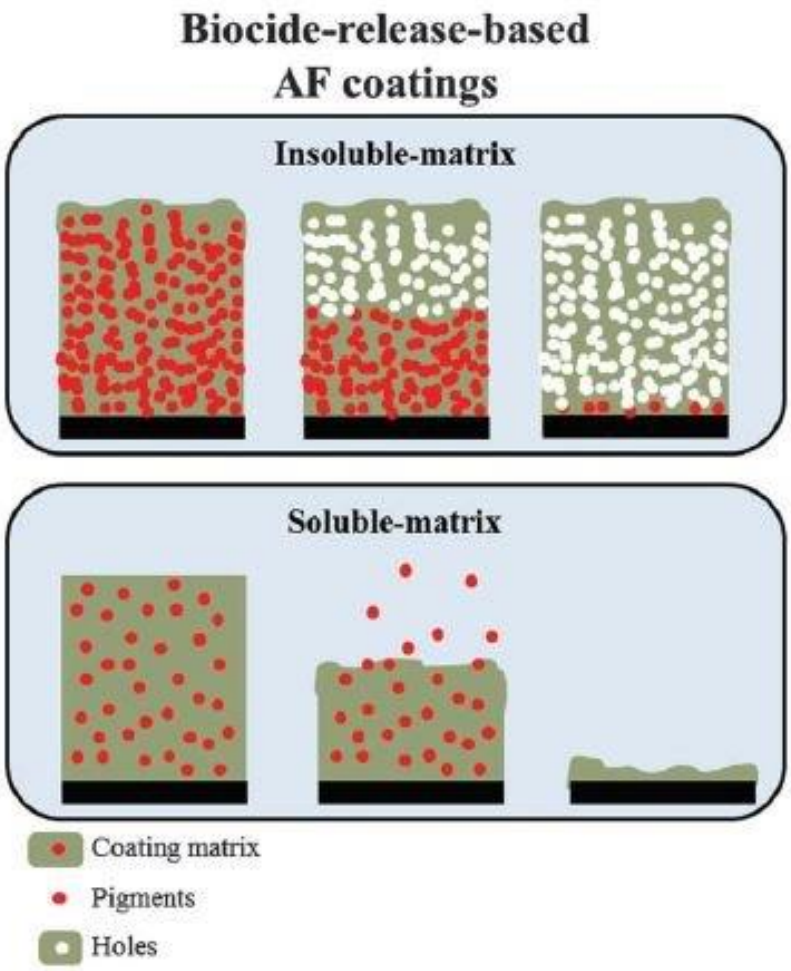

Figure 1.5. Schematic illustration of antifouling coatings based on biocide-release approach, for soluble and insoluble matrixes.[4]

1.3.2.3. Self-polishing copolymer coatings

The SPC coatings are based on acrylic and methacrylic copolymers that can be easily hydrolysed in sea water.[5] The advantage of these coatings is that the releasing rate of the incorporated biocide in the copolymer matrix can be controlled through controlling the erosion rate of the binder.[33] The SPS coatings contain less biocides than CDP coatings and they are usually less toxic. Furthermore, SPC coatings have a

more controlled release of biocides over time which reduces the risk of fouling, and increases their lifetime efficiency, normally up to 5 years. Therefore, the vast majority of paint manufacturers nowadays are producing mainly SPC coatings. Even if a certain amount of biofoulers will attach on the SPC coating surface, they will be eliminated together with the binder during its decomposition by hydrolysis. This type of paint was designed to mimic the antifouling activity of TBT-SPC paints. The TBT-free SPC coatings are using copper, silicon or zinc-based ester moieties instead of the toxic TBT-ester groups. Nevertheless, none of these products can fully mimic the activity of the banned TBT-SPC coatings since none of them provides the same biocide release mechanism.[15]

1.3.2.4. Active compounds: Biocides

After the ban of the effective TBT-based biocides, the most common alternatives are using copper-based compounds. Among them, the most cost effective and widely used biocide is dicopper oxide (Cu_2O) which is effective against a broad range on fouling organisms, especially those related to hard fouling. Therfore, dicopper oxide is usually supported from other booster biocides which are more effective against slime and algae.[3] In contrast with the high toxicity of TBT-based compounds which have been shown to bioaccumulate with a high dentrimental effect on non-target organisms and the surrounding environment, the toxicity of copper is about ten times lower, but it is still a controversial issue in the scientific community.[34] There are several reports in the literatue indicating the toxicity of copper on non-target species and its use in antifouling paints can increase the level of copper in shellfish such as

mussels and oysters.[35,36] Major attention has been received from the active biocidal compounts due to their potential to cause adverse effects, as a result all the biocide-releasing antifouling paints are currently regulated and require approval.[7]

There are several reviews in the literature providing information for the most widely used biocides in the antifouling systems and their potential toxic effects for the environments and several living organisms.[35,37–39] **Figure 1.6** shows a list of common biocides currently used in antifouling coatings. A good biocide should be able to provide high efficiency in preventing biofouling on the exposed surface and, at the same time its concentration in the paint should not be high enough to cause dentrimental environmental effects.[38]

The last years, particular attention has been paid in the identification of natural products that could act as biocides/antifoulants. There are several marine organisms that are equiped with physical or chemical defence mechanisms against fouling.[40] The chemical antifouling mechanism of marine organisms occurs through the production of natural products such as secondary metabolites which deter foulers.[5] Isolation of these bioactive secondary metabolites could lead in the development of new eco-friendly biocides. These natural products could be extracted compounds from marine organisms such as seaweed, aquatic plants, algae, invertebrates and several marine bacteria.[41]

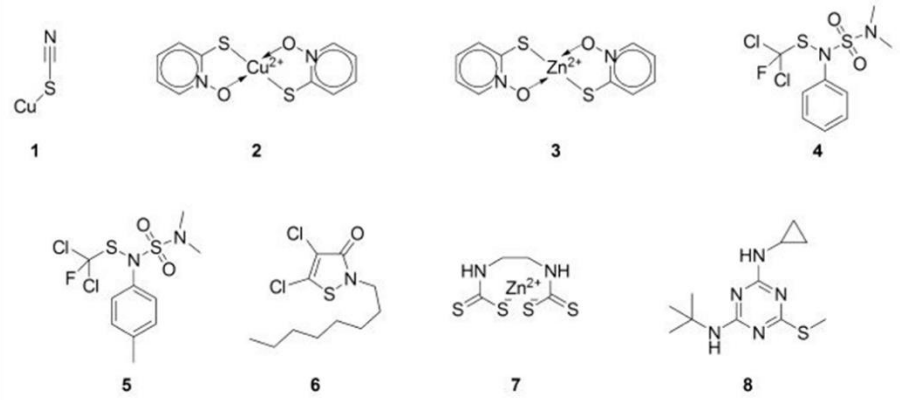

biocide	alternative name
copper	
dicopper oxide (cuprous oxide)	
copper thiocyanate 1	
bis(1-hydroxy-1H-pyridine-2-thionate-O,S) copper 2	copper pyrithione
zinc complex of 2-mercaptopyridine-1-oxide 3	zinc pyrithione
N-dichlorofluoromethylthio-*N*′,*N*′-dimethyl-*N*-phenylsulfamide 4	Dichlofluanid, Preventol A4S, Euparen
N-dichlorofluoromethylthio-*N*′,*N*′-dimethyl-*N*-*p*-tolylsulfamide 5	Tolylfluanid, Preventol A5S Euparen M
4,5-dichloro-2-*n*-octyl-4-isothazolin-3-one 6	Sea-Nine 211, Kathon 287T, Kathon 930, DCOIT
zinc ethylene bisdithiocarbamate 7	Zineb
N′-*tert*-butyl-*N*-cyclopropyl-6-(methylthio)-1,3,5-triazine-2,4-diamine 8	Irgarol 1051, Cybutryne

Figure 1.6. Main biocides used in antifouling paints.[3]

1.3.3. Not-biocide-releasing antifouling paints

The not-biocide-releasing antifouling coatings usually referred in the literature as fouling-release coatings too. The main idea behind this type of coatings is to design foul-release coatings in order to prevent adhesion of microorganisms by providing moieties with desired functionality at the surface that will have low-friction and ultra-smooth surface. The two main strategies for these coatings rely on the development of coatings that can prevent attachment of biofoulants and the detachment of biofoulants from hydrophobic surfaces with the help from the shear flow caused by the movement of the ship (**Figure 1.7**).[4]

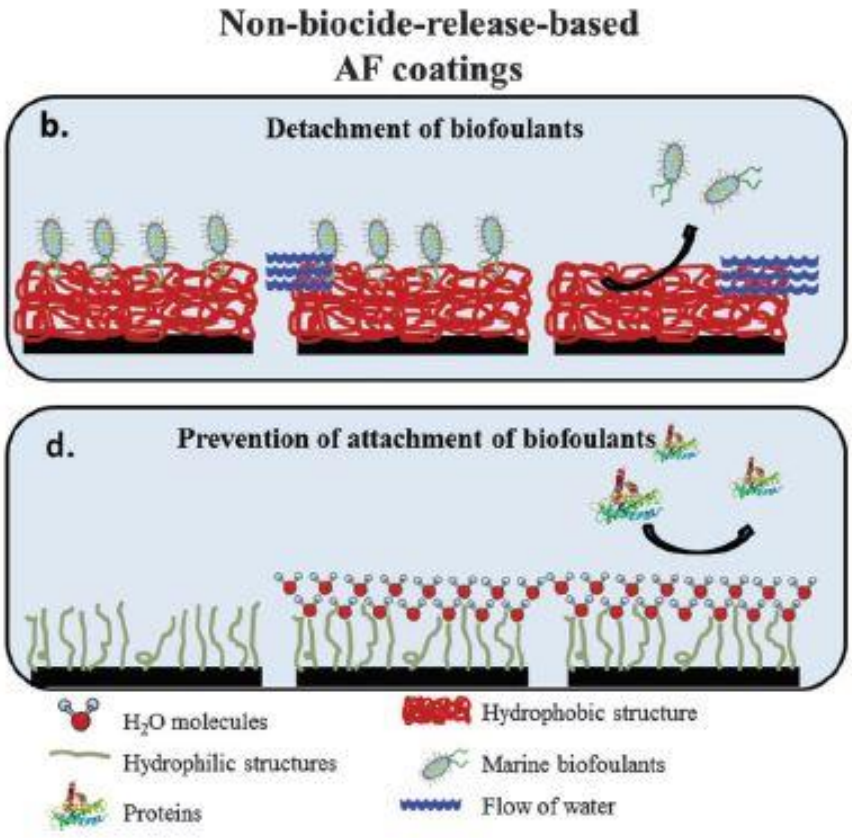

Figure 1.7. Schematic illustration of antifouling coatings based on non-biocide-release approach.[4]

Historically, the foul-release coatings were developed almost simultaneously with the SPC coatings but they attracted less attention because they were less effective and more expensive to produce. As reported by Brady[42], the main properties of these antifouling coatings in order to be efficient are:

- Flexible and linear backbone
- Sufficient number of surface-active groups to impact a surface energy in the desired range

- Low elastic modulus
- Smooth surface at the molecular level to avoid infiltration of biological adhesives
- High molecular mobility in the backbone and surface-active chains
- Physical and chemical stability for prolonged periods in the marine environment

These properties can be found in two families of materials: fluoropolymers and silicones. Therefore, the not-biocide-releasing antifouling coatings are mainly based on these two materials.

1.3.3.1. Fluoropolymer-based materials

This type of material form non-porous, very low surface-free energy surfaces with very good non-stich characteristics.[43] They have two main disadvantages: the fluorine atoms make the coatings very stiff and once fouling microorganisms are settled, it is very difficult to remove them. The first fluoropolymers that were used as coating components were poly(tetrafluoroethylene) and fluorinated ethylene-propylene copolymers for the protection of ship hulls.[44] The materials presented unique properties such as similar coefficient of friction with Teflon, very high hydrophobicity, UV resistant and provided abrasion resistance four times higher that Teflon.

1.3.3.2. Silicone-based materials

The silicone-based materials can improve the non-stick efficiency of fluoropolymers but, at the same time they have a few drawbacks: the short chain silicones can be released to the water, their service life is significantly lower compared to biocide-based products and their prices are higher. The first use of cross-linked silicones as marine fouling release coatings was reported in the patent of Robbart in 1961.[45] This invention was based on the discovery that the settlement of barnacles could be largely avoided with a surface coating composed of a silicone resin. Most of the used materials are based on poly(dimethylsiloxane) coatings.

1.4. Dual-effect antibacterial/antifouling surfaces

As we discussed in the previous section, the commercially available antifouling coatings currently on the market are either biocide-releasing or not-biocide-releasing based antifouling coatings.[4] Both of these systems present inherent advantages and disadvantages. For instance, the not-biocide-released antifouling coatings can prevent, inhibit or reduce the initial attachment of bacteria and the formation of biofilms, but without achieving 100% efficiency. On the other hand, the biocide-releasing coatings are more effective but their antifouling activity is diminished during their lifetime and there are several issues related to their ecotoxicity.[7,46] In addition, the biocides are directly incorporated and dispersed molecularly in the polymer matrix of the coating. Normally, there is a premature depletion of the active compound to the surrounding environment resulting in short antifouling action of the coatings. In order to maintain the antifouling activity of the coating for longer

period, excessive amount of biocide is required which may pollute the marine environment, harm non target species and affect the mechanical properties of the coating.[47] An effective methodology to address this problem is the encapsulation, a technique that has been used successfully in the past for drug delivery, biomedical systems, protection against corrosion and energy storage systems.[48–53] Encapsulation provides a methodology to decrease and control the release rate of the biocides and, at the same time, protect them from the surrounding environment.[54–57]

An ideal antibacterial/antifouling surface should be able to: prevent attachment of microorganisms, kill microorganisms that managed to attach and remove the dead microorganisms from its surface. During the last two decades in an effort to find ideal antibacterial/antifouling surfaces, researches were focused on the development of multifunctional, usually dual-functional, surfaces that combine effective operating principles from single functionalised systems into one system.[58,59] According to these recent advances, the antibacterial/antifouling surfaces with dual effect based on the combination of surfaces with single effect can be divided in two main categories: surfaces that can kill and resist, and surfaces that can kill and release.[58]

1.4.1. Antibacterial/antifouling surfaces that can kill and resist

This type of surfaces are inspired from single functionalised systems with bactericidal and bacteria-resistant properties. Dual action “kill and resist” surfaces are based on the incorporation of biocidal compounds into non-fouling materials and they can be divided in the following three categories.

1.4.1.1. Biocidal compounds tethered to hydrophilic copolymers

For several years, the interactions between polymeric surfaces and organisms have been the focus for many studies. Proteins have a key role in these interactions as they can determine the biocompatibility of polymers.[60] Hydrophilic polymers have been widely used as biofunctional surfaces through the immobilisation of bioactive molecules. They can provide: antifouling protection to surfaces since they resist non-specific protein interactions preventing bacteria adhesion and increased accessibility to active biocidal compounds through surface modification.[61,62] In recent years, several surfaces with both bactericidal and bacteria-resistant properties were developed based on hydrophilic polymers.

The most widely used non-fouling hydrophilic polymer is poly(ethylenglycol) (PEG). PEG molecules can be immobilised on polymeric substrates and several antibacterial or antibiotic compounds can attach to their terminal groups.[61] Therefore, the antibacterial surfaces will provide dual action, the first action from the attached active compound on the terminal groups and the second action from the PEG molecules.[63] By using PEG molecules with different terminal groups, different types of active compounds can be attached simultaneously.[64] The main problem of this systems is the decreased number of attached active compounds since each immobilised PEG molecule on the substrate has only one terminal group to offer. Some studies tried to solve this problem by using comb-like polymers with several side chains containing ethylenglycol (EG) units.[65,66] In addition, PEG molecules have been also used to surface modify polymeric substrates with incorporated silver nanoparticles. The resulting coating had a dual effect: antimicrobial silver ion release system and microbe-repelling surface.[67]

1.4.1.2. Layer-by layer alternated deposition of nonfouling and antibacterial layers

Layer-by-layer (LbL) deposition is a simple and low-cost technique in order to attain additional functionality to delivery systems.[68] The technique is based on step-wise adsorption of various components (polyelectrolytes, nanoparticles, proteins, enzymes, etc.) as the layer growth is governed by their electrostatic attraction and allows the formation of multilayer shells with nanometer (thickness) precision (**Figure 1.8**).[69] Over the past years, LbL deposition has been extensively used for encapsulation purposes in drug delivery systems and more recently for loading and triggered-releasing antibacterial agents.[70–74] This method can be used to synthesise dual functionalised surfaces by physically adsorbing antibacterial and anti-adhesive compounds with opposite charges onto substrates.

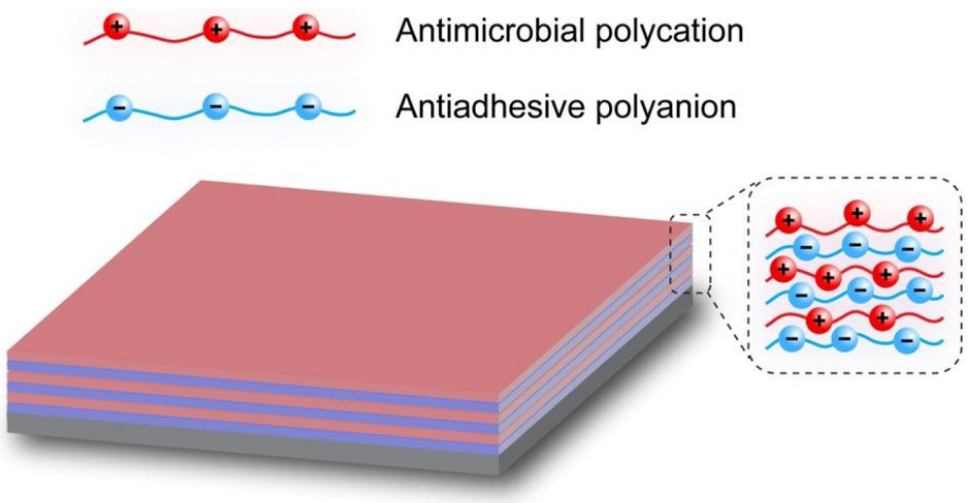

Figure 1.8. Schematic illustration of multilayer film containing antibacterial agents and anti-adhesive agents prepared by the LbL method.[58]

In a typical approach based on LbL method, according to Follmann *et al.*, dual functional antibacterial surfaces were developed when chitosan (cationic antibacterial agent) and heparin (anionic antiadhesive agent) were alternately deposited on modified polystyrene films.[75] In the antibacterial tests against *E. coli* bacteria, the modified polystyrene films showed effective antiadhesive properties and reduced the number of viable bacteria dramatically. In another approach to combat marine biofouling using the LbL method, fouling resistant azido-functionalized poly(ethylene glycol) methyl ether methacrylate-based polymer chains (azido-poly(PEGMA)) and antimicrobial alkynyl-functionalized 2-(methacryloyloxy)ethyl trimethyl ammonium chloride-based polymer chains (alkynyl-poly(META)) were click-assembled layer-by-layer via alkyne-azide 1,3-dipolar cycloaddition on stainless steel coated with polydopamine.[76] The polymer multilayer coatings were resistant to bacteria adhesion and show high antibacterial properties against marine bacteria.

1.4.1.3. Antibacterial agents released from nonfouling surfaces

It is well known that surfaces based on the contact-killing mechanism can effectively kill deposited bacteria on them but their antibacterial activity is limited against planktonic bacteria. On the other hand, antibacterial surfaces that are able to release antibacterial compounds are extremely effective against planktonic. To combine these two effective approaches in one material, zwitterionic hydrogels with releasable antibacterial agents were developed for biomedical applications.[77–80] According to this approach, a mild antibacterial agent (salicylate, anionic compound)

is added into a positively charged ester hydrogel as its anionic counter ion. Because of hydrolysis reactions, the anionic antibacterial agent is released to the surrounding environment. When the anionic antibacterial compound is completely released, the positively charged zwitterionic compound will continue to provide antibacterial properties.[77] Further improvements to this approach, in order to decrease the fast release of the antibacterial agents during the hydrolysis, were achieved by covalently attaching the antibacterial agents into the polymer matrix via hydrolysable linkers.[78]

1.4.2. Antibacterial/antifouling surfaces that can kill and release

These type of surfaces are inspired from single functionalised systems with bactericidal and bacteria-release properties, and they are combining both approaches into one system. One of the main problems that the bactericidal surfaces have to overcome is the accumulation of dead bacteria on their surface. This accumulation can both decrease their biocidal effectiveness and provide nutrients to other bacteria for colonisation. Therefore, it is highly favourable for the antibacterial surface to have the capability to release or remove dead bacteria. Most of the dual functionalised surfaces that can kill and release bacteria rely on two basic types of polymers; pH-responsive and temperature-responsive.

1.4.2.1. pH responsive antibacterial surfaces with dual action

The pH responsive antibacterial surfaces with the dual action are capable to chemically switch from a cationic antibacterial form to a zwitterionic nonfouling

form that can release/repel attached dead bacteria.[58] A characteristic example is illustrated in **Figure 1.9 a**. Initially, the polymeric surface is modified with a cationic quaternary ammonium compound which provides high antibacterial properties. After hydrolysis in basic or neutral aqueous environment, the polymeric surface switches to a zwitterionic nonfouling surface and releases dead bacteria. Moreover, the resulting zwitterionic surface can further prevent the attachment of proteins and microorganisms and reduce the formation of a biofilm on the surface, as the authors stated in the original publication.[81] The main drawback of this method is that the transition between cationic and zwitterionic forms can happen only once, thus it can be used only for disposable devices. In order to achieve renewable kill and release effect based on the same principle, the same research group developed a polymer that is capable to switch reversibly between cationic and zwitterionic forms in response to pH change (**Figure 1.9 b**).[82] The developed polymer is capable of switching repeatedly between its two equilibrium states, a cationic N,N-dimethyl-2-morpholinone (CB-Ring) and a zwitterionic carboxy betaine (CB-OH). When the CB-ring is formed, the polymeric surface provides strong biocidal activity from the cationic compound. After hydrolysis in basic or neutral pH, the polymeric surface is capable to release the dead bacteria because of the existence of the zwitterionic compound. The main limitation of these surfaces is that the bacteria should be attached while it is dry. Therefore, this operating principle can work only for airborne bacteria.

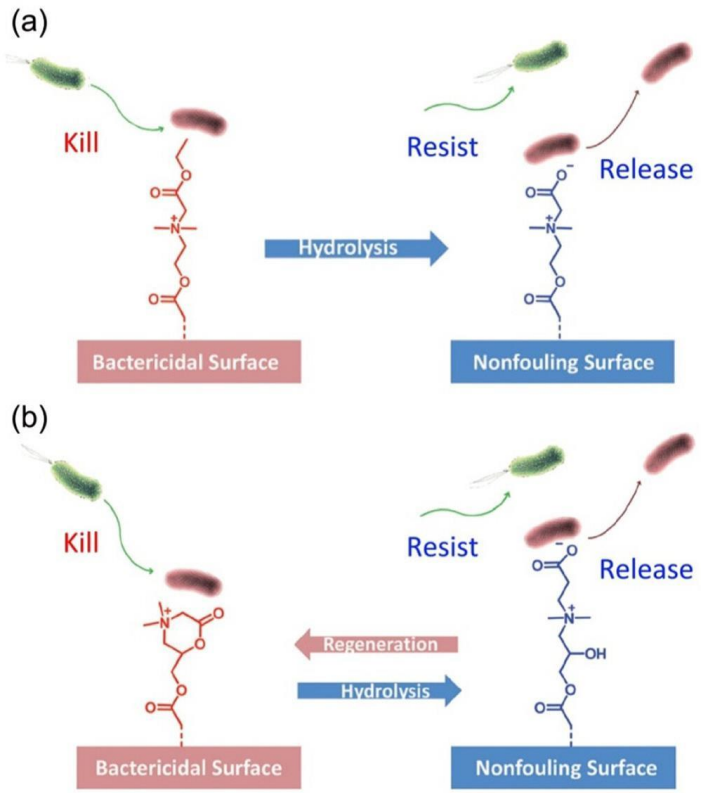

Figure 1.9. Zwitterionic surfaces that kill and release bacteria in response to the environmental pH value. (a) one-time effect, irreversible approach and (b) reversible approach after several times.[83]

1.4.2.2. Temperature responsive antibacterial surfaces with dual action

Among the temperature responsive polymers, poly(N-isopropylacrylamide) (PNIPAAm) is the most commonly used and best studied.[84] This polymer exhibits fouling-release properties since it can provide reversible wettability and bioadhesion properties in response to temperature changes below and above its lower critical solution temperature (LCST).[85–87] In previous studies, it has been proved that PNIPAAm can effectively release attached bacteria, as well as fully developed biofilms.[88,89] Therefore, there are a few studies that attempted to incorporate active

biocidal molecules into PNIPAAm polymeric matrixes in order to achieve dual "kill and release" antibacterial effect.

In recent studies, two common antibacterial compounds (quaternary ammonium salt and lysozyme) were incorporated in nanopatterned PNIPAAm polymeric brushes and their antibacterial properties were tested (**Figure 1.10**).[89,90] When the temperature was above PNIPAAm's LCST, the bacteria were attaching to the polymer surface and were dying because of the release of the incorporated antibacterial agent. When the temperature was below PNIPAAm's LCST, the swollen PNIPAAm chains were promoting the release of the dead bacteria. The main limitation with this system is that its biocidal activity and release properties can be maintained only for two cycles. Other limitation for this system is the several required steps to produce the dual action material.

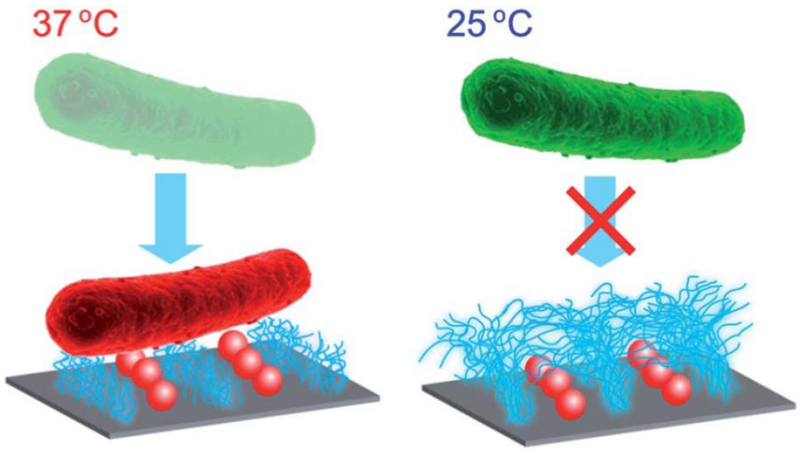

Figure 1.10. Schematic illustration of interactions between bacteria (E. coli) and nanopatterned PNIPAAm/Lys surface at different temperatures.[90]

1.5. Spherical mesoporous silica nanoparticles

In 1992, Mobil's scientists introduced for first time a detailed synthesis and characterization of a new family (M41S) of mesoporous molecular sieves using cationic quaternary ammonium surfactants as template [91,92]. The members of the M41S family named Mobil Crystalline of Materials (MCM) include MCM-41 (hexagonal pore system), MCM-48 (cubic pore system) and MCM-50 (laminar structure) (**Figure 1.11**). This discovery initiated a worldwide research of these materials, which continues until today.

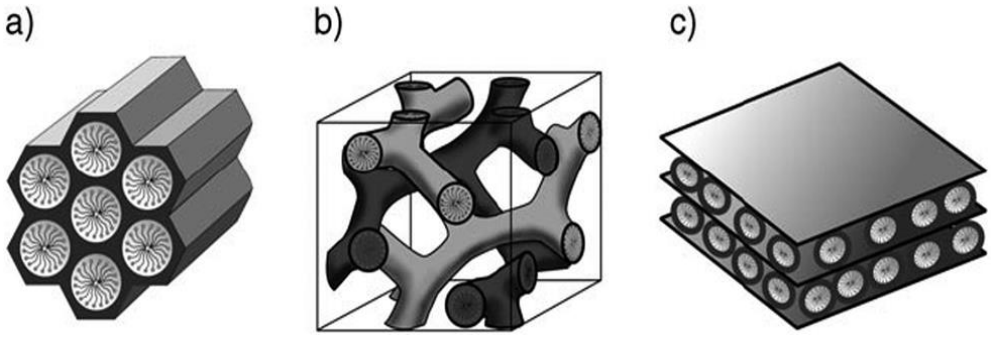

Figure 1.11. Pore structure systems for MCM-41 (hexagonal pore system), MCM-48 (cubic pore system) and MCM-50 (laminar structure).[93]

There are two earlier publications which often cited as the first attempts to synthesize ordered mesoporous materials but their importance characterised post-M41S as the authors didn't identify and characterise at that time the materials [94]. In the first case, a patent in 1971 reports a material obtained by reaction of tetraethylorthosilicate with cetyltrimethylammonium cationic surfactant but the characterisation of the material was limited and not clear. The experiment

reproduced in 1997 by Direnzo F. *et al*. with the advantage of the M41S knowledge and considered to be a mesoporous material [95]. The second case is in 1989 where Japanese scientists noticed the formation of alkyltrimethylammonium-kanemite complexes when single layered polysilicate kanemite was allowed to react with alkyltrimethylammoniumcloride at high pH [96]. However, they couldn't propose a mechanism which explains the formation of the whole family of mesoporous materials.

In order to explain the formation of the mesostructures, Mobil's scientists suggested the liquid-crystal template (LCT) mechanism [92]. They proposed two possible pathways (**Figure 1.12**), the first in which the liquid-crystal phase pre-exists before the silica source is added and the second in which during the addition of the silica source, the silicate anions promote the long-range ordering of the surfactant to form the hexagonal arrangement. In both pathways, under the conditions of the reaction the negatively charged silicate groups interact with the positively charged ammonium head groups of the surfactants and condense into a solid framework.

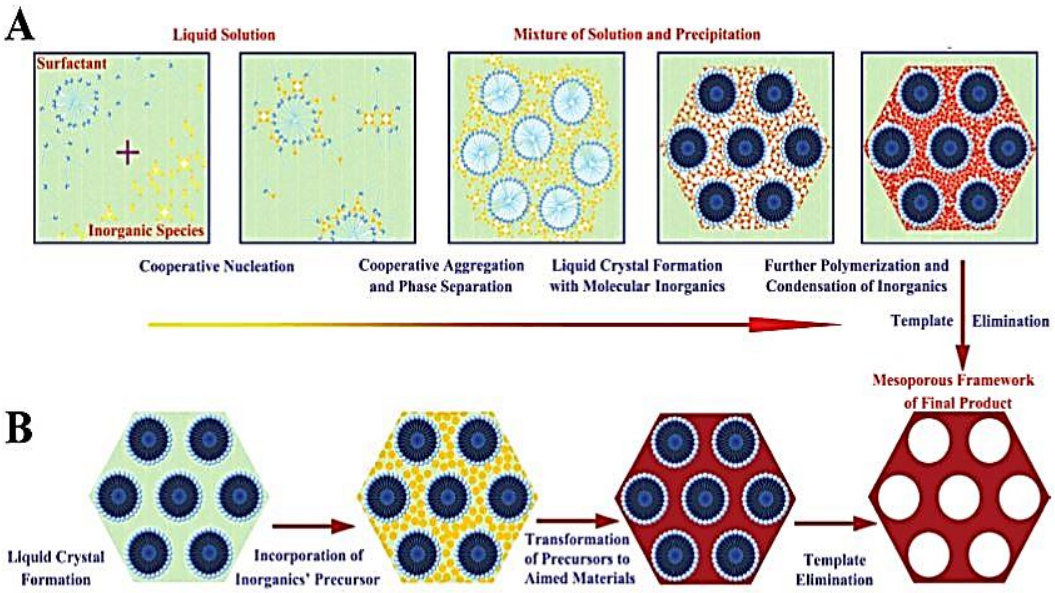

Figure 1.12. Two synthetic strategies of mesoporous materials: (A) cooperative self-assembly and (B) liquid-crystal templating process.[97]

Three different research groups have synthesised in parallel mesoporous silica nanostructures for first time in 2001 and 2002. Cai *et al*. synthesised MCM-41 spherical nanoparticles with average size of 110 nm through reaction of extremely low cationic surfactant concentration with tetraethylorthosilicate in sodium hydroxide medium at 353K [98]. Fowler *et al*. synthesised spherical MCM-41 in room temperature with average size of 20nm after decrease of the reaction rate by pH neutralization [99]. Nooney and co-workers synthesized spherical mesoporous silica nanoparticles (MSNs) with a simple one step procedure in which the average size of the nanoparticles was controlled in a range from 65 to 740 nm under dilute conditions [100]. The last ten years, a lot of groups all over the world made many attempts to synthesise MSNs with several dimensions, morphologies and pore sizes with controlling the reaction conditions such as the characteristics of the surfactants,

the pH of the reaction, the concentration and the source of the silica, etc. An ideal protocol for the fabrication of MSNs would be characterized by good stable suspension of the solution, and controllable particle and pore size [101].

A typical synthesis of MSNs follows the sol-gel process which is catalysed mostly by a base. During this process take place the following reactions [102]:

$$\equiv Si-OR + H_2O \underset{\text{esterification}}{\overset{\text{hydrolysis}}{\rightleftharpoons}} \equiv Si-OH + ROH \quad (1)$$

$$\equiv Si-OR + HO-Si\equiv \underset{\text{alcoholysis}}{\overset{\text{alcohol condensation}}{\rightleftharpoons}} \equiv Si-O-Si\equiv + ROH \quad (2)$$

$$\equiv Si-OH + HO-Si\equiv \underset{\text{hydrolysis}}{\overset{\text{water condensation}}{\rightleftharpoons}} \equiv Si-O-Si\equiv + H_2O \quad (3)$$

The most common silica sources for the formation of MSNs are the tetraalkoxysilanes $Si(OR)_4$ where R= Me, Et, Pr and Bu, the shorter chain alkoxysilane direct to smaller size nanoparticles because of the faster hydrolysis rates [103]. The catalyst of the reaction can be either base or acid. Typical bases for this reaction include sodium hydroxide, potassium hydroxide, ammonia, triethanolamine, tetramethylammonium hydroxide and tetraethylammonium hydroxide. In the case of acidic catalysis, hydrochloric acid, nitric acid and sulfuric acid are usually used. Typically, there are three types of surfactants that can be used: cationic, anionic and nonionic. The reaction temperature is varied from room temperature to 130^{o}C and it depends on the critical micelle concentration (CMC) of the surfactant. Cationic surfactants have relatively low CMC and therefore room

temperature is feasible. However, higher reaction temperature is required when nonionic surfactants are used due to their higher CMC values [97].

It is very important to know that the pH of the synthesis solution strongly influences the hydrolysis and condensation reactions due to the charges of the silica species. The isoelectric point (IEP) of silica is at pH=2, as can be seen from **Figure 1.13**, under the IEP, the silica species are positively charged and the charge density increases as the pH decreases. Above the IEP, at the pH range from 2 to 7, the silica species become negatively charged and are attracted by the positively charged cationic surfactants via electrostatic and hydrogen-bonding interactions. In basic conditions where the pH>7, the negatively charged species due to strong electrostatic interactions can only assemble with the cationic surfactants. As a consequence, in the silica condensation reaction, the more charged species there are in the reaction solution, the higher is the condensation rate of silica [104].

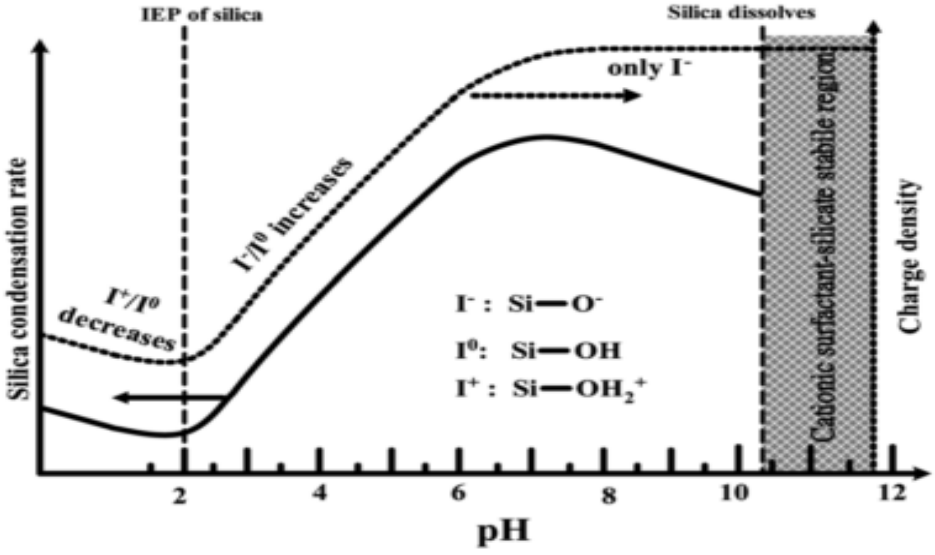

Figure 1.13. Effects of pH value on the silica condensation rate, charge properties and charge density on the surface of the silica species.[105]

One of the main problems during the synthesis of MSNs is their aggregation. During the condensation reactions, neighbouring silanol groups between different nanoparticles can bridge Si-O-Si bonds. In order to have a stable suspended colloidal solution, the aggregation should be reduced. There are two synthetic procedures to avoid or decrease the aggregation. Fowler *et al*. used a diluted system by addition of an excess of water to synthesise MCM-41 with average size of 20 nm. Due to the dilution, the bridge Si-O-Si bonds between the NPs decreased. The second approach succeeded when Suzuki *et al*. used a double surfactant system [106,107]. They used a cationic surfactant as a template and a nonionic surfactant as a suppressant of grain growth. The anionic silicates were assembled with the cationic surfactant and the nonionic surfactant reduced the aggregation through coating the surface of the silicates via hydrogen bonds.

In the literature, many authors refer that they used the modified Stober method to produce MSNs. Stober *et al*. first developed a system of chemical reactions to produce spherical silica particles [108]. They hydrolysed alkyl silicates in a solution of ethanol and water using ammonia as a morphological catalyst. Many years later, in 1997, Grun *et al*. first thought to modify Stober's method in order to synthesise MSNs [109]. They modified this method by adding a cationic surfactant to the reaction mixture as a source of micelles and they synthesised spherical MCM-41with average size of 600 nm. Since then, the modified Stober method used widely to produce MSNs with variations in the structure and the pore size. Yano K. and Fukushima Y. produced mono-dispersed spherical MSNs with a wide range of pore size by changing the ethanol ratio in the solution and using cationic surfactants with

different alkyl chain length [110]. Furthermore, they found that by adding a different silica precursor to the initial one, it is possible to form monodispersed spherical MSNs because the additional different silica precursor reacts preferentially with the silanol groups on the surface of the existing particles [111]. Chiang and co-workers investigated the influence of the amount of the silica source, the pH value and the reaction time to the size and structure of the particles [112]. It was found that the most important parameter is the pH value of the reaction solution. Kim *et al*. developed a rapid and facile synthesis route to spherical MCM-48 by controlling the stirring rate and adding a triblock copolymer (Pluronic F127) as a dispersing agent in order to control the particle size [113]. They found that spherical MCM-48 formed under vigorous stirring (1000 rpm) with size range of 70-500 nm depending on the amount of the Pluronic. Furthermore, they managed to control the pore size from 2.3 to 3.3 nm after using different alkyl chain length surfactants and hydrothermal treatment.

During the synthesis of MSNs, the reaction temperature is in the range from -10 to 130 ^{o}C depending on which surfactant is being used [97]. The cationic surfactants do not require high temperature of the reaction because their critical micelle temperature (CMT) is usually low and therefore in room temperature high quality MSNs can be obtained. On the other hand, nonionic surfactants have high CMT values which mean that the reaction temperature is higher than the room temperature. Furthermore, many of the cationic surfactants are insoluble in high temperature (cloud point value CP) and their solutions become cloudy because of the phase separation, as a result, they start to precipitate. Thus, in these cases the temperature of the reaction should be chosen with respect to the CMT and CP.

In general, after the synthesis of the MSNs, in order to receive highly ordered mesostructures, hydrothermal treatment is required in the range of temperature between 80 and 150 ºC. Stucky *et al*. found that the silicate framework condenses and undergoes reconstruction under hydrothermal conditions [114]. The mesostructures of the MSNs are formed during the synthesis but the regularity is enhanced via the hydrothermal treatment which can last from a few hours to several weeks. Petitto and co-workers produced for the first time a controlled direct synthesis of 3D mesostructured silicas via phase transition [115]. When MCM-41 are formed in high alkaline conditions, they have low degree of polymerization which allows the further MCM-41/-48 phase transition via hydrothermal treatment. Xia *et al*. noticed that hexagonal-cubic-lamellar phase transformations take place at 135 ºC by varying the treatment time to 3 hours, 24 hours and 12 days respectively [116]. Until 1999, all published methods for the synthesis of MCM-48 were via hydrothermal treatment. Schumacher *et al*. synthesised for the first time highly ordered MCM-48 at room temperature without the need of hydrothermal treatment [117]. This method is the fastest one to produce MCM-48, it needs only 2 hours.

The last step of the MSNs synthesis is the removal of the template. There are two ways to remove the surfactant, with calcination or with extraction. Calcination is the most common method due to its simplicity and because it completely removes the surfactant. Usually, it takes place at 550 ºC with heating rate 1ºC/minute and keeping this temperature stable for 6 hours. The template can be completely removed by calcination only in air or oxygen conditions. The favourable characteristics of the MSNs such as high specific area, large pore volume, etc are decreased if the calcination temperature is higher than 550 ºC. The drawbacks of this method are the

decrease of the silanol groups on the surface of the materials and the unrecovered surfactants. The extraction of the template takes place using ethanol or THF and a small amount of HCl. The surfactants in general have excellent solubility in ethanol. Since the extraction is a mild method for the removal of the surfactants, MSNs with better characteristics than those obtained using the calcination method can be prepared. In addition, the amount of hydroxyl groups on the surface of the MSNs is much higher than the amount after calcination and the surfactants can be reused. The drawback of this method is that the surfactants are not completely removed [97].

1.6. Quaternary ammonium salts as functional surface groups

Quaternary ammonium salts (QASs) have been indexed as antimicrobial compounds for more than 50 years. They have been used against the bacterial growth of a broad range of microorganisms in several applications including food and pharmaceutical products, antiseptics, disinfectants, biocides, fungicides, cosmetics and water treatment [118,119]. The QAS are positively charged cationic compounds and the bacterial cell membranes are negatively charged. As a consequence of electrostatic interactions, the QAS can be adsorbed on the cell surfaces and diffuse through the cell wall. The next step is their binding to the cytoplasmic membrane causing its disruption and release of K^+ ions and constituents of the cytoplasmic membrane which leads to cell death[120,121].

The effectiveness of the QAS in killing a wide range of microorganisms attracted the interest of scientists as antimicrobial agents. In several studies, QAS were used to functionalise surfaces of different materials as antimicrobial treatment. The big advantage of these QAS functionalised materials is their interaction nature with the host material. In comparison with the biocide release based coatings, the QAS are covalently attached to the coatings and they have permanent biocidal activity. Gottenbos *et al*. studied the antimicrobial activity of QAS-coating on silicone rubber against Gram-negative and Gram-positive bacteria and they found that QAS were effective both in vivo and in vitro [122]. Nurdin *et al*. prepared polyurethane-QAS films which exhibited high biocidal activity against Gram-negative and Gram-positive bacteria, yeasts and moulds [123]. Furthermore, the polysiloxane matrixes have been widely used as carriers for the QAS because they have been shown to exhibit good fouling release character and biocompatibility [124–126]. Other modified materials with QAS for antimicrobial activity including poly (propylene imine), glass surfaces, chitosan, activated carbon and silica nanoparticles [127–131].

There are several parameters which influence the interactions between the quaternary ammonium moieties and the cell membranes and therefore their biocidal activity. The effectiveness of a specific QAS is microorganism dependent since there are variations to the composition and structure from one microorganism to another [132]. Kugler *et al*. found that there is a charge-density threshold for optimum efficiency of surfaces bonded with QAS. At their experiments, they found that the threshold is dependant from the bacterial type and it should be high enough in order to cause death of the bacteria [133]. Chen and co-workers found that biocides which consist of 16 quaternary ammonium groups on their surfaces present over 2 orders of

magnitude better antimicrobial activity than monofunctional counterparts [134]. Oblak *et al*. reported that the biocidal performance of gemini QAS (two hydrophilic cationic head groups and two hydrophobic moieties per molecule) is better than the monomeric QAS performance [135]. Another important parameter for the efficiency of the QAS is the alkyl chain length of their general molecular formula (NR_4^+). Nakawaga *et al*. studied the antibacterial activity of QAS with variation of alkyl chain length from C_2 to C_{18} to conclude that QAS with alkyl chain length from C_8 and higher present high antimicrobial activity [136]. Tiller *et al*. found that immobilized poly(4-vinyl-N-alkylpyridinium bromide) with C_2, C_4, C_6 and C_8 chain length effectively reduced the number of viable bacteria cells while C_{10}-C_{16} were totally ineffective [137].

From the big family of the QAS, dimethyloctadecyl[3-(trimethoxysilyl)propyl] ammonium chloride (DMOAP, **Figure 1.14**) has been widely used due to its hydrophobic character and excellent antimicrobial activity [122,127,59,138,139]. Li *et al*. incorporated DMOAP in a coating formula in combination with other antifouling agents and reported the high bacteria-killing efficiency of the coating [59]. Majumdar and co-workers synthesised polysiloxane coatings containing tethered DMOAP and found its effectiveness against two marine bacteria and one marine microalgae diatom [125].

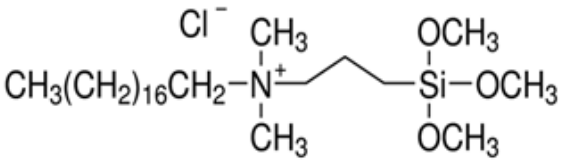

Figure 1.14. Dimethyloctadecyl[3-(trimethoxysilyl)propyl] ammonium chloride.

Among the large number of publications about QAS functionalised material, there are only a few where silica nanoparticles were used for surface modification with QAS. Silica NPs can be easily functionalised with QAS which have siloxyl groups. Zhu *et al*. synthesised poly(dimethyl aninoethyl methacrylate) grafted silica nanoparticles via RAFT polymerization. After the polymerization, they used a simple reaction of quartenization to transform the tertiary amino groups into quaternary ammonium groups. Afterwards, they incorporated the modified NPs into polyethersulfone membranes in order to achieve antimicrobial properties [140]. Song *et al*. studied the bacteria adhesion inhibition of modified silica NPs with QAS. The modified materials exhibited excellent antibacterial activity [131].

1.7. Current research

After the ban of the efficient but environmentally harmful antifouling paints based on tributyltin, the creation of new, effective and low-toxic antifouling paints is a major challenge. The aim of the work presented in this thesis was to develop novel modified nanoparticles as functional fillers for low toxic and environmentally friendly antibacterial/antifouling coatings for mobile and stationary applications in

maritime, hospitals, industries, etc. Therefore, our research is based on the dual functionalisation of nanocontainers in order to be used as functional fillers for antibacterial/antifouling applications with enhanced performance compared to the current available products in the market. Simple methods were sought, which may be scaled up in the future for commercial purposes. Initially, we focused on finding appropriate carries as core materials for dual functionalities. Thus, we attempted to use mesoporous silica nanoparticles, which provide favourable characteristics for dual modification. This type of materials can be easily surface modified with several compounds because of the existence of hydroxyl groups on their surface. Subsequently, a second functionality can be achieved using encapsulation techniques by loading their mesoporous pore channel system with active compounds. Once the appropriate carriers had been found, suitable and established biocides and antibacterial/antifouling compounds were selected in order to provide dual antibacterial/antifouling effect to the modified materials.

At the second part of the work presented in this thesis, the physical and chemical properties of the synthesised dual functional nanocontainers were further assessed and their successful dual functionalisation was confirmed. Afterwards, the excellent antibacterial properties of the synthesised materials in powder form were confirmed in lab scale experiments. Following the promising results from the antibacterial tests, the dual modified nanocontainers were incorporated in coatings formulations for the final application. The nanocontainer-doped coatings were tested according to their physical and surface properties, and more importantly according to their antibacterial/antifouling efficiency both on lab scale and field test experiments. The nanocontainer-doped paints showed: a) homogeneous distribution of the

nanocontainer in the coating formulations, b) increased hydrophobic surfaces, c) excellent antibacterial performance by killing all the bacteria at the end of the experiments, d) excellent anti-macrofouling properties to the paints and, at the same time, low toxicity against non-target species and e) excellent antifouling performance at a six-month field test in Red Sea, Israel.

Through our research, we demonstrated a simple and facile approach to synthesise dual functionalised nanocontainers that can be effectively incorporated in coating formulations providing enhanced antibacterial/antifouling properties combined with low toxicity against non-target species. Results detailed in this thesis may also be of use to researchers studying: i) other combinations of biocides-antibacterial-antifouling compounds to achieve dual effect and ii) similar or other potential nanocontainers as carriers of dual-functionalities for a broad spectrum of applications.

References

[1] J. A. Callow, M. E. Callow, *Nat. Commun.* **2011**, *2*, 244.

[2] M. E. Callow, J. A. Callow, *Biologist* **2002**, *49*, 10.

[3] M. Lejars, A. Margaillan, C. Bressy, *Chem. Rev.* **2012**, *112*, 4347.

[4] A. G. Nurioglu, A. C. C. Esteves, G. de With, *J. Mater. Chem. B* **2015**, *3*, 6547.

[5] L. D. Chambers, K. R. Stokes, F. C. Walsh, R. J. K. Wood, *Surf. Coatings Technol.* **2006**, *201*, 3642.

[6] C. M. Magin, S. P. Cooper, A. B. Brennan, *Mater. Today* **2010**, *13*, 36.

[7] M. Lejars, A. Margaillan, C. Bressy, *Chem. Rev.* **2012**, *112*, 4347.

[8] S. Kiil, K. Dam-Johansen, C. E. Weinell, M. S. Pedersen, S. A. Codolar, *J. Coatings Technol.* **2002**, *74*, 45.

[9] J. P. Maréchal, C. Hellio, *Int. J. Mol. Sci.* **2009**, *10*, 4623.

[10] M. P. Schultz, J. A. Bendick, E. R. Holm, W. M. Hertel, *Biofouling* **2011**, *27*, 87.

[11] I. Fitridge, T. Dempster, J. Guenther, R. de Nys, *Biofouling* **2012**, *28*, 649.

[12] I. B. Beech, *Int. Biodeterior. Biodegrad.* **2004**, *53*, 177.

[13] M. S. Selim, M. A. Shenashen, S. A. El-Safty, S. A. Higazy, M. M. Selim, H. Isago, A. Elmarakbi, *Prog. Mater. Sci.* **2017**, *87*, 1.

[14] ICS, *Shipping, World Trade and the Reduction of C02 Emissions*, **2013**.

[15] D. M. Yebra, S. Kiil, K. Dam-Johansen, *Prog. Org. Coatings* **2004**, *50*, 75.

[16] G. A. Hopkins, B. M. Forrest, *ICES J. Mar. Sci.* **2008**, *65*, 811.

[17] I. Fitridge, T. Dempster, J. Guenther, R. de Nys, *Biofouling* **2012**, *28*, 649.

[18] J. V. Aarsnes, H. Rudi, G. Loland, The Institution Of Civil Engineers, Engineering For Offshore Fish Farming., **1990**, pp. 137–152.

[19] R. J. Andersen, H. A. Luu, D. Z. X. Chen, C. F. B. Holmes, M. L. Kent, M. Le Blanc, F. J. R. 'Max. Taylor, D. E. Williams, *Toxicon* **1993**, *31*, 1315.

[20] D. Johansson, K. Ruohonen, A. Kiessling, F. Oppedal, J.-E. Stiansen, M. Kelly, J.-E. Juell, *Aquaculture* **2006**, *254*, 594.

[21] P. Lader, T. Dempster, A. Fredheim, Ø. Jensen, *Aquac. Eng.* **2008**, *38*, 52.

[22] C. M. Adams, S. E. Shumway, R. B. Whitlatch, T. Getchis, *J. World Aquac. Soc.* **2011**, *42*, 242.

[23] L. Delauney, C. Compère, M. Lehaitre, *Ocean Sci.* **2010**, *6*, 503.

[24] O. Langhamer, D. Wilhelmsson, J. Engström, *Estuar. Coast. Shelf Sci.* **2009**, *82*, 426.

[25] M. Babin, C. S. Roesler, J. J. Cullen, *Real-Time Coastal Observing Systems for Marine Ecosystem Dynamics and Harmful Algal Blooms : Theory, Instrumentation and Modelling*, UNESCO, Paris, France, **2008**.

[26] *MARINE FOULING AND ITS PREVENTION*, Woods Hole Oceanographic

Institution, US Naval Institute, Annapolis, Maryland, **1952**.

[27] M. Callow, *Chelistry Ind.* **1990**, *5*.

[28] E. Almeida, T. C. Diamantino, O. de Sousa, *Prog. Org. Coatings* **2007**, *59*, 2.

[29] IMO, *Int. Marit. Organ.* **2002**, *44*, 1.

[30] I. Omae, *Chem. Rev.* **2003**, *103*, 3431.

[31] F. Marson, *J. Appl. Chem.* **2007**, *19*, 93.

[32] V. J. D. Rascio, C. A. Giúdice, B. del Amo, *Corros. Rev.* **1988**, *8*, DOI 10.1515/CORRREV.1988.8.1-2.87.

[33] I. Omae, *Appl. Organomet. Chem.* **2003**, *17*, 81.

[34] S. Sonak, P. Pangam, A. Giriyan, K. Hawaldar, *J. Environ. Manage.* **2009**, *90*, S96.

[35] N. Voulvoulis, M. D. Scrimshaw, J. N. Lester, *Appl. Organomet. Chem.* **1999**, *13*, 135.

[36] S. . Evans, A. . Birchenough, M. . Brancato, *Mar. Pollut. Bull.* **2000**, *40*, 204.

[37] K. V. Thomas, *Advances in Marine Antifouling Coatings and Technologies*, Woodshead Publishing, Cambridge, UK, **2009**.

[38] K. V. Thomas, S. Brooks, *Biofouling* **2010**, *26*, 73.

[39] I. K. Konstantinou, T. A. Albanis, *Environ. Int.* **2004**, *30*, 235.

[40] C. Hellio, M. Tsoukatou, J.-P. Maréchal, N. Aldred, C. Beaupoil, A. S. Clare,

C. Vagias, V. Roussis, *Mar. Biotechnol.* **2005**, *7*, 297.

[41] P.-Y. Qian, Y. Xu, N. Fusetani, *Biofouling* **2009**, *26*, 223.

[42] R. F. Brady, *Prog. Org. Coatings* **1999**, *35*, 31.

[43] R. F. Brady, *Prog. Org. Coatings* **2001**, *43*, 188.

[44] R. F. Gould, Ed. , **1964**.

[45] E. Robbart, *Ship Hull Coated with Anti-Fouling Silicone Resin and Method of Coating*, **1961**, US2986474.

[46] B. R. Knowles, P. Wagner, S. Maclaughlin, M. J. Higgins, P. J. Molino, *ACS Appl. Mater. Interfaces* **2017**, *9*, 18584.

[47] M. Andersson Trojer, L. Nordstierna, J. Bergek, H. Blanck, K. Holmberg, M. Nydén, *Adv. Colloid Interface Sci.* **2015**, *222*, 18.

[48] D. Borisova, H. Möhwald, D. G. Shchukin, *ACS Nano* **2011**, *5*, 1939.

[49] M. Graham, J. A. Coca-Clemente, E. Shchukina, D. Shchukin, *J. Mater. Chem. A* **2017**, *5*, 13683.

[50] H. Gao, O. A. Goriacheva, N. V. Tarakina, G. B. Sukhorukov, *ACS Appl. Mater. Interfaces* **2016**, *8*, 9651.

[51] Z. Zheng, Z. Chang, G.-K. Xu, F. McBride, A. Ho, Z. Zhuola, M. Michailidis, W. Li, R. Raval, R. Akhtar, D. Shchukin, *ACS Nano* **2017**, *11*, 721.

[52] H. Gao, D. Wen, G. B. Sukhorukov, *J. Mater. Chem. B* **2015**, *3*, 1888.

[53] D. V. Andreeva, D. Fix, H. Möhwald, D. G. Shchukin, *J. Mater. Chem.* **2008**, *18*, 1738.

[54] G. Sørensen, A. L. Nielsen, M. M. Pedersen, S. Poulsen, H. Nissen, M. Poulsen, S. D. Nygaard, *Prog. Org. Coatings* **2010**, *68*, 299.

[55] M. Yang, L. Gu, B. Yang, L. Wang, Z. Sun, J. Zheng, J. Zhang, J. Hou, C. Lin, *Appl. Surf. Sci. jou* **2017**, *426*, 185.

[56] F. Maia, A. P. Silva, S. Fernandes, A. Cunha, A. Almeida, J. Tedim, M. L. Zheludkevich, M. G. S. Ferreira, *Chem. Eng. J.* **2015**, *270*, 150.

[57] S. V. Lamaka, D. G. Shchukin, D. V. Andreeva, M. L. Zheludkevich, H. Möhwald, M. G. S. Ferreira, *Adv. Funct. Mater.* **2008**, *18*, 3137.

[58] Q. Yu, Z. Wu, H. Chen, *Acta Biomater.* **2015**, *16*, 1.

[59] Z. Li, D. Lee, X. Sheng, R. E. Cohen, M. F. Rubner, *Langmuir* **2006**, *22*, 9820.

[60] H. Chen, L. Yuan, W. Song, Z. Wu, D. Li, *Prog. Polym. Sci.* **2008**, *33*, 1059.

[61] J. M. Goddard, J. H. Hotchkiss, *Prog. Polym. Sci.* **2007**, *32*, 698.

[62] Q. Yu, Y. Zhang, H. Wang, J. Brash, H. Chen, *Acta Biomater.* **2011**, *7*, 1550.

[63] N. Aumsuwan, S. Heinhorst, M. W. Urban, *Biomacromolecules* **2007**, *8*, 713.

[64] N. Aumsuwan, M. S. McConnell, M. W. Urban, *Biomacromolecules* **2009**, *10*, 623.

[65] S. Yuan, D. Wan, B. Liang, S. O. Pehkonen, Y. P. Ting, K. G. Neoh, E. T.

Kang, *Langmuir* **2011**, *27*, 2761.

[66] W. J. Yang, T. Cai, K.-G. Neoh, E.-T. Kang, G. H. Dickinson, S. L.-M. Teo, D. Rittschof, *Langmuir* **2011**, *27*, 7065.

[67] C. H. Ho, J. Tobis, C. Sprich, R. Thomann, J. C. Tiller, *Adv. Mater.* **2004**, *16*, 957.

[68] E. M. Shchukina, D. G. Shchukin, *Curr. Opin. Colloid Interface Sci.* **2012**, *17*, 281.

[69] E. M. Shchukina, D. G. Shchukin, *Adv. Drug Deliv. Rev.* **2011**, *63*, 837.

[70] A. A. Antipov, G. B. Sukhorukov, *Adv. Colloid Interface Sci.* **2004**, *111*, 49.

[71] D. G. Shchukin, G. B. Sukhorukov, *Adv. Mater.* **2004**, *16*, 671.

[72] S. Y. Wong, L. Han, K. Timachova, J. Veselinovic, M. N. Hyder, C. Ortiz, A. M. Klibanov, P. T. Hammond, *Biomacromolecules* **2012**, *13*, 719.

[73] I. Zhuk, F. Jariwala, A. B. Attygalle, Y. Wu, M. R. Libera, S. A. Sukhishvili, *ACS Nano* **2014**, *8*, 7733.

[74] S. Y. Wong, Q. Li, J. Veselinovic, B.-S. Kim, A. M. Klibanov, P. T. Hammond, *Biomaterials* **2010**, *31*, 4079.

[75] H. D. M. Follmann, A. F. Martins, A. P. Gerola, T. A. L. Burgo, C. V. Nakamura, A. F. Rubira, E. C. Muniz, *Biomacromolecules* **2012**, *13*, 3711.

[76] W. J. Yang, D. Pranantyo, K. G. Neoh, E. T. Kang, S. L. M. Teo, D. Rittschof, *Biomacromolecules* **2012**, *13*, 2769.

[77] G. Cheng, H. Xue, G. Li, S. Jiang, *Langmuir* **2010**, *26*, 10425.

[78] L. Mi, S. Jiang, *Biomaterials* **2012**, *33*, 8928.

[79] L. Mi, H. Xue, Y. Li, S. Jiang, *Adv. Funct. Mater.* **2011**, *21*, 4028.

[80] F. Ji, W. Lin, Z. Wang, L. Wang, J. Zhang, G. Ma, S. Chen, *ACS Appl. Mater. Interfaces* **2013**, *5*, 10489.

[81] G. Cheng, H. Xue, Z. Zhang, S. Chen, S. Jiang, *Angew. Chemie Int. Ed.* **2008**, *47*, 8831.

[82] Z. Cao, L. Mi, J. Mendiola, J.-R. Ella-Menye, L. Zhang, H. Xue, S. Jiang, *Angew. Chemie Int. Ed.* **2012**, *51*, 2602.

[83] L. Mi, S. Jiang, *Angew. Chemie Int. Ed.* **2014**, *53*, 1746.

[84] H. G. Schild, *Prog. Polym. Sci.* **1992**, *17*, 163.

[85] L. K. Ista, S. Mendez, S. S. Balamurugan, S. Balamurugan, V. G. Rama Rao, G. P. Lopez, **2009**, pp. 95–110.

[86] R. J. A., L. S. A., L. A. E., H. C. L., C. H. E., *Langmuir* **2012**, *28*, 2281.

[87] Q. Yu, Y. Zhang, H. Chen, Z. Wu, H. Huang, C. Cheng, *Colloids Surfaces B Biointerfaces* **2010**, *76*, 468.

[88] L. K. Ista, G. P. Lopez, *J. Ind. Microbiol. Biotechnol.* **1998**, *20*, 121.

[89] Q. Yu, J. Cho, P. Shivapooja, L. K. Ista, G. P. López, *ACS Appl. Mater. Interfaces* **2013**, *5*, 9295.

[90] Q. Yu, L. K. Ista, G. P. López, *Nanoscale* **2014**, *6*, 4750.

[91] C. T. Kresge, M. E. Leonowicz, W. J. Roth, J. C. Vartuli, J. S. Beck, *Nature* **1992**, *359*, 710.

[92] J. S. Beck, J. C. Vartuli, W. J. Roth, M. E. Leonowicz, C. T. Kresge, K. D. Schmitt, C. T. W. Chu, D. H. Olson, E. W. Sheppard, S. B. McCullen, J. B. Higgins, J. L. Schlenker, *J. Am. Chem. Soc.* **1992**, *114*, 10834.

[93] F. Hoffmann, M. Cornelius, J. Morell, M. Fröba, *Angew. Chemie - Int. Ed.* **2006**, *45*, 3216.

[94] C. T. Kresge, W. J. Roth, *Chem. Soc. Rev.* **2013**, *42*, 3663.

[95] F. Di Renzo, H. Cambon, R. Dutartre, *Microporous Mater.* **1997**, *10*, 283.

[96] T. Yanagisawa, T. Shimizu, K. Kuroda, C. Kato, *Bull. Chem. Soc. Jpn.* **1990**, *63*, 988.

[97] Y. Wan, D. Zhao, *Chem. Rev.* **2007**, *107*, 2821.

[98] Q. Cai, Z. S. Luo, W. Q. Pang, Y. W. Fan, X. H. Chen, F. Z. Cui, *Chem. Mater.* **2001**, *13*, 258.

[99] C. E. Fowler, D. Khushalani, B. Lebeau, S. Mann, *Adv. Mater.* **2001**, *13*, 649.

[100] R. I. Nooney, D. Thirunavukkarasu, Y. Chen, R. Josephs, A. E. Ostafin, *Chem. Mater.* **2002**, 4721.

[101] C.-Y. M. and H.-P. L. Si-Han Wu, *Chem. Soc. Rev.* **2013**, 3862.

[102] Z. Li, J. C. Barnes, A. Bosoy, J. F. Stoddart, J. I. Zink, *Chem. Soc. Rev.* **2012**,

41, 2590.

[103] H. Yamada, C. Urata, Y. Aoyama, S. Osada, Y. Yamauchi, K. Kuroda, *Chem. Mater.* **2012**, *24*, 1462.

[104] H. Lin, C. Mou, *Acc Chem. Res.* **2002**, *35*, 927.

[105] R. K. Iler, *Wiley* **1979**, *New York*, 897.

[106] K. Suzuki, K. Ikari, H. Imai, *J. Am. Chem. Soc.* **2004**, *126*, 462.

[107] K. Ikari, K. Suzuki, H. Imai, *Langmuir* **2006**, *22*, 802.

[108] W. Stöber, A. Fink, E. Bohn, *J. Colloid Interface Sci.* **1968**, *26*, 62.

[109] M. Gr n, I. Lauer, K. K. Unger, *Angew. Chemie Int. Ed.* **1997**, *9*, 254.

[110] K. Yano, Y. Fukushima, *J. Mater. Chem.* **2004**, *14*, 1579.

[111] and K. Y. Tadashi Nakamura, Mamoru Mizutani, Hiroshi Nozaki, Noritomo Suzuki, *J. Phys. Chem. C* **2007**, *111*, 1093.

[112] Y.-D. Chiang, H.-Y. Lian, S.-Y. Leo, S.-G. Wang, Y. Yamauchi, K. C. W. Wu, *J. Phys. Chem. C* **2011**, *115*, 13158.

[113] T.-W. Kim, P.-W. Chung, V. S.-Y. Lin, *Chem. Mater.* **2010**, *22*, 5093.

[114] Q. Huo, D. I. Margolese, G. D. Stucky, *Chem. Mater.* **1996**, *4756*, 1147.

[115] C. Petitto, A. Galarneau, M. F. Driole, B. Chiche, B. Alonso, F. D. Renzo, F. Fajula, *Chem. Mater.* **2005**, *17*, 2120.

[116] Y. Xia, R. Mokaya, J. J. Titman, *J. Phys. Chem. B* **2004**, *108*, 11361.

[117] K. Schumacher, M. Grün, K. . Unger, *Microporous Mesoporous Mater.* **1999**, *27*, 201.

[118] K. Hegstad, S. Langsrud, B. T. Lunestad, A. A. Scheie, M. Sunde, S. P. Yazdankhah, *Microb. Drug Resist.* **2010**, *16*, 91.

[119] J. Y. Maillard, *Symp. Ser. Soc. Appl. Microbiol.* **2002**, 16S.

[120] T. Tashiro, *Macromol. Mater. Eng.* **2001**, *286*, 63.

[121] A. Davies, M. Bentley, B. S. Field, *J. Appl. Bacteriol.* **1968**, *31*, 448.

[122] B. Gottenbos, H. C. Van Der Mei, F. Klatter, P. Nieuwenhuis, H. J. Busscher, *Biomaterials* **2002**, *23*, 1417.

[123] N. Nurdin, G. Helary, G. Sauvet, *J. Appl. Polym. Sci.* **1993**, *50*, 663.

[124] S. Ye, P. Majumdar, B. Chisholm, S. Stafslien, Z. Chen, *Langmuir* **2010**, *26*, 16455.

[125] P. Majumdar, E. Lee, N. Patel, K. Ward, S. J. Stafslien, J. Daniels, B. J. Chisholm, P. Boudjouk, M. E. Callow, J. A. Callow, S. E. M. Thompson, *Biofouling* **2008**, *24*, 185.

[126] G. Sauvet, S. Dupond, K. Kazmierski, J. Chojnowski, *J. Appl. Polym. Sci.* **2000**, *75*, 1005.

[127] Z. Shi, K. G. Neoh, E. T. Kang, *Ind. Eng. Chem. Res.* **2007**, *46*, 439.

[128] M. J. Saif, J. Anwar, M. A. Munawar, *Langmuir* **2009**, *25*, 377.

[129] C. Zhisheng Chen, S. L. Cooper, N. C. Beck Tan, *Chem. Commun.* **1999**,

1585.

[130] Chun Ho Kim and Kyu Suk Choi, *J. Ind. Eng. Chem.* **2002**, *8*, 71.

[131] J. Song, H. Kong, J. Jang, *Colloids Surfaces B Biointerfaces* **2011**, *82*, 651.

[132] P. Majumdar, J. He, E. Lee, A. Kallam, N. Gubbins, S. J. Stafslien, J. Daniels, B. J. Chisholm, *J. Coatings Technol. Res.* **2010**, *7*, 455.

[133] R. Kügler, O. Bouloussa, F. Rondelez, *Microbiology* **2005**, *151*, 1341.

[134] C. Z. Chen, N. C. Beck-Tan, P. Dhurjati, T. K. van Dyk, R. A. LaRossa, S. L. Cooper, *Biomacromolecules* **2000**, *1*, 473.

[135] E. Obłąk, A. Piecuch, K. Guz-Regner, E. Dworniczek, *FEMS Microbiol. Lett.* **2014**, *350*, 190.

[136] N. Yoshihiro, H. Hiroyuki, T. Takahiko, K. Hiroki, H. Tokunaru, S. Isao, *Appl. Environ. Microbiol.* **1984**, *47*, 513.

[137] J. C. Tiller, C. J. Liao, K. Lewis, a M. Klibanov, *Proc. Natl. Acad. Sci. U. S. A.* **2001**, *98*, 5981.

[138] P. Majumdar, E. Lee, N. Patel, K. Ward, S. J. Stafslien, J. Daniels, B. J. Chisholm, P. Boudjouk, M. E. Callow, J. a Callow, S. E. M. Thompson, *Biofouling* **2008**, *24*, 185.

[139] P. Majumdar, E. Lee, N. Gubbins, D. A. Christianson, S. J. Stafslien, J. Daniels, L. Vanderwal, J. Bahr, B. J. Chisholm, *J. Comb. Chem.* **2009**, *11*, 1115.

[140] L.-J. Zhu, L.-P. Zhu, Y.-F. Zhao, B.-K. Zhu, Y.-Y. Xu, *J. Mater. Chem. A* **2014**, *2*, 15566.

Chapter 2: Materials and Characterisation Techniques

2.1. Introduction

In this chapter, we describe the materials and characterisation techniques used in this thesis. The chapter is divided in three main sections. In section 2.2., we describe the materials used for the synthetic experimental procedures. Next, section 2.3. describes the methods used in order to characterise the two different types of mesoporous silica nanoparticles (MSNs) and the methods used to characterise and confirm the successful surface modification and encapsulation of the biocide in the mesoporous materials. Finally, section 2.4 describes the techniques used in order to characterise the nanocontainer-doped coating formulations (distribution of the nanocontainers in the coatings and surface properties of the coatings).

2.2. Materials

For the synthesis of the MSNs, tetraethyl orthosilicate (TEOS 98%, Sigma-Aldrich) was used as the source of silica. Hexadecyltrimethylammonium bromide (CTAB 99%, Sigma-Aldrich) and Pluronic F127 (colorless powder, Sigma-Aldrich) were used as surfactants (structure directing agents). Ethanol (99.8%, Sigma-Aldrich) and ammonium hydroxide (32 wt % solution, Merck) were used to carry out the synthesis of MSNs.

For the surface modification of MSNs two types of quaternary ammonium salts (QASs) were used. Dimethyloctadecyl [3-(trimethoxysilyl) propyl] ammonium chloride (QC18 60% in methanol, Acros Organics) and dimethyltetradecyl [3-(triethoxysilyl) propyl] ammonium chloride (QC14). The QC14 was synthesised by

reacting N,N-dimethyltetradecylamine (95%, Sigma-Aldrich) with 3-chloropropyltriethoxy silane (95%, Sigma-Aldrich). The biocide for the loading of the MSNs was Parmetol S15 (Schulke).

For the antibacterial tests, we used Gram-positive *S. aureus* (ATCC 25923) and Gram-negative *E. coli* (ATCC 10536) bacteria. The growth medium used for the overnight cultures of the bacteria was: powder microbial growth medium Luria Broth (Miller's LB, Sigma-Aldrich). For the preparation of the agar petri-dishes we used powder microbial growth medium Luria Broth with agar (Miller's LB agar, Sigma-Aldrich). The buffer solution phosphate-buffered saline (PBS) used for the recovery of the bacteria from the treated glass slides was prepared by mixing sodium chloride (99.5%, Sigma-Aldrich) and sodium phosphate dibasic heptahydrate (99%, Sigma-Aldrich).

2.3. Characterisation techniques: pristine and modified MSNs in powder form.

2.3.1. X-ray diffraction

X-ray powder diffraction (XRD) is a rapid analytical technique widely used for the phase identification and structure characterisation of crystalline materials. The powder XRD patterns for the synthesised MCM-48 nanoparticles were collected on a laboratory diffractometer (Bruker, D8 Venture) using Cu Ka radiation. The powder samples were finely grinded using a pestle and mortar. The fine powder samples

were packed in borosilicate glass capillary tubes (0.5 mm diameter, Capillary Tube Supplies Ltd) and their diffraction data were recorded in 2θ range of 1.5 to 10° for 60 minutes.

2.3.2. Nitrogen adsorption isotherms

The low-temperature nitrogen isotherms can provide accurate and reliable information associated with the specific surface area and the quality of the mesoporous structure of solid materials. Nitrogen adsorption isotherms were measured at 77 K on a Quadrasorb SI analyser (Quantachrome Instruments) in Max Planck Institute for Colloids and Interfaces, Germany. Before the measurements, the samples were finely ground with a pestle and mortar and outgassed under vacuum for 20 hours at 423 K in the degas port of the adsorption apparatus. Data of relative pressure P/P_0 between 0.01 and 0.16 were used for the calculation of the BET specific area according to the Brunauer - Emmett - Teller (BET) method.[1] The pore size distribution and the total pore volume of the synthesised MCM-48 materials were calculated from the nitrogen adsorption isotherms by using the nonlocal density functional theory (NLDFT) method.[2–4]

2.3.3. Scanning electron microscopy

A scanning electron microscope (SEM) scans the surface of the sample with a focused beam of electrons and generates a variety of signals due to the interactions between the electrons of the beam and the atoms of the sample. These signals can be secondary electrons, backscattered electrons, X-rays and visible photons that contain

information about the sample's topography and composition. The signals are recorded by appropriate detectors in order to produce images with high magnification and resolution better than 1 nm can be achieved.[5]

In order to analyse the morphology of the MCM-48 samples, SEM measurements were taken with a JEOL JSM-7001F scanning electron microscope in the nanoinvestigation centre at Liverpool (**Figure 2.1**). For the preparation of the samples, MCM-48 nanoparticles were diluted to approximately 1 wt % in ethanol by bath sonication for 30 minutes. Approximately 100 μl of the resulting dispersion was added on a glass cover slide attached with a double-sided carbon tape to an SEM stub, and dried to room temperature. Afterwards, the samples were coated by gold sputtering prior to the measurement.

Figure 2.1. Photograph of the JEOL JSM-7001F scanning electron microscope used for the SEM measurements.

2.3.4. Transmission Electron Microscopy

Transmission electron microscopy (TEM) is a microscopy that uses an electron beam with high energy to shine through ultrathin specimens or suspensions on grids. The interactions between the electrons of the beam and the atoms of the sample as the beam is transmitted through the sample are used to form an image. The basic operating principles of a transmission electron microscope are very similar with a light microscope but instead of light it uses electrons with much smaller wavelengths. Therefore, the resolution for TEM images are many orders of magnitude smaller than the resolution seen in a light microscope which enables the instrument to reveal fine details of the specimens as small as individual atoms.[6]

A probe side aberration corrected JEOL 2100FCs transmission electron microscope, operating at 200 kV, was used to capture conventional TEM images. For the preparation of the samples, MCM-48 nanoparticles were diluted to approximately 0.1 wt % in ethanol by bath sonication for 40 minutes. Approximately 50 μl of the resulting dispersion was added on gold TEM grid and dried to room temperature.

2.3.5. Scanning transmission electron microscopy

Scanning transmission electron microscopy (STEM) combines principles from SEM and TEM. A typical STEM microscope is a conventional type of TEM microscope equipped with additional tools and detectors that allow to use other types of signals such as secondary electrons, energy dispersive X-ray spectroscopy, electron energy loss spectroscopy and scattered beam electrons. Similarly with TEM, the interactions between the electrons of the beam and the atoms of the sample as the beam is

transmitted through the sample are used to form an image. However, unlike conventional TEM, STEM focuses the electron beam on a particular spot as small as 1 nm at a thin sample which is then scanned in a raster pattern over the area of interest.

A probe side aberration corrected JEOL 2100FCs transmission electron microscope, operating at 200 kV, was used to capture STEM bright field (BF) and high angle annular dark field (HAADF) images. STEM was used to record z-contrast images, scattered electrons were collected by a HAADF detector over a semi-angle ranging from 75 to 195 mrad. For the preparation of the samples, MCM-48 nanoparticles were diluted to approximately 0.1 wt % in ethanol by bath sonication for 40 minutes. Approximately 50 μl of the resulting dispersion was added on gold TEM grid and dried to room temperature.

2.3.6. Diffuse reflectance infrared Fourier transform spectroscopy

Diffuse reflectance infrared Fourier transform spectroscopy (DRIFT) is a well-known characterisation technique for fine particles and powders that collects and analyses scattered infrared energy. When the infrared light is focused onto a sample's surface, the incident beam can interact with the sample in one of the following ways: light can be adsorbed, reflected from the surface, or it can penetrate the sample before being scattered. The scattered light is then collected and relayed to the IR detector, where the absorption by chemical groups is revealed.[7] A DRIFT accessory directs the IR energy into a sample cap filled with a mixture of the sample and a non-absorbing matrix (e.g. KBr). The IR radiation interacts with the sample

and then reflects off its surface, causing the light either to diffuse or scatter, as it moves throughout the sample. The output mirror then directs this scattered energy to the detector in the spectrometer. The detector records the altered IR beam as an interferogram signal, which can then be used to generate a spectrum. A typical background is collected for the DRIFT cup filled with just the IR non-absorbing matrix.[8]

Chemical analysis of the pristine and modified MCM-48 samples was performed using DRIFT spectroscopy. The DRIFT spectra of the samples were obtained in a Bruker TENSOR II FTIR spectrometer equipped with a diffuse reflectance accessory (EasyDiff, Pike Technologies, Madison, WI, USA) (**Figure 2.2**). For the preparation of the samples, a small quantity of pristine or modified MCM-48 (approximately 10 wt %) was mixed with KBr by using a pestle and mortar. After fine grinding, the powder sample was placed in the DRIFT micro-cup. Finely grinded KBr was used as a background. All spectra were recorded within the range of 4000-400 cm^{-1} with resolution 4 cm^{-1} and 128 scans, and submitted to background spectrum subtraction.

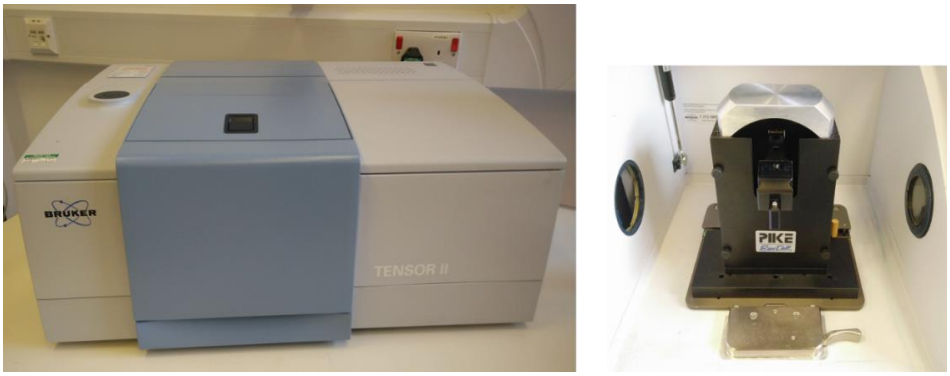

Figure 2.2. Photograph of Bruker TENSOR II FTIR spectrometer (left) and diffuse reflectance accessory EasyDiff, Pike Technologies, Madison, WI, USA (right) used to obtain the DRIFT spectra of the samples.

2.3.7. Thermogravimetric analysis

Thermogravimetric analysis (TGA) was used to determine:

- The calcination process for the removal of the surfactant from the pristine mesoporous silica nanoparticles was successful and all the surfactant was removed.
- The thermal stability of the pristine MCM-48 materials.
- The amount of the covalently attached QASs on the surface of the pristine MCM-48
- The amount of loaded biocide Parmetol S15 in the QAS-modified MCM-48.

The TGA curves were obtained at a Linseis STA PT-1000 top loading thermobalance (**Figure 2.3**). The samples were exposed to temperature increase from room temperature up to 800 °C with a ramp of 10 °C per minute under nitrogen atmosphere. All of the samples were dried at 50 °C under high vacuum prior the measurements.

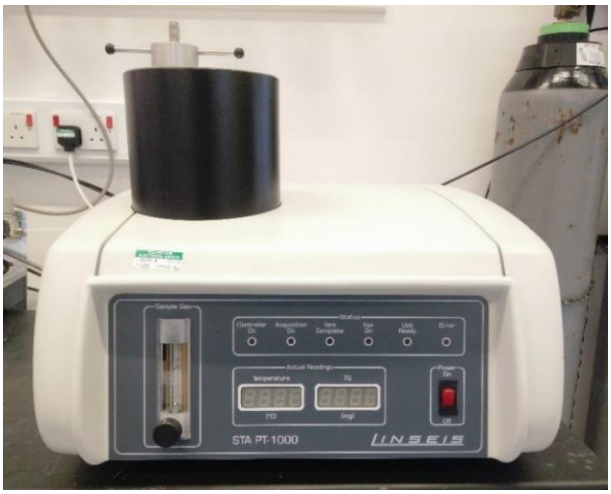

Figure 2.3. Linseis STA PT-1000 top loading thermobalance used for the thermogravimetric analysis.

2.3.8. ζ-potential measurements

When a particle comes in contact with a liquid, it acquires an electronic charge on its surface. The ζ-potential is an electrokinetic potential parameter in colloidal dispersions indirectly determined by the surface charge of particles when suspended in polar media.[9] Through the manipulation of ζ-potential, we can get information regarding the stability of colloidal dispersions. Colloids with high absolute number of ζ-potential are electrically stabilised while colloids with low values of ζ-potential tend to form aggregates. ζ-potential values from ±30 to ±40 mV indicate moderate stability while values from ±40 to ±60 mV indicate good stability.

We used ζ-potential measurements in order to obtain further information about the surface properties of the modified and unmodified materials, and their stability in pH range of 1.5-9.5. For the preparation of the samples, either pristine or QAS modified MCM-48 nanoparticles were diluted to approximately 0.1 wt % in water solutions with different pH values by bath sonication for 40 minutes. The water solutions with different pH values were prepared with diluted HCl and NaOH. The ζ-potential measurements were operated at a Malvern Zetasizer Nano ZS instrument (**Figure 2.4**) using folded capillary zeta cells (DTS1070, Malvern Panalytical).

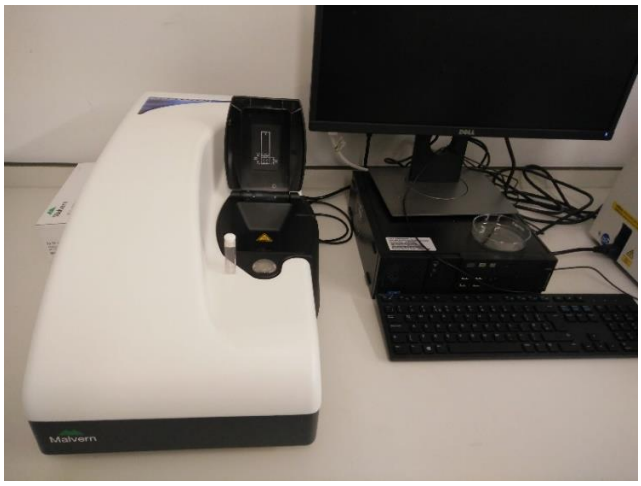

Figure 2.4. Malvern Zetasizer Nano ZS used for the ζ-potential measurements of colloidal nanoparticles.

2.3.9. Elemental analysis

Elemental analysis of carbon, hydrogen and nitrogen was performed for the pristine and QAS modified MCM-48 in order to obtain quantitative information about the samples' composition. CHN elemental analysis is an analytical technique that is based on the complete and instaneous oxidation of the sample by flash combustion. According to this technique, a sample is placed in a tin container and is burned in excess of oxygen. All the inorganic and organic substances are converted to combustion products, pass through a reduction furnace and are directed to a chromatographic column. Then, the individual components are separated and eluted as nitrogen (N_2), carbon dioxide (CO_2) and water (H_2O) with the help of a thermal conductivity detector.[10]

The CHN elemental analysis was performed in a FlashEA 1112 Analyzer (Thermo Fisher Scientific) (**Figure 2.5**). The powder samples were dried under vacuum

overnight prior the measurement. We used approximately 10 mg of sample for each measurement.

Figure 2.5. FlashEA 1112 Analyzer by Thermo Fisher Scientific used for the elemental analysis of pristine and modified MCM-48.

2.3.10. Hydrogen nuclear magnetic resonance

Hydrogen nuclear magnetic resonance (^{1}H-NMR) spectroscopy was used to confirm the successful synthesis of dimethyltetradecyl [3-(triethoxysilyl) propyl] ammonium chloride (by reacting N,N-dimethyltetradecylamine with 3-chloropropyltriethoxy silane). ^{1}H-NMR spectra of the two reactants (N,N-dimethyltetradecylamine and 3-chloropropyltriethoxy silane) and the resulting product {dimethyltetradecyl [3-(triethoxysilyl) propyl] ammonium chloride} were recorded in deuterated chloroform using a Bruker Avance I 400 MHz spectrometer equipped with a 60-position sample changer (**Figure 2.6**).

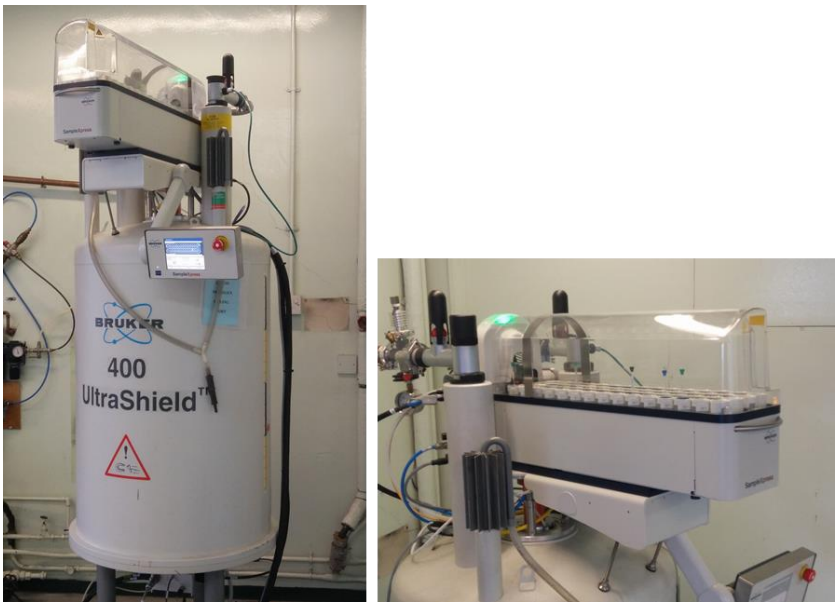

Figure 2.6. Bruker Avance I 400 MHz spectrometer equipped with a 60-position sample changer, used for the ^{1}H-NMR spectra.

2.3.11. Spin coating

Spin coating is a simple and straight forward technique to do deposition of uniform coatings of organic materials or to apply uniform distribution of particles on various flat substrates. The technique offers the advantage to apply uniform films with thickness varying from few nanometres to several microns in very short time. In a typical spin coating process, the coating material is dispersed in an appropriate solvent which is usually volatile. A small amount of the dispersion is placed on the centre of the substrate which is either rotating at low speed or is stationary. Then, the substrate starts to spin in high speed and because of the created centrifugal force, the coating material is spread uniformly to the substrate's surface. The spinning continues until the desired thickness is achieved and the applied solvent is

evaporated. Typically, a conventional spin coater allows controlling parameters such as rotating speed, time and acceleration of each individual step during the deposition process.

In our work, we used a Laurell WS-650MZ-23NPP/UD2 spin coater in order to apply uniform distribution of pristine and QAS modified MCM-48 on the surface of glass substrates for the antibacterial tests. For the preparation of the samples, 22 mm x 22 mm glass slides were spin-coated by 1 mL of either pristine or modified nanoparticles dispersed in ethanol solution (2 wt %).

2.4. Characterisation techniques: nanocontainer-doped coating formulations and coated PVC plates/panels

2.4.1. Focused ion beam scanning electron microscopy

Focused ion beam scanning electron microscopy (FIB-SEM) was used to obtain cross-sectional images of the pristine and nanocontainer-doped coating formulations. The operating principle for FIB-SEM systems is similar to SEM systems and it is a widely used technique in materials science. As the name indicates, FIB setups use a focused beam of ions rather than a focused beam of electrons used from conventional SEM systems. FIB systems use gallium as primary ion beam which hits the surface of specimens and sputters a small amount of material. The FIB is a destructive technique for the specimens which can be used to etch or “mill” surfaces

with precision in nanoscale. The FIB-SEM systems have incorporated both types of beams; the SEM focused electron beam provides high resolution images while the FIB tool allows to modify the samples' surfaces.

For the preparation of the samples, small PVC plates (typically 10 mm X 10 mm) coated either with the pristine or nanocontainer-doped paints were attached with a double-sided carbon tape to an SEM stub. Afterwards, the samples were coated by gold sputtering prior to the measurement. The measurements were performed with a FEI Helios Nanolab 600i dual-beam FIB-SEM at the nanoinvestigation centre in Liverpool (**Figure 2.7**).

Figure 2.7. FEI Helios Nanolab 600i dual-beam FIB-SEM used for the cross-sectional images of pristine and nanocontainer-doped paints.

2.4.2. Fineness of grind

Grindometers or fineness of grind gauge are precision instruments to determine how finely grounded the particles of solid materials are dispersed in a coating, paint, ink, etc. The gauges are made of hardened steel and consist of one or two etched parallel grooves which decrease in depth from one side end of the block to the other. The two channels of grooves can vary in depth from 100 μm to 0. In a typical test, a small volume of sample is placed on the deep side of the groove and a straight scraper is used to drawn down the sample toward the shallow end. For the determination of the fineness of grind, the reading is taken from the marked scale next to the grooves where regular oversize particles and their tracks start to appear.

For the measurements of our samples, we used approximately 3 mL of either pristine or nanocontainer-doped paint. The process repeated at least 9 times with a two channel grindometer (Ascott Analytical Equipment Limited) and the results were averaged.

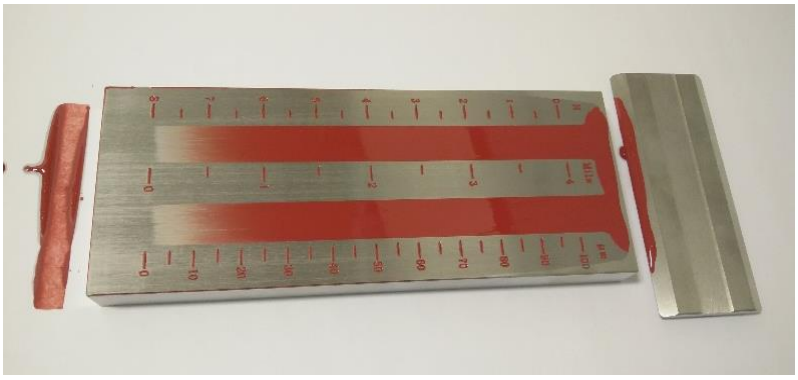

Figure 2.8. Nanocontainer-doped paint applied on a two channel grindometer for the determination of fineness of grind.

2.4.3. Contact stylus profiler

A surface profiler or profilometer is a common measuring instrument used to measure a surface's features such as roughness. A contact stylus profiler uses a probe (stylus) to detect the surface as the probe moves along the exposed surface in continuous contact. There is a constant force between the probe and the exposed surface which allows to monitor and record vertical displacements of the probe along the scan providing surface height and roughness information. In this work, we used an Ambios XP200 contact stylus profiler to record the average surface roughness of coated PVC plates (5 cm X 5 cm) with pristine or nanocontainer-doped paints.

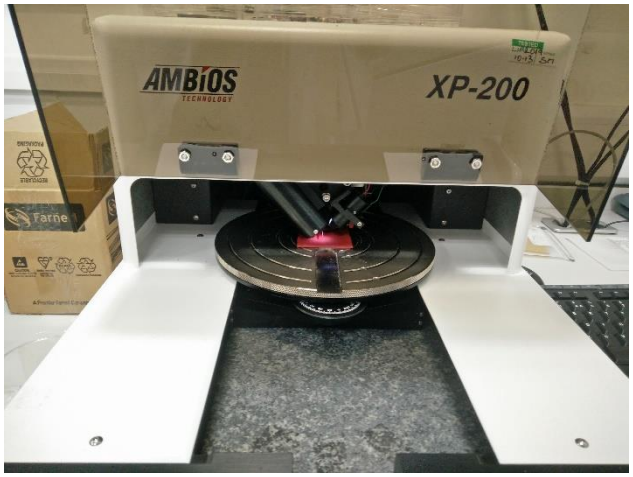

Figure 2.9. Ambios XP200 contact stylus profiler used for the surface roughness measurements of coated PVC plates.

2.4.4. Non-contact 3D optical profiler

Non-contact 3D optical profilers are interference microscopes and are used for surface measurements such as film thickness and height variations for surface roughness. Some of the advantages of using an optical profiler are:

- There is no contact between the sample and profiler, thus, there is no damage of sample's surface.
- Provides three dimensional measurements.
- Extremely high resolution for surface roughness, up to 50 nm.
- Quick measurement for large scanned area.
- Inexpensive consumable parts to replace.

In our studies, 7 cm X 10 cm coated PVC panels with pristine or nanocontainer-doped paints were scanned with a 3D non-contact optical profiler Talysurf CCI-HD (Taylor-Hobson) in order to obtain information for their surface roughness values (**Figure 2.10**). The scanned area for each panel was 100 mm^2.

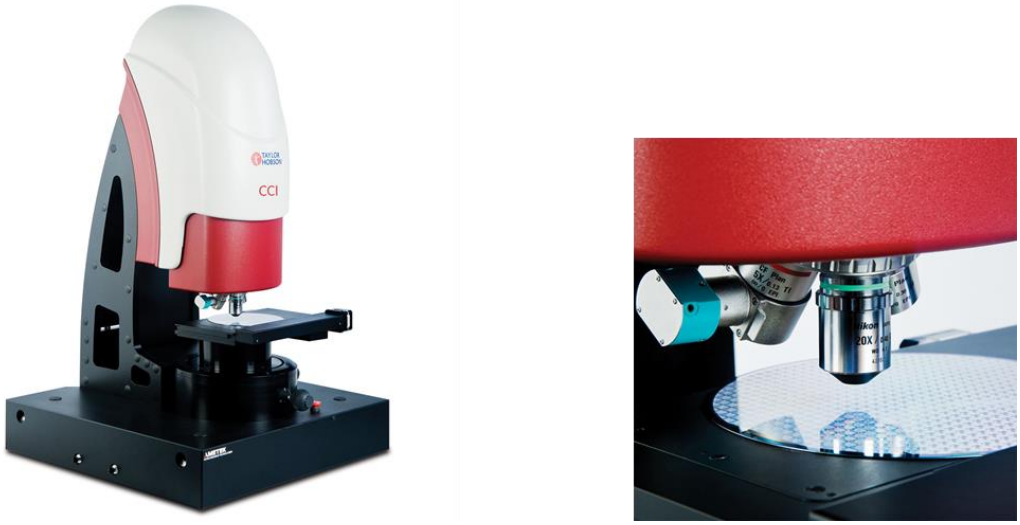

Figure 2.10. 3D non-contact optical profiler (Talysurf CCI-HD, Taylor-Hobson) used for the surface roughness measurements of coated PVC panels.

2.4.5. Contact angle

The contact angle is the angle where a liquid-vapour interface meets a given solid surface. Usually, the probing liquid is water and the measured contact angle is referred as water contact angle. In general, a surface is called hydrophilic if the measured contact angle value is less than 90°, whereas it is called hydrophobic if the measured contact angle value is greater than 90°. Surfaces that show contact angle values greater than 150° are called superhydrophobic.

There are three regimes that describe the balance of forces acting on a liquid droplet spreading on a surface (**Figure 2.11**).[11] The first one who introduced an equation to quantify the wettability of a surface by a liquid was Young in 1805.[12] Young's regime applies on theoretical ideal surface which is atomically smooth and chemically homogeneous. Thus, it is difficult to find in nature a perfectly smooth and flat surface as assumed in Young's approach. In more realistic approaches, the non-ideal solid surfaces found in nature are both rough and chemically heterogeneous. In 1936, Wenzel defined the relationship between the wettability and the surface roughness of a solid surface.[13] The so-called Wenzel regime predicts that by introducing roughness to a homogeneously wetted surface will either increase the hydrophilicity or hydrophobicity of the sample, depending on whether the initial tested surface is hydrophilic or hydrophobic, respectively. Later in 1944, Cassie-Baxter introduced an equation to describe chemically heterogeneous surfaces where the liquid does not penetrate into the grooves and the water droplet sits on patchwork of solid and air pockets trapped between the solid surface and the liquid.[14]

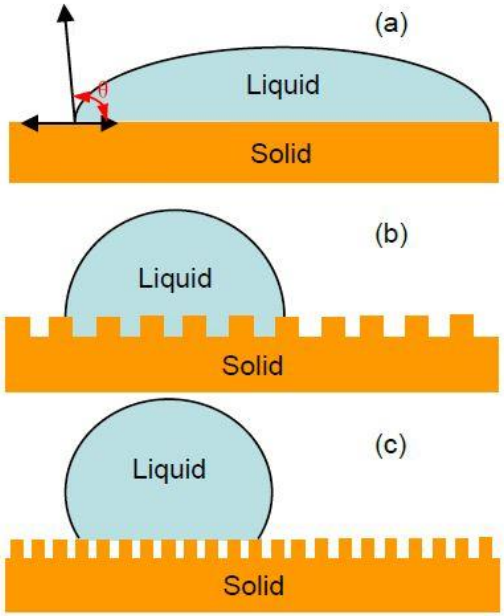

Figure 2.11. Schematic illustration of Young's (a), Wenzel (b) and Cassie (c) regimes.[11]

For measurement of water contact angle values, PVC plates 5 cm X 5 cm were coated with the pristine paint and the four nanocontainer-doped paints. We used three coated PVC replicates for each type of paint and the water contact angles were obtained in three different areas for each replicate. Afterwards, the overall values for each type of paint were averaged. The water contact angle values of the coated plates were obtained with an Attension Theta (Biolin Scientific) contact angle meter interfaced to drop shape analysis software (**Figure 2.12**).

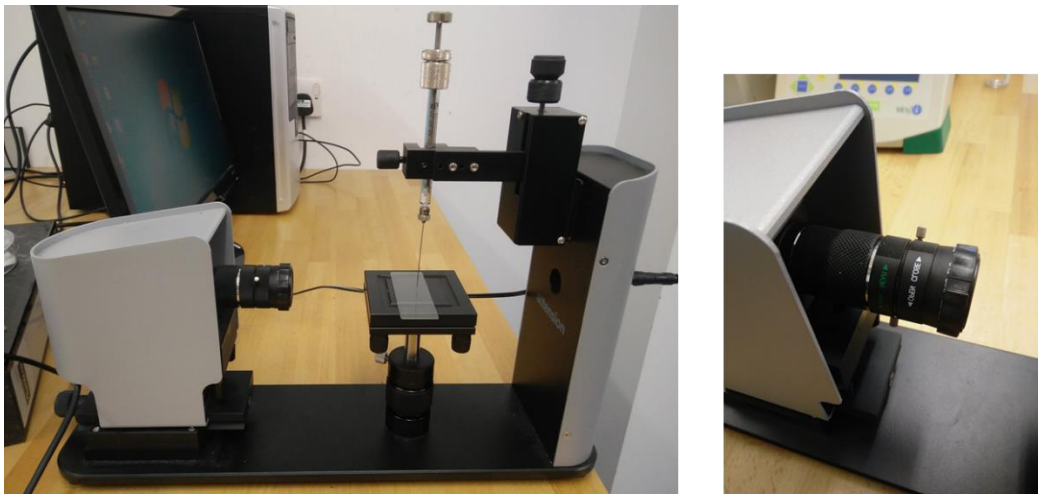

Figure 2.12. Attension Theta (Biolin Scientific) contact angle meter used for measuring the contact angle of droplets on coated PVC plates.

References

[1] S. Brunauer, P. H. Emmett, E. Teller, *J. Am. Chem. Soc.* **1938**, *60*, 309.

[2] C. Lastoskie, K. E. Gubbins, N. Quirke, *J. Phys. Chem.* **1993**, *97*, 4786.

[3] J. Landers, G. Y. Gor, A. V. Neimark, *Colloids Surfaces A Physicochem. Eng. Asp.* **2013**, *437*, 3.

[4] P. I. Ravikovitch, S. C. O. Domhnaill, A. V. Neimark, F. Schueth, K. K. Unger, *Langmuir* **1995**, *11*, 4765.

[5] D. C. J. Joseph I. Goldstein, Dale E. Newbury, Joseph R. Michael, Nicholas W.M. Ritchie, John Henry J. Scott, *Scanning Electron Microscopy and X-Ray Microanalysis*, Springer, US, Boston, MA, **2003**.

[6] B. Fultz, J. M. Howe, *Transmission Electron Microscopy and Diffractometry of Materials*, Springer, **2007**.

[7] G. Accardo, R. Cioffi, F. Colangelo, R. D'Angelo, L. De Stefano, F. Paglietti, *Materials (Basel).* **2014**, *7*, 457.

[8] ThermoFisherScientific, "FTIR Sample Techniques - Diffuse Reflectance (DRIFTS)," can be found under www.thermofisher.com, **2018**.

[9] J. Antonio Alves Júnior, J. Baptista Baldo, *New J. Glas. Ceram.* **2014**, *4*, 29.

[10] "CHN Elemental Microanalysis, UCL SCHOOL OF PHARMACY," **2018**.

[11] Song, *Nord. Pulp Pap. Res. J.* **2013**, *28*, 216.

[12] T. Young, *Philos. Trans. R. Soc. London* **1805**, *95*, 65.

[13] R. N. Wenzel, *Ind. Eng. Chem.* **1936**, *28*, 988.

[14] A. B. D. Cassie, S. Baxter, *Trans. Faraday Soc.* **1944**, *40*, 546.

Chapter 3: Mesoporous Silica Nanoparticles: Synthesis & Characterisation

3.1. Introduction

The discovery of ordered mesoporous silicas was first reported by Mobil's scientists and Japanese scientists in the early 1990s using cationic organic surfactants as structure-directing agents (templates) in order to synthesise ordered pore structure materials.[1–4] Since then, the templating method has been widely used to prepare mesoporous silica nanoparticles with high surface are values (up to 1500 m^2/m), controlled and tuneable pore sizes (1.5-10 nm), tuneable particle size, high pore volumes and different morphologies.[5] By controlling the reaction conditions (such as reaction pH, temperature, silica source, surfactant concentration, etc.) and because of surfactants can assembly in different mesophases and morphologies, the surfactant-templated method can be used in order to obtain mesoporous silicas with various mesostructures (disordered, cubic, hexagonal, lamellar, wormhole-like mesophases), morphologies (spheres, hollow spheres, fibers, helical fibers, tubules, gyroids) and dimensions (from nm to cm).[6]

Over the past decade, MSNs have been widely used in catalysis, sensors, separation, encapsulation, nanodevices and biomedical applications because of their unique uniform mesoporous structure, two functional surfaces (internal into the pore channels system and external particle surface) and good biocompatibility.[11–13] Among the different types of MSNs, Mobil's M41S family of mesoporous molecular sieves received huge attention due to their well-defined pore structures. Mobil composition of matter (MCM)-41 (with a hexagonal arrangement of mesopores, space group *p6mm*) is undoubtedly the most well-known and most extensively researched material of this family. Other discrete representatives of the M41S family

are the MCM-48 (with a cubic arrangement of mesopores, space group *Ia3d*) and MCM-50 (with a laminar structure, space group *p2*) forms (**Figure 3.1**).[14,15]

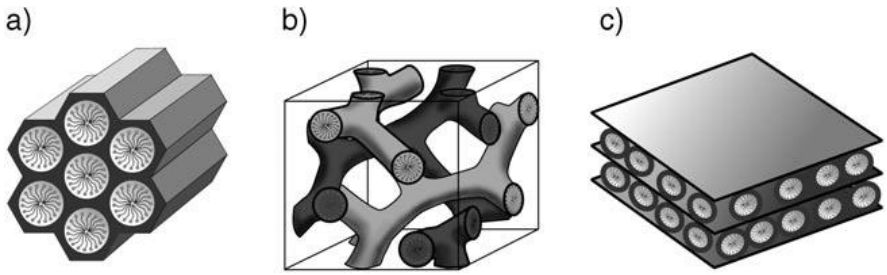

Figure 3.1. Structures of mesoporous M41S materials: a) MCM-41 (2D hexagonal, space group *p6mm*), b) MCM-48 (cubic, space group *Ia3d*) and c) MCM-50 (lamellar, space group *p2*).[15]

As an important member of the M41S family, considerable attention has been paid to MCM-48 because of its unique three-dimensional (3D) bicontinuous cubic mesostructure. Different from the unidirectional 2D hexagonal channels of MCM-41, the 3D gyroid bicontinuous channels of MCM-48 are considered to be useful for fast molecule transport and easy molecular accessibility.[16] Materials with 3D pore channels are considered to be more advantageous for the loading and release of guest molecules for encapsulation, catalytic and other applications since they are less prone to the pore blocking and should allow a faster diffusion of reactants through the material.[17] On the other hand, their synthesis and characterisation is more difficult and more complicated.

This chapter will present and discuss the synthesis and characterisation of spherical MCM-48 MSNs with two different average sizes (400 nm and 120 nm) as potential carriers of antibacterial and antifouling compounds. MCM-48 spherical

nanoparticles (NPs) were chosen for two main reasons. First, their interwoven, branched 3D mesostructure makes them excellent candidates for the loading and release of active molecules with antibacterial/antifouling properties (e.g. biocides, fungicides, disinfectants, etc.). Second, these materials can be easily functionalized with several compounds, as they exhibit high surface reactivity because of the existence of the hydroxyl groups on their surface. The morphological properties and the quality of the mesoporous channel system for the synthesised materials were evaluated by several techniques and the successful synthesis of highly ordered spherical MCM-48 with two different average sizes was confirmed.

3.2. Experimental

3.2.1. Synthesis of mesoporous silica nanoparticles with average size of 400 nm.

The modified Stöber's method was used for the synthesis of MSNs as reported from Schumacher et al.[18,19] According to this method, spherical MCM-48 can be synthesized at room temperature which provides a faster synthetic procedure compared to the traditional hydrothermal pathway. Hexadecyltrimethylammonium bromide (2.6 g) was dissolved in a mixture of deionized water (120 mL) and pure ethanol (50 mL), and ammonium hydroxide (12 mL of 32 wt % solution) were added to the surfactant solution. The solution was stirred for 10 minutes at 600 rpm and tetraethyl orthosilicate (3.4 g) was added at once during stirring. After stirring for 16 hours at room temperature the resulting solid was recovered by filtration, washed

twice with ethanol, twice with distilled water and dried in air at ambient conditions. The organic template was removed by calcination in a muffle furnace at 550 ºC for 6 h after heating with a ramp of 1 ºC/min.

3.2.2. Synthesis of mesoporous silica nanoparticles with average size of 120 nm.

The modified Stober's method used for the synthesis of MSNs as reported from Kim et al. [20]. According to this method, CTAB (0.5 g) and Pluronic F127 (2.05 g) are dissolved in distilled water (96 mL), EtOH (34 g) and ammonium hydroxide (10.05 g of 29 wt % solution) at room temperature. After complete dissolution, TEOS (1.8 g) was added into the mixture at once. After 1 min of mechanical stirring at 1000 rpm, the mixture was kept at a static condition for 24 hours at room temperature for further silica condensation. The white solid product was recovered by ultrahigh speed centrifuge, washed with water, and dried at 70 ºC in air. The final template free MCM-48 MSN materials were obtained after calcination in a muffle furnace at 550 ºC for 6 h after heating with a ramp of 1 ºC/min.

3.3. Results and discussion

3.3.1. Mesoporous silica nanoparticles with average size of 400 nm.

3.3.1.1. Powder X-ray diffraction pattern.

The X-ray diffraction data can provide useful information about the structure properties of MSNs. The powder XRD pattern of the template-free synthesised MCM-48 after calcination (**Figure 3.2**) is similar to the literature data.[18] The samples exhibit five distinct Bragg diffraction peaks in the range 2θ= 1.5-10° which correspond to the planes (211), (220), (420), (332) and (431). The diffraction peaks can be assigned to the typical cubic space group *Ia3d* characteristic for mesoporous materials with 3D cubic structure. The planes (211) and (220) are intense and sharp which is an indication of high ordering of our synthesised MCM-48. In the reaction mixture, the MCM-48 NPs are formed within a few minutes after the addition of TEOS, but the XRD peaks become sharper and show higher intensities after 2 hours.[18] During our experimental procedure, the solution was left under stirring for 16 hours before the collection of the solid materials. According to the literature, a longer stirring time is required in order to promote further silica condensation that could prevent the shrinkage of the mesostructure during the calcination process for the removal of the template.[20,21] Melendez-Ortiz *et. al.* studied the influence of reaction conditions for MCM-48 silica obtained in room temperature and they concluded that samples which are synthesised for 14 hours or longer show better stability, when temperature is raised, as well as high ordering of the mesoporous channels.[21]

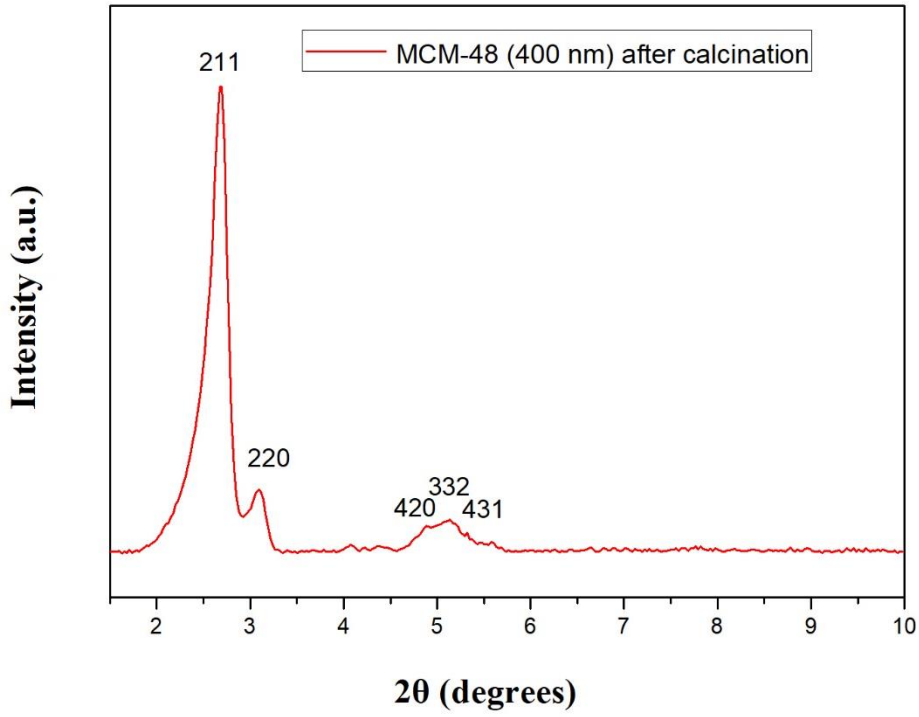

Figure 3.2. XRD patterns for the synthesised MCM-48 mesoporous nanoparticles (400 nm average size), planes (211), (220), (420), (332) and (431) correspond to the cubic space group *Ia3d*.

3.3.1.2. Nitrogen Adsorption/Desorption Isotherms.

The low-temperature nitrogen isotherms can provide accurate and reliable information associated with the specific surface area and the quality of the mesoporous structure of solid materials.[22] **Figure 3.3 a** shows the nitrogen adsorption/desorption isotherms for MCM-48 material obtained at 77 K. The sample presented type IV isotherm according to the Brunauer-Deming-Deming-Teller classification which is characteristic for MCM-41 and MCM-48 mesoporous materials.[23] No hysteresis was observed between the adsorption and desorption isotherm. A sharp capillary condensation step can be observed from the inflection point at relative pressures P/P_0 between 0.22 and 0.32 providing information for the

uniformity of the pore channels and the narrow pore size distribution (**Figure 3.3 a**).[24–27]

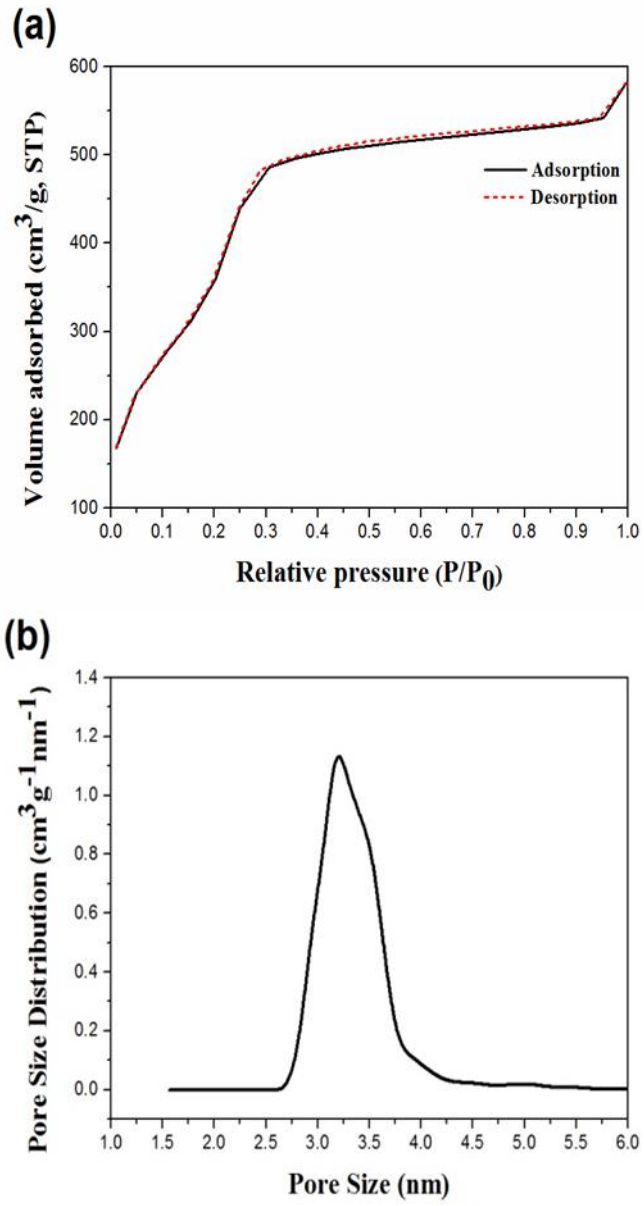

Figure 3.3. Synthesised MCM-48 mesoporous silica nanoparticles with average size of 400 nm: (a) Nitrogen adsorption-desorption isotherms at 77 K and (b) pore size distribution.

The specific surface area was calculated according to the Brunauer - Emmett - Teller (BET) method.[28] Data of relative pressure P/P_0 between 0.01 and 0.16 were used for

the calculation of the BET specific area (S_{BET}, cross sectional area of nitrogen molecule based on 16.2 $Å^2$). The mesoporous MCM-48 samples exhibited high values of S_{BET} in a range from 1180 to 1300 m^2/g. The most common methods used for the calculation of the pore size distribution and the average pore volume are the Barrett-Joyner-Halenda (BJH) and Horvath-Kawazoe (HK) methods.[19,22,29,30] However, the accuracy of these methods is limited for materials with pore sizes in the nanometer range. Characteristic problems of these methods are related to the overprediction of the relative pressures for the capillary condensation steps and the underestimation of the pore diameters.[31–34] For that reason, the pore size distribution and the total pore volume of the synthesised MCM-48 materials were calculated from the nitrogen adsorption isotherms by using the nonlocal density functional theory (NLDFT) method.[35–37] It has been well documented that the NLDFT model is more accurate and rigorous approach for the interpretation of the nitrogen isotherms and the calculation of mesoporous structure properties for MCM-48 materials.[18,19,38,39] The synthesised MCM-48 material presented high total pore volume of 0.8 cm^3/g at 0.99 relative pressure. Furthermore, the material under study exhibited narrow pore size distribution as expected due to the sharp capillary condensation step (**Figure 3.3 b**). The average pore diameter is 3.2 nm as calculated from the NLDFT method.

3.3.1.3. Morphological studies.

Scanning electron microscopy (SEM) was used to observe the morphology of the samples. The SEM images of the mesoporous MCM-48 after calcination at 550 ^oC are shown in **Figure 3.4**. The samples showed spherical morphology in the range of

200-600 nm. In the reaction mixture, the presence of ammonia works as a morphological catalyst responsible for the spherical size of the particles.[40] As can been seen from the SEM images, some of the particles are aggregated and fused together but most of them are single monodispersed particles.

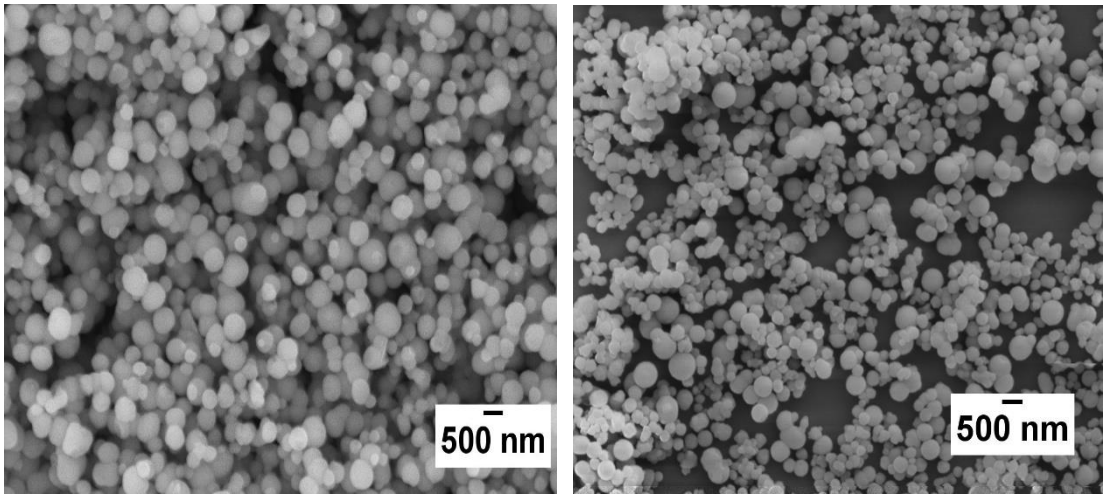

Figure 3.4. SEM images for the synthesised MCM-48 mesoporous silica nanoparticles with average size of 400 nm.

Further information regarding the morphology and the pore structure of the synthesised materials was obtained by transmission electron microscopy (TEM). **Figure 3.5** shows the TEM images for template-free mesoporous MCM-48 after calcination at 550 ^{o}C. The TEM images are in a good agreement with the SEM images showing the spherical shape of the particles and it is easier to observe the aggregation between the particles. Furthermore, the TEM images offer a visualisation of the pore structure. We can observe that each NP has a regular well-ordered mesopore arrangement over the whole particle. The TEM image allows one

to estimate the size of the pores but in this case the resolution of the images is not high enough to estimate the pore size. The NPs were too large or too thick and, as a result, it was difficult to obtain images with higher resolution in order to determine the size of the pores.

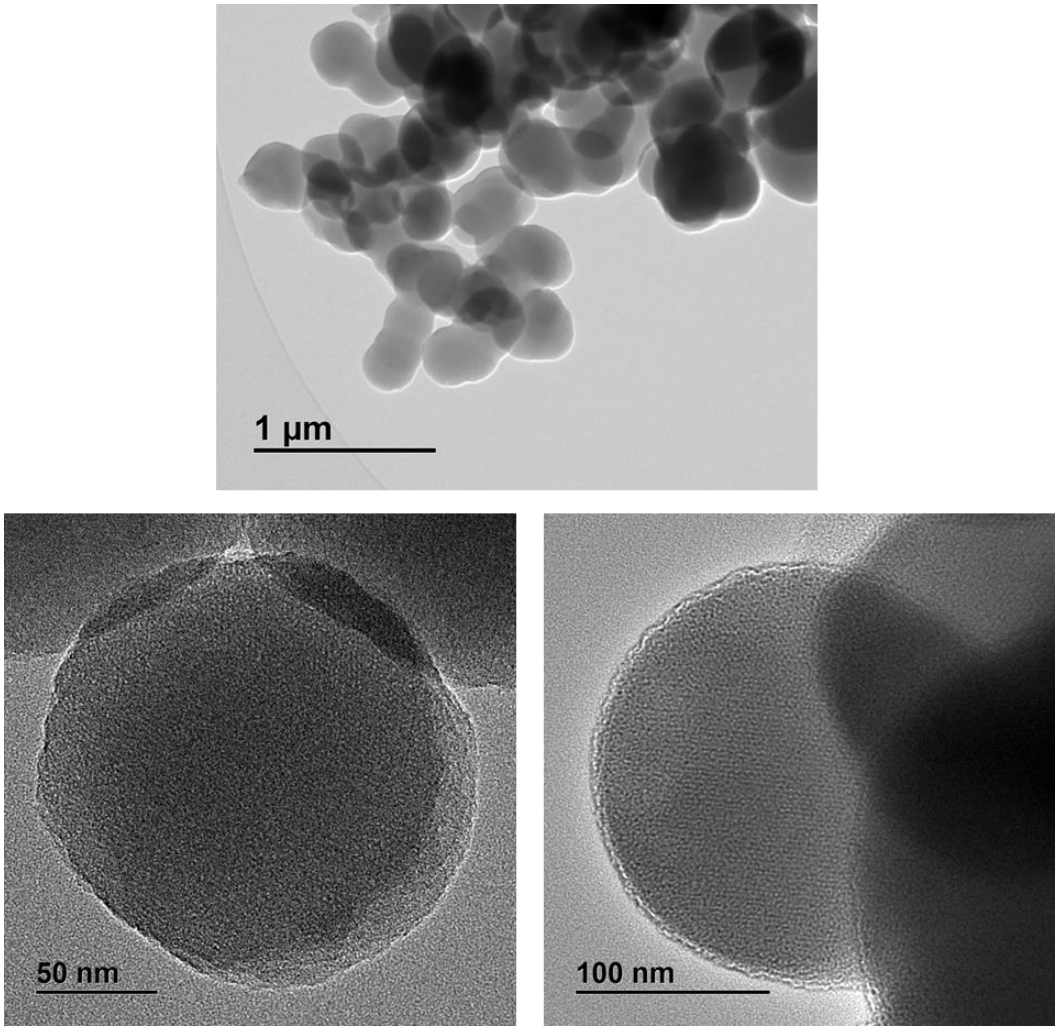

Figure 3.5. TEM images of MCM-48 mesoporous silica nanoparticles with average size of 400 nm.

3.3.1.4. Diffuse Reflectance Infrared Fourier Transform (DRIFT) spectroscopic analysis.

The DRIFT spectrum for the pristine MCM-48 after calcination at 550 ^{o}C is shown in **Figure 3.6**. The synthesised sample shows the characteristic absorption peaks for the SiO_2 materials: Si-O-Si bending vibration (465 cm^{-1}), Si-O-Si symmetric stretching (800 cm^{-1}), Si-OH asymmetric vibration (940 cm^{-1}), Si-O asymmetric vibration (1080 cm^{-1}), H-O-H bending vibration (1635 cm^{-1}) and –OH stretching (3400 cm^{-1}). The absence of peaks in the region of 1350-1480 cm^{-1} and 2850-3000 cm^{-1} (related to C-H bending and stretching vibrations) implies that the calcinated material is template-free and all of the surfactant was removed successfully during the calcination process. Furthermore, the high intensity of the broad –OH peak at 3400 cm^{-1} for the pristine MCM-48 is an indication that a significant number of free –OH groups on the surface and within the pore channel system of pristine MCM-48 remained even after the calcination. Another possible explanation for the intensity of this peak could be the presence of humidity or water in the sample. However, the samples were dried over night at 100 ^{o}C under high vacuum before getting the spectrum. Therefore, we can assume that the intensity of the peak is mostly because of the –OH groups of the sample.

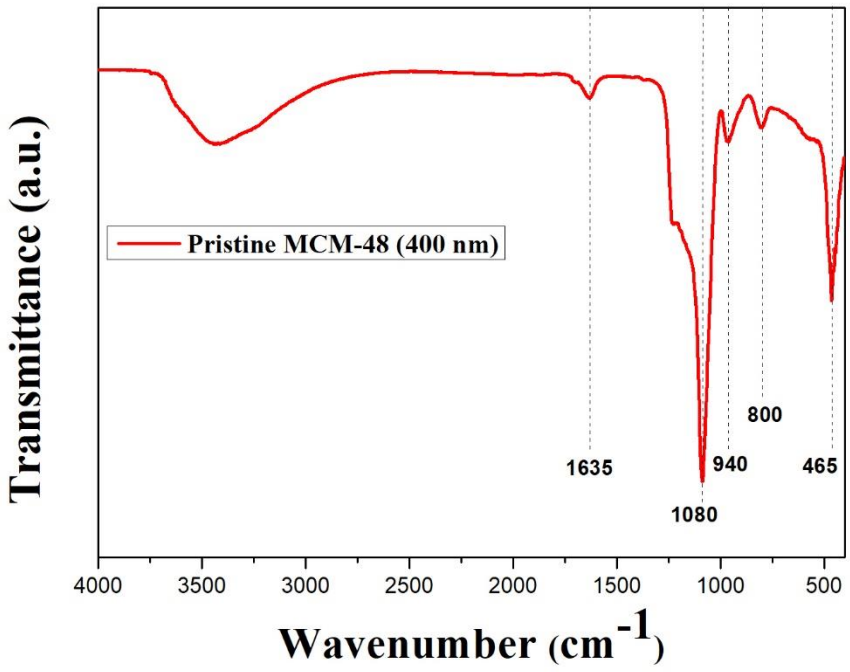

Figure 3.6. DRIFT spectrum for pristine MCM-48 mesoporous silica nanoparticles with average size of 400 nm.

Table 3.1. Wavenumbers for sample: pristine MCM-48 mesoporous silica nanoparticles with average size of 400 nm.

Pristine MCM-48 (400 nm)	
Wavenumber (cm^{-1})	**Assignment**
465	Si-O-Si bending vibration
800	Si-O-Si symmetric stretching
940	Si-OH asymmetric vibration
1080	Si-O asymmetric vibration
1635	H-O-H bending vibration
3400	–OH stretching

3.3.1.5. Thermogravimetric analysis (TGA).

The TGA was used to evaluate the successful removal of the surfactant and the thermal stability of the template-free MCM-48 when heated under N_2 atmosphere up to 800 ^oC (**Figure 3.7**). The pristine MCM-48 was calcinated up to 800 ^oC and its weight decreased only by 4%. The weight loss below 120 ^oC can be attributed mainly to thermodesorption of physically adsorbed water.[25] After the 120 ^oC, the MSNs exhibited high thermal stability and no additional weight loss was observed up to 800 ^oC. The silica NPs have very high thermal stability and keep their weight constant up to 800 ^oC. However, the mesoporous structure collapses above 750 ^oC, especially for MSNs prepared with TEOS.[41] The absence of further weight loss below 400 ^oC implies that the complete removal of the surfactant during the calcination process on synthetic stage was successful. Otherwise, a prominent weight loss between 200-400 ^oC should be observed due to the decomposition of organic species corresponding to surfactant.[25,42]

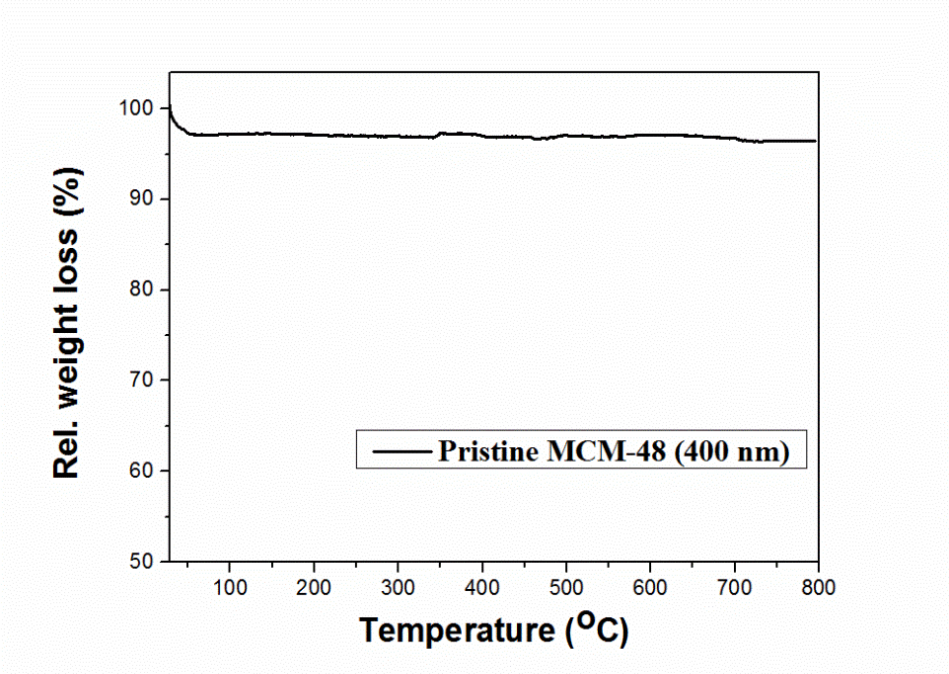

Figure 3.7. TGA curve for pristine MCM-48 mesoporous silica nanoparticles with average size of 400 nm.

3.3.2. Mesoporous silica nanoparticles with average size of 120 nm.

3.3.2.1. Powder X-ray diffraction pattern.

The XRD pattern of template-free MCM-48 obtained using a binary system of surfactants (CTAB and Pluronic F127) is illustrated in **Figure 3.8**. The sample shows five distinct Bragg diffraction peaks in the range of 2θ= 1.5-10° which correspond to the planes (211), (220), (420), (332) and (431). These peaks are similar to the literature and can be assigned to the *Ia3d* cubic space group, which is characteristic for mesoporous materials with 3D cubic structure.[20] The XRD pattern for the calcinated sample shows sharp and intense (211) and (220) planes which is typical for highly ordered MCM-48 materials. According to the synthetic procedure, after 1 min of mechanical stirring at 1000 rpm, the mixture was kept at a static

condition for 24 hours at room temperature prior to the recovery of the white solid product. As it is reported in the literature, longer synthesis time is essential in order to promote further silica condensation and form mesoporous materials with high ordering and stable mesostructure on high temperatures.[18,21] Therefore, this could explain the high mesostructure ordering of the synthesised material and the appearance of peaks with high intensity.

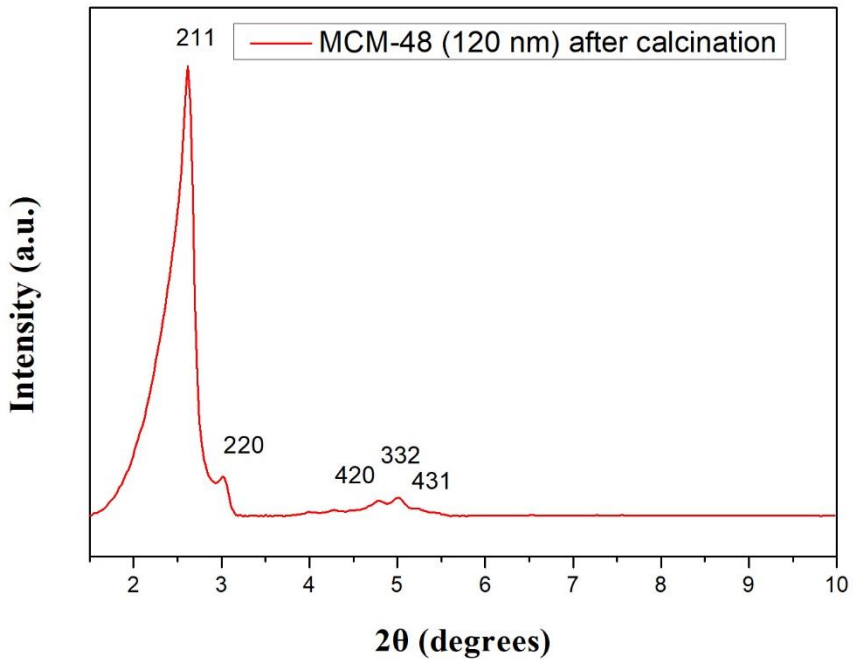

Figure 3.8. XRD pattern for the synthesised MCM-48 mesoporous nanoparticles (120 nm average size), planes (211), (220), (420), (332) and (431) correspond to the cubic space group *Ia3d*.

3.3.2.2. Nitrogen Adsorption/Desorption Isotherms.

The adsorption/desorption isotherms for the synthesised MCM-48 with average size of 120 nm obtained at 77 K are shown in **Figure 3.9 a**. The isotherms of the sample are of type IV according to the Brunauer-Deming-Deming-Teller classification

which is characteristic for mesoporous solids such as MCM-41 and MCM-48.[23] No hysteresis loop was observed between the adsorption/desorption isotherm, which means that there are no secondary pores and the capillary condensation behaviour of the sample can be considered reversible.[26] The sample's isotherms exhibit two capillary condensation steps. The first sharp capillary condensation step is appeared at a relative pressure of 0.18-0.3 and can be attributed to the nitrogen condensation that took place at the internal mesopores.[20] The sharpness of this step suggests a uniform size pore system and narrow pore size distribution.[24,25,27] The second capillary condensation step is observed at relative pressure above 0.95 and is related to interparticle voids, which indirectly reflects the size of particles; the higher step shows a small particle size.[20]

The specific surface area was calculated according to the Brunauer - Emmett - Teller (BET) method.[28] For the calculation of the BET surface area, we used data of relative pressure between 0.01 and 0.2. The synthesised MCM-48 with average size of 120 nm showed high values of BET surface area in a range from 1050 to 1120 m^2/g. The pore size distribution and the total pore volume of the synthesised MCM-48 materials with average size of 120 nm were calculated from the nitrogen adsorption isotherms by using the more accurate and rigorous approach of nonlocal density functional theory (NLDFT) method.[35,36,38] The synthesised MCM-48 material illustrated high total pore volume of 1.27 cm^3/g at 0.99 relative pressure. As can be seen in **Figure 3.9 b**, the pore size distribution is narrow (as expected from the first sharp capillary condensation step) with average pore diameter at 3.5 nm as calculated from the NLDFT method.

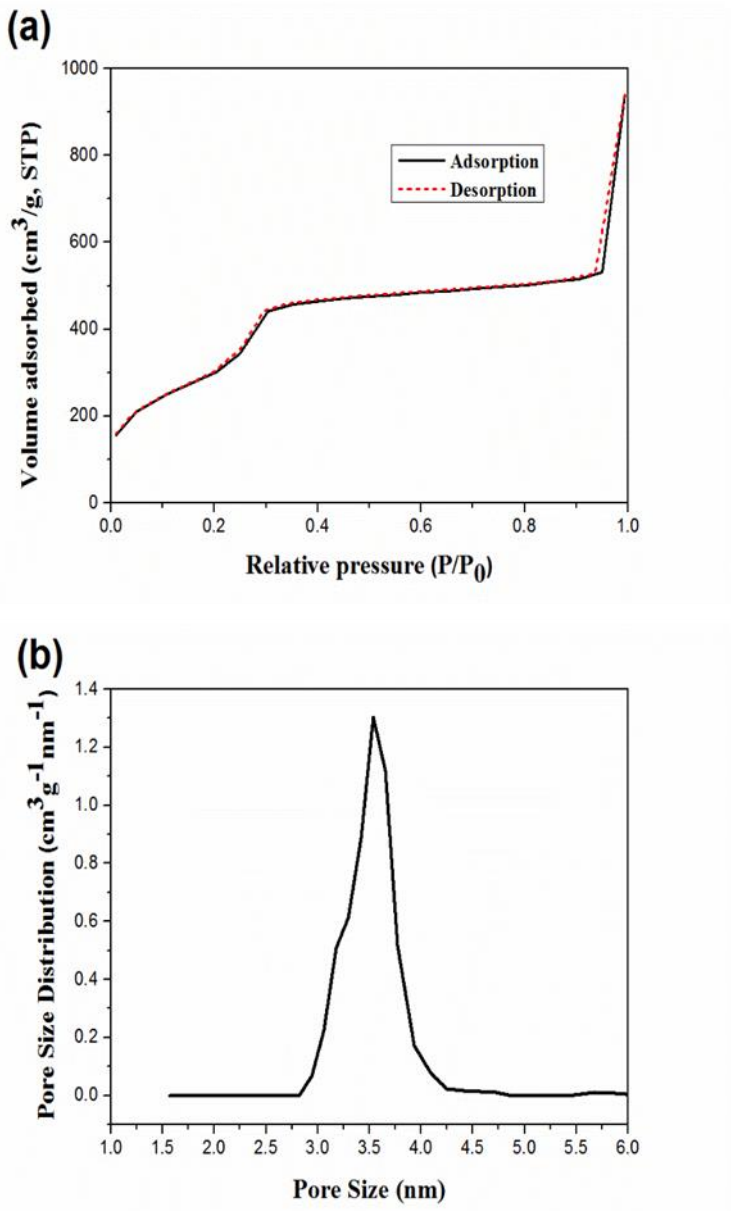

Figure 3.9. Synthesised MCM-48 mesoporous silica nanoparticles with average size of 120 nm: (a) Nitrogen adsorption-desorption isotherms at 77 K and (b) pore size distribution.

3.3.2.3. Morphological studies.

Scanning electron microscopy was used in order to obtain images of the synthesised template-free MCM-48 after calcination at 550 ^{o}C. As shown in **Figure 3.10**, the resulting NPs are perfectly spherical in shape and no agglomeration is visible. The

particle size is in the range of 90-170 nm with average size at 120 nm. As it is documented in the literature, the ammonia plays the role of the morphological catalyst which is responsible for the spherical size of the nanoparticles.[20] Furthermore, monodispersed MCM-48 without the deformation of structural properties was obtained by using the triblock copolymer Pluronic F127 which acts as dispersing agent and grain size tailor in the binary surfactant system. In the present synthesis method, the cationic surfactant CTAB is assembled with anionic silicates through electrostatic interactions in a basic solution, producing an ordered mesophase. The non-ionic surfactant Pluronic F127 interacts with the anionic silicates, limiting the growth of the mesostructure particle grain and creating a steric barrier. Thus, the particle size of the resultant mesoporous silica and the monodispersity of the particles can be determined from the inhibition caused by the interaction with Pluronic F127.[20]

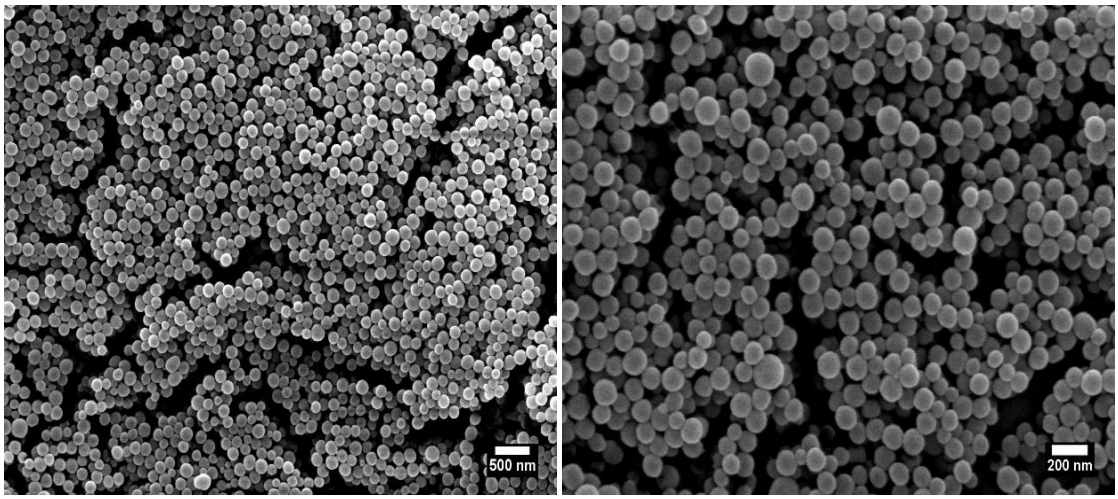

Figure 3.10. SEM images of monodispersed MCM-48 mesoporous silica nanoparticles with average size of 120 nm.

Further information for the morphology and the pore structure of calcinated template-free MCM-48 was obtained by scanning transmission electron microscopy (STEM) using a high-angle annular dark field (HAADF) detector. The HAADF images provide mass-thickness information; holes appear dark and dense regions bright. As shown in **Figure 3.11**, the STEM images clearly show that monodispersed NPs with perfectly spherical morphology were synthesised. The NPs are well-shaped and there is no aggregation or fused NPs together. The highly magnified STEM image shows that the NPs have well-ordered regular mesoporous structure extending over the whole particle. Furthermore, the small size and the good stability of the NPs under the STEM beam allowed us to obtain images with high resolution and magnification in order to determine the pore size at 3.5 nm which is in a good agreement with the analysis from the N_2 isotherms (**Figure 3.9)**. Additionally, the good resolution of the STEM images allowed us to estimate the wall thickness of the mesoporous channel system to approximately 12 Å.

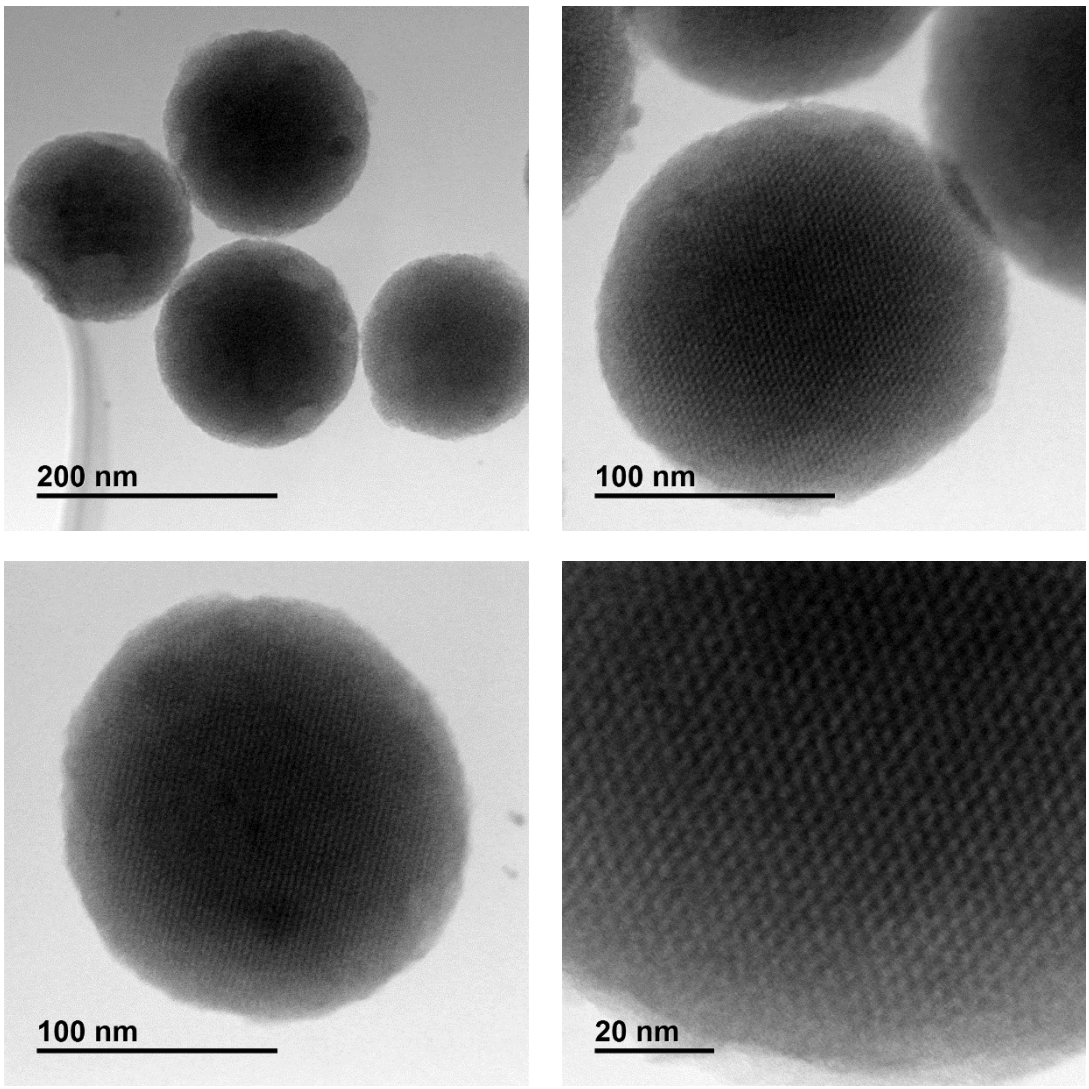

Figure 3.11. STEM images of monodispersed MCM-48 mesoporous silica nanoparticles with average size of 120 nm using an HAADF detector.

3.3.2.4. Diffuse Reflectance Infrared Fourier Transform (DRIFT) spectroscopic analysis.

Figure 3.12 shows the DRIFT spectrum for the pristine MCM-48 after calcination at 550 ^{o}C. The two absorption peaks at 1090 cm^{-1} and 802 cm^{-1} can be assigned to asymmetric and symmetric Si-O-Si stretching vibrations, respectively. The peak at 960 cm^{-1} is attributed to asymmetric vibration of Si-OH bonding and the peak at 466

cm^{-1} corresponds to Si-O-Si bending vibration. Also, it can be observed a peak at 1632 cm^{-1} due to H-O-H bending vibration. The broad peak at 3400 cm^{-1} is assigned to –OH stretching. Since the intensity of the peak at 3400 cm^{-1} is high even after drying the samples at 100 ^{o}C under high vacuum (for the removal of humidity or adsorbed water), we can assume that a significant number of silanol groups was retained on the surface and within the pore channel system of the pristine MCM-48 after the calcination for the removal of the template. The DRIFT spectrum of the pristine template-free MCM-48 has no peaks in the bending and stretching region of hydrocarbons (1350-1480 cm^{-1} and 2850-3000 cm^{-1}, respectively), both associated with the surfactants. Thus, the binary surfactant system was successfully removed during the calcination.

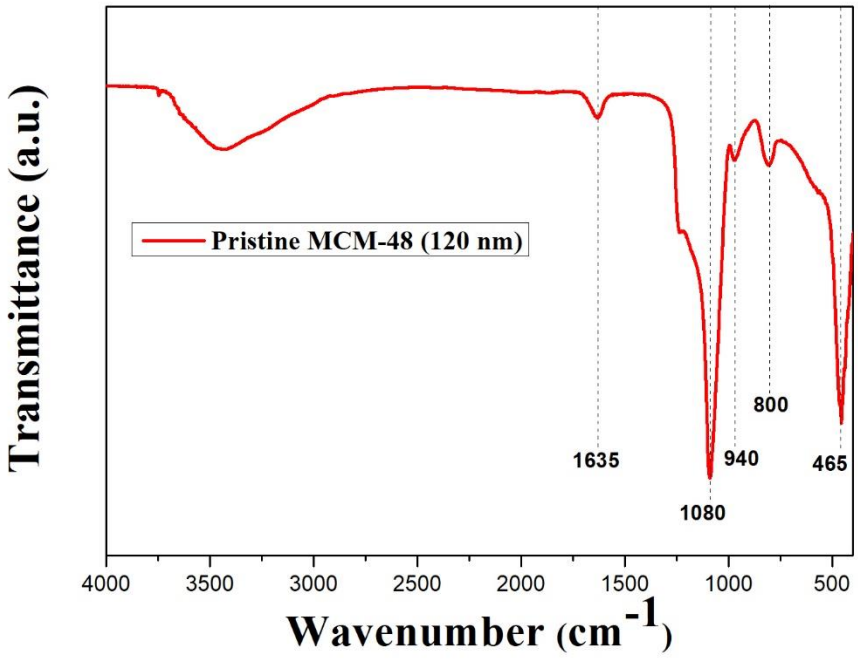

Figure 3.12. DRIFT spectrum for pristine MCM-48 mesoporous silica nanoparticles with average size of 120 nm.

Table 3.2. Wavenumbers for sample: pristine MCM-48 mesoporous silica nanoparticles with average size of 120 nm.

Pristine MCM-48 (120 nm)	
Wavenumber (cm^{-1})	**Assignment**
466	Si-O-Si bending vibration
802	Si-O-Si symmetric stretching
960	Si-OH asymmetric vibration
1090	Si-O asymmetric vibration
1632	H-O-H bending vibration
3400	–OH stretching

3.3.2.5. Thermogravimetric analysis (TGA).

Finally, the successful removal of the binary system of surfactants and the thermal stability of the monodisperse MCM-48 were evaluated by TGA. **Figure 3.13** presents the TGA curve for the pristine (template-free) monodisperse MCM-48 after heating up to 800 ^{o}C under N_2 atmosphere. Only one major region of weight loss can be observed, below 120 ^{o}C. There is approximately 2% weight loss below this temperature which is attributed to thermodesorption of physically adsorbed water.[25] No further weight loss was observed up to 800 ^{o}C which is an indication of the high thermal stability of the monodispersed NPs and, as previously discussed, the complete removal of the binary surfactant system during the calcination process.

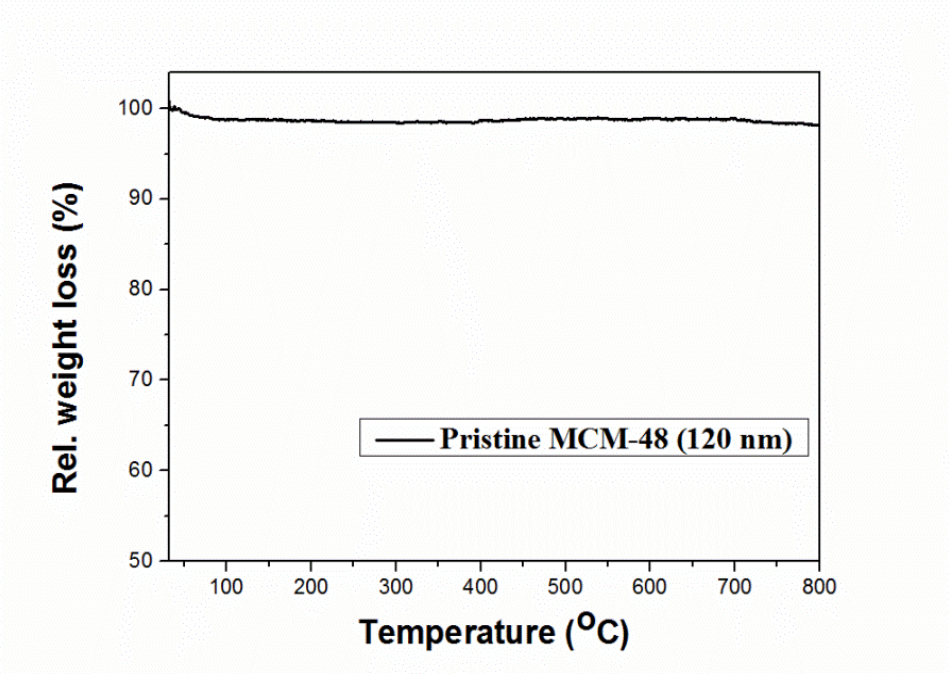

Figure 3.13. TGA curve for pristine MCM-48 mesoporous silica nanoparticles with average size of 120 nm.

Table 3.3. Comparison table of properties for MCM-48 with average size of 400 nm and 120 nm.

	MCM-48 (400 nm)	MCM-48 (120 nm)
XRD patterns	5 planes: (211), (220), (420), (332) and (431). Highly ordered mesoporous structure, *Ia3d* cubic space group.	5 planes: (211), (220), (420), (332) and (431). Highly ordered mesoporous structure, *Ia3d* cubic space group.
Nitrogen isotherms	type IV isotherms with no hysteresis loop	type IV isotherms with no hysteresis loop
S_{BET}	1180 to 1300 m^2/g	1050 to 1120 m^2/g
Average pore size	3.2 nm	3.5 nm
Total pore volume	0.8 cm^3/g	1.27 cm^3/g
Average size of particles	400 nm	120 nm
Morphology	mainly spherical monodispersed particles and some aggregated and fused together particles	only spherical monodispersed particles
Wall thickness (STEM/TEM)	not good enough resolution for the estimation	approximately 12 Å

References

[1] C. T. Kresge, M. E. Leonowicz, W. J. Roth, J. C. Vartuli, J. S. Beck, *Nature* **1992**, *359*, 710.

[2] J. S. Beck, J. C. Vartuli, W. J. Roth, M. E. Leonowicz, C. T. Kresge, K. D. Schmitt, C. T. W. Chu, D. H. Olson, E. W. Sheppard, S. B. McCullen, J. B. Higgins, J. L. Schlenker, *J. Am. Chem. Soc.* **1992**, *114*, 10834.

[3] T. Yanagisawa, T. Shimizu, K. Kuroda, C. Kato, *Bull. Chem. Soc. Jpn.* **1990**, *63*, 988.

[4] S. Inagaki, Y. Fukushima, K. Kuruda, *J. Chem. Soc. Chem. Commun.* **1993**, 680.

[5] Y. Wan, D. Zhao, *Chem. Rev.* **2007**, *107*, 2821.

[6] C.-Y. M. and H.-P. L. Si-Han Wu, *Chem. Soc. Rev.* **2013**, 3862.

[7] C. E. Fowler, D. Khushalani, B. Lebeau, S. Mann, *Adv. Mater.* **2001**, *13*, 649.

[8] Q. Cai, Z. S. Luo, W. Q. Pang, Y. W. Fan, X. H. Chen, F. Z. Cui, *Chem. Mater.* **2001**, *13*, 258.

[9] R. I. Nooney, D. Thirunavukkarasu, Y. Chen, R. Josephs, A. E. Ostafin, *Chem. Mater.* **2002**, 4721.

[10] C. Y. Lai, B. G. Trewyn, D. M. Jeftinija, K. Jeftinija, S. Xu, S. Jeftinija, V. S. Y. Lin, *J. Am. Chem. Soc.* **2003**, *125*, 4451.

[11] Z. Li, J. C. Barnes, A. Bosoy, J. F. Stoddart, J. I. Zink, *Chem. Soc. Rev.* **2012**, *41*, 2590.

[12] D. Borisova, H. Möhwald, D. G. Shchukin, *ACS Nano* **2011**, *5*, 1939.

[13] I. I. Slowing, J. L. Vivero-Escoto, B. G. Trewyn, V. S.-Y. Lin, *J. Mater. Chem.* **2010**, *20*, 7924.

[14] C. T. Kresge, W. J. Roth, *Chem. Soc. Rev.* **2013**, *42*, 3663.

[15] F. Hoffmann, M. Cornelius, J. Morell, M. Fröba, *Angew. Chemie - Int. Ed.* **2006**, *45*, 3216.

[16] F. Tang, L. Li, D. Chen, *Adv. Mater.* **2012**, *24*, 1504.

[17] L. A. Solovyov, *Chem. Soc. Rev.* **2013**, *42*, 3708.

[18] K. Schumacher, M. Grün, K. . Unger, *Microporous Mesoporous Mater.* **1999**, *27*, 201.

[19] K. Schumacher, P. I. Ravikovitch, A. Du Chesne, A. V Neimark, K. K. Unger, *Langmuir* **2000**, *16*, 4648.

[20] T.-W. Kim, P.-W. Chung, V. S.-Y. Lin, *Chem. Mater.* **2010**, *22*, 5093.

[21] H. I. Meléndez-Ortiz, Y. a. Perera-Mercado, L. a. García-Cerda, J. a. Mercado-Silva, G. Castruita, *Ceram. Int.* **2014**, *40*, 4155.

[22] K. S. Jean Rouquerol, Françoise Rouquerol , Philip Llewellyn, Guillaume Maurin, *Acad. Press* **2013**.

[23] S. Brunauer, L. S. Deming, W. E. Deming, E. Teller, *J. Am. Chem. Soc.* **1940**, *62*, 1723.

[24] A. Romero, M. D. Alba, W. Zhou, J. Klinowski, *J. Phys. Chem. B* **1997**, *101*,

5294.

[25] M. Kruk, M. Jaroniec, R. Ryoo, Sang Hoon Joo, *Chem. Mater.* **2000**, *12*, 1414.

[26] M. Kruk, M. Jaroniec, R. Ryoo, J. M. Kim, *Chem. Mater.* **1999**, 2568.

[27] E. W. S. J. C. Vartuli, K. D. Schmitt, C. T. Kresge, W. J. Roth, M. E. Leonowicz, S. B. McCullen, S. D. Hellring, J. S. Beck, J. L. Schlenker, D. H. Olson, *Chem. Mater.* **1994**, *6*, 2317.

[28] S. Brunauer, P. H. Emmett, E. Teller, *J. Am. Chem. Soc.* **1938**, *60*, 309.

[29] E. P. Barrett, L. G. Joyner, P. P. Halenda, *J. Am. Chem. Soc.* **1951**, *73*, 373.

[30] G. Horvath, K. Kawazoe, *J. Chem. Eng. Japan* **1983**, *16*, 470.

[31] M. W. Maddox, J. P. Olivier, K. E. Gubbins, *Langmuir* **1997**, *13*, 1737.

[32] P. I. Ravikovitch, D. Wei, W. T. Chueh, G. L. Haller, A. V. Neimark, *J. Phys. Chem. B* **1997**, *101*, 3671.

[33] P. I. Ravikovitch, S. C. O. Domhnaill, A. V. Neimark, F. Schueth, K. K. Unger, *Langmuir* **1995**, *11*, 4765.

[34] M. Kruk, M. Jaroniec, A. Sayari, *Langmuir* **1997**, *13*, 6267.

[35] C. Lastoskie, K. E. Gubbins, N. Quirke, *J. Phys. Chem.* **1993**, *97*, 4786.

[36] J. Landers, G. Y. Gor, A. V. Neimark, *Colloids Surfaces A Physicochem. Eng. Asp.* **2013**, *437*, 3.

[37] P. I. Ravikovitch, S. C. O. Domhnaill, A. V. Neimark, F. Schueth, K. K.

Unger, *Langmuir* **1995**, *11*, 4765.

[38] P. I. Ravikovitch, G. L. Haller, A. V. Neimark, *Mesoporous Mol. Sieves 1998, Proc. 1st Int. Symp.* **1998**, *117*, 77.

[39] A. V Neimark, P. I. Ravikovitch, M. Grün, F. Schüth, K. K. Unger, *J. Colloid Interface Sci.* **1998**, *207*, 159.

[40] R. K. Iler, *Wiley* **1979**, *New York*, 897.

[41] K. Cassiers, T. Linssen, M. Mathieu, M. Benjelloun, K. Schrijnemakers, P. Van Der Voort, P. Cool, E. F. Vansant, *Chem. Mater.* **2002**, *14*, 2317.

[42] Y. Xia, R. Mokaya, J. J. Titman, *J. Phys. Chem. B* **2004**, *108*, 11361.

Chapter 4:

Dual-Functionalised MSNs with Antibacterial Properties

4.1. Introduction

The definition of biofouling or biological fouling is the accumulation of microorganisms, plants, algae or animals on wetted surfaces. From the first minute of immersion of a clean surface in natural seawater, it immediately starts to adsorb a molecular conditioning film consisted of dissolved organic materials [1]. After that initial stage, the surface colonisation by a wide range of organisms depends on their relative rate of attachment and surface exploitation .[1,2] The distinction between the different fouling stages comprises "microfouling", "soft macrofouling" and "hard macrofouling". Biofouling has serious effects in various sectors of maritime industry. It is the main expense of maintenance for any immersed man-made surface such as buoys, membrane bioreactors and desalination units, power plants' cooling water systems and oil pipelines. Furthermore, it has significant effects on the aquaculture industry especially in marine finfish aquaculture where the use of sea cages is necessary.[3,4] As the diversity of fouling organisms is vast and the range of adhesion mechanisms correspondingly broad, it is a major challenge the creation of an effective fouling resistant coating.

The majority of the coatings in the past were biocide-based self-polishing coatings and their main component was the tributyltin (TBT), an efficient and versatile biocide.[5] However, due to their toxicity to humans and their negative impact on the environment, TBT compounds became completely banned after 1 January 2008 by the International Convention on the Control of Harmful Anti-fouling Systems on Ships of the International Maritime Organization.[6,7] Subsequently, antifouling manufacturers have been forced to urgently develop new and more environmentally

friendly antifouling paints. Almost all the antifouling paints today contain copper as their primary active ingredient which is well known for more than 2000 years from ancient years. Since 300 B.C., Greeks and Romans used copper in the bronze-shod rams of their warships and copper nails to secure the lead sheathing.[5,8]

To date, the working principle of the most of paint systems applied is based on slow release of biocide compounds. This operating principle has drawbacks for the paint systems [9]. Usually, the main active ingredient dissolves away and the paint loses its effectiveness but the binder stays behind.[5] Furthermore, as more coats are applied, the dead binder layers get thicker and thicker until they start to flake off in large chunks. Thus, it is very difficult and expensive to remove the old paint, and as a consequence, this type of coatings has been put aside. In addition, the antifouling release materials like perfluorinated or silane containing compounds were directly introduced into the coating thereby influencing other coating properties like corrosion protection. One approach to eliminate some of these drawbacks is the encapsulation, a methodology that has been applied into effective delivery systems for various applications in biotechnology, energy storage systems, protection against corrosion, pharmaceutics and food industry.[10–12] Commonly used technologies to encapsulate small molecules such as biocides include the Layer-by-Layer method and physical adsorption into porous materials.[13–15] By using proper carriers for encapsulation, it is possible to decrease and control the release rate of biocides and provide an effective protection from the surrounding environment.[16,17]

The quaternary ammonium salts (QASs) have been indexed as antimicrobial compounds for more than 70 years.[18,19] They have been used against the growth of

a broad range of microorganisms in several applications including food and pharmaceutical products, antiseptics, disinfectants, biocides, fungicides, cosmetics and water treatment.[20,21] In several studies, QAS were used to functionalise surfaces of different materials as antimicrobial treatment.[22–26] The advantage of the QAS-modified materials in comparison with the classic biocide-release coatings can be attributed to their attachable nature to the fillers of the coatings which allows a permanent antifouling effect of the coating without the release of the biocide material. An important parameter for the efficiency of the QAS is the alkyl chain length of their general molecular formula (NR_4^+). It has been found that QAS with alkyl chain length from C8 and higher present high antimicrobial activity.[27]

Herein, this chapter details on the development of functional fillers for antibacterial/antifouling coatings with advanced performance compared to the current state of the art coatings. Usually in the literature, while describing biomedical and antifouling systems, non-porous silica nanoparticles are used only for surface modifications and mesoporous silica nanoparticles (MSNs) only for encapsulation. However, to the best of our knowledge, this is the first study that describes the development of dual-function antibacterial/antifouling MSNs based on the combination of two strategies (surface modification and encapsulation) in one system (**Figure 4.1**). Through our approach, we are aiming to demonstrate the idea of an easy, simple and straightforward method for the development of dual-functional nanoparticles with long-lasting effect by using established and effective antibacterial/antifouling compounds. For this purpose, spherical MCM-48 MSNs with a dual synergetic antimicrobial effect were synthesised and tested against Gram-positive and Gram-negative bacteria. As mentioned in Chapter 3, spherical

MCM-48 MSNs with two different average sizes (400 nm and 120 nm) were synthesised in room temperature as carriers of antibacterial/antifouling compounds.[28–30] The interwoven, branched 3D mesostructure of MCM-48 makes it excellent candidate for the loading and release of active molecules with antibacterial/antifouling properties. Furthermore, the surface of this material can be easily functionalised with several compounds because of its high reactivity from the existence of hydroxyl groups bonded on its surface. Based on our search in the literature, this is the first study that reports on the surface modification of MCM-48 with QAS.

The surface of the nanoparticles (NPs) was modified with two different QASs, dimethyloctadecyl [3-(trimethoxysilyl) propyl] ammonium chloride (QC18) and dimethyltetradecyl [3-(triethoxysilyl) propyl] ammonium chloride (QC14). This modification provides the coatings the necessary hydrophobicity and antifouling properties, biocidal activity against marine microorganisms and resistance to microfouling in seawater immersion. Afterwards, the QAS-modified MSNs were loaded with a liquid biocide (Parmetol S15) for dual antifouling effect. The active ingredient for the Parmetol S15 is the 4, 5-dichloro-2-octyl-4-isothiazolin-3-one (DCOIT), a highly hydrophobic compound with good biodegradability and low water solubility. The DCOIT received the first Environmental Protection Agency (EPA) Green Chemistry award in 1996 for replacing the TBT in antifouling products and has been successfully used in encapsulation techniques for microcapsules with antifouling properties.[31] The final synthesised materials with the encapsulated biocide exhibit superior performance in the antibacterial tests due to the dual antimicrobial effect from the modified surface with QAS and from the encapsulated

biocide in the mesostructure of the NPs. Through our approach, we are aiming to prevent the early stages of the biofilm and biofouling formation where everything starts with the attachment of microorganisms on surfaces. Modified nanoparticles with high antibacterial performance are effective potential fillers for biofilm and fouling resistant coatings. The modified MSNs can provide permanent antibacterial properties to the coating formulations even after the release of the biocide due to the existence of the chemically attached QAS groups on the NPs surface.

Figure 4.1. Schematic illustration of the dual functionalisation process.

4.2. Experimental

4.2.1. Synthesis of dimethyltetradecyl [3-(trimethoxysilyl) propyl] ammonium chloride (QC14).

The dimethyltetradecyl [3-(triethoxysilyl) propyl] ammonium chloride (QC14) was synthesised by reacting 4.76 g N,N-dimethyltetradecylamine (1.97 x 10^{-2} moles) with 5 g 3-chloropropyltriethoxy silane (2.08 x 10^{-2} moles) in a 20 mL vial (**Figure 4.2**). The vial containing the reaction mixture was purged with nitrogen for 10 min before sealing. The quaternisation reaction was carried out at 110 ^{o}C for 48 h using magnetic stirring. After 48 h, the reaction mixture was cooled at room temperature before adding 9.76 g of methanol to produce 50 wt % solution of dimethyltetradecyl [3-(trimethoxysilyl) propyl] ammonium chloride (QC14) in methanol.[32]

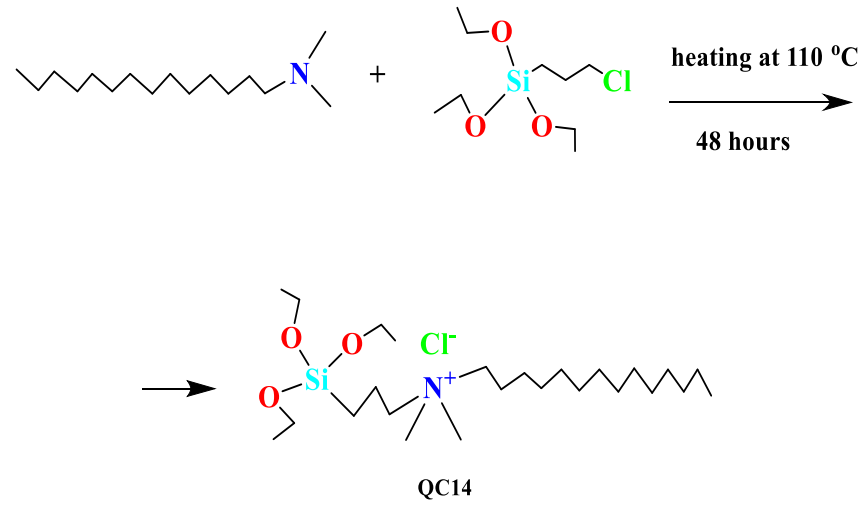

Figure 4.2. Reaction of synthesis for the dimethyltetradecyl[3-(triethoxysilyl)propyl] ammonium chloride (QC14).

4.2.2. Surface modification of the MCM-48.

The QAS-modified MCM-48 was prepared by hydrolysis and condensation reactions between the quaternary ammonium salt and the hydroxyl groups on the surface of the MCM-48 (**Figure 4.3**). For the surface modification, 1 g of calcinated MCM-48 powder was dispersed in a mixture of ethanol (50 mL) and deionised water (50 mL) using sonication bath. To the homogeneous solution, 0.5 mL of either QC18 or QC14 was added and stirred for 24 hours at room temperature. The modified NPs were collected with centrifugation, washed twice with ethanol and twice with water to remove the residual reagents and dried at ambient conditions.

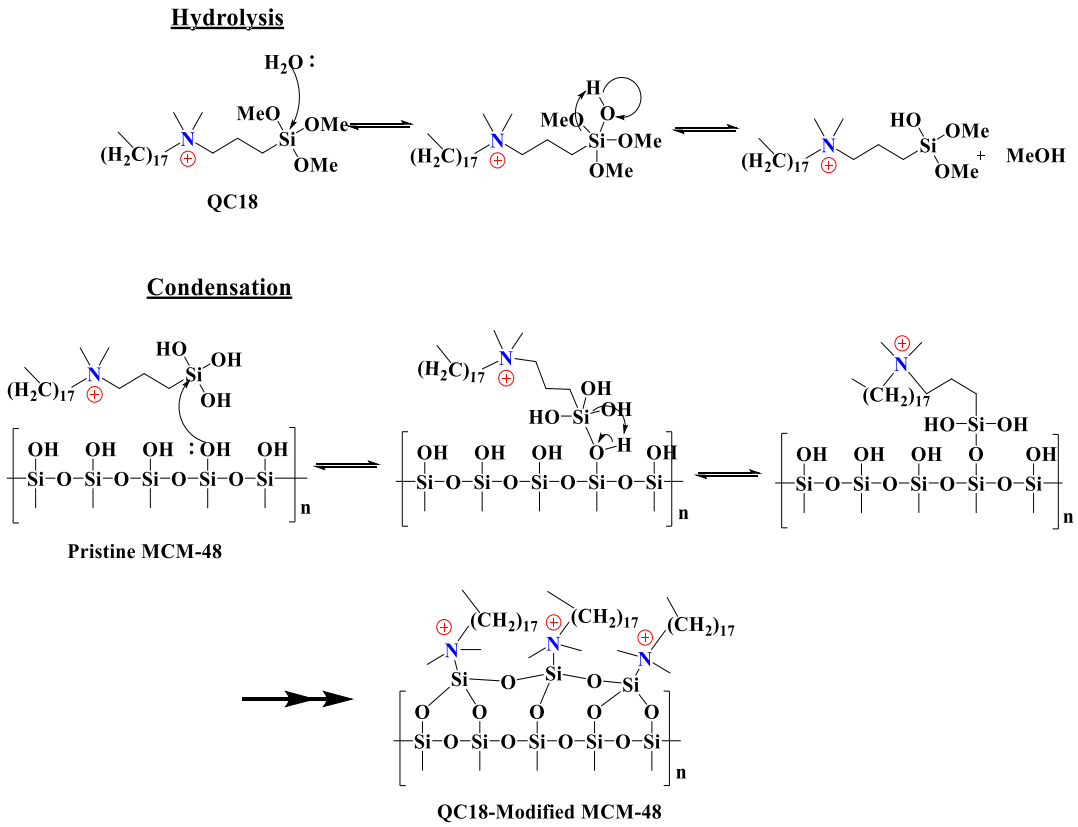

Figure 4.3. Mechanism of the surface modification reaction for the QAS-modified MCM-48.

4.2.3. Loading of the modified MCM-48 with biocide.

Before loading the modified MSNs, the samples were dried at 100 ^{o}C under vacuum in order to remove water and air from the mesoporous structure. Subsequently, modified MSNs (0.20 g) were dispersed directly in the biocide Parmetol S15 (20 mL) and stirred under vacuum overnight. The active ingredient for the Parmetol S15 is the 4, 5-dichloro-2-octyl-4-isothiazolin-3-one (DCOIT), a highly hydrophobic compound with good biodegradability and low water solubility (**Figure 4.4**). The solid was recovered by filtration and gently washed on the filter paper dropwise with ethanol. The loaded NPs were dried at ambient conditions.

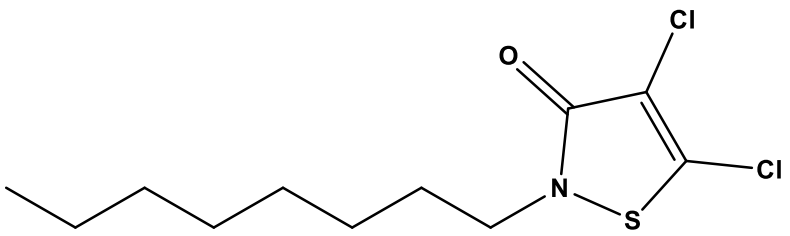

4,5-Dichloro-2-octyl-3-isothiazolone (DCOIT)

Figure 4.4. Chemical formula of the active ingredient for the Parmetol S15 (4, 5-dichloro-2-octyl-4-isothiazolin-3-one, DCOIT).

4.2.4. Minimum Inhibitory Concentration Determination (MIC).

S. aureus (ATCC 25923) and *E. coli* (ATCC 10536) were transferred from the stock to a fresh agar plate and incubated overnight at 37 ^{o}C. Three colonies were taken from the agar plate, transferred to fresh NB medium (Oxoid, Ltd-Thermo Fisher) and grown overnight in a shaking incubator (200 rpm, at 37 ^{o}C). The bacterial cell concentration was adjusted to $2x10^{5}$ colony forming units per millilitre (CFU/mL) in

sterile NB for each of the bacterial strains. Then 100 μL of the bacterial solution were added to each of the well of a 96-well plate containing different concentrations of modified nanoparticle solutions. The samples used for the MIC determination were: pristine MCM-48, QC18-modified MCM-48 loaded with Parmetol S15 (QC18/Parm/MCM-48), QC14-modified MCM-48 loaded with Parmetol S15 (QC14/Parm/MCM-48), QC18-modified MCM-48 (QC18/MCM-48) and QC14-modified MCM-48 (QC14/MCM-48). Afterwards, the plates were placed in a FilterMax F5 Multimode Plate Reader (Molecular Devices) and screened for 24h at 37 ^{o}C. The minimum inhibitory concentration (MIC) was calculated as the minimum concentration which resulted in maintenance or reduction of the initial inoculum.

4.2.5. Antibacterial activity of pristine and modified MCM-48.

S. aureus (ATCC 25923) and *E. coli* (ATCC 10536) cultures were grown overnight at 37 ^{o}C in sterilised nutrient broth medium (NB). The bacterial cells were centrifuged and the NB was replaced by a sterile 500 fold diluted NB (1/500 NB). For the tests against Gram-negative *E. coli* and Gram-positive *S. aureus*, 22 mm x 22 mm glass slides were coated by 1 mL of either pristine or modified nanoparticles dispersed in ethanol solution (2 wt %) with a spin coater. The samples used for the antibacterial tests were: pristine MCM-48, QC18-modified MCM-48 and loaded with Parmetol S15 (QC18/Parm/MCM-48), QC14-modified MCM-48 and loaded with Parmetol S15 (QC14/Parm/MCM-48), QC18-modified MCM-48 (QC18/MCM-48) and QC14-modified MCM-48 (QC14/MCM-48). The pristine MCM-48 was used as negative control since no antibacterial activity is expected from these

materials. The spin-coated glass slides were UV sterilised for 1 hour and were inoculated with 50 μL of 10^5 colony forming unit per mL (CFU/mL) of either *S. Aureus* or *E. Coli* solution. Each sample was covered with a 20 mm x 20 mm sterile glass cover slip and was incubated at 37 ^oC for 3 hours. Then, each sample was introduced in a 50 mL falcon tube containing 10 mL of phosphate-buffered saline solution (PBS) and was vortexed prior to spreading 100 μL of the bacterial solution on an agar plate. Inoculated agar plates were incubated overnight and the CFU/mL was counted. Each sample type was studied in triplicate following this method. One-way analysis of variance (ANOVA) was used to compare mean values in order to determine the equivalence of variance between the samples. Significance between the samples was determined using the Bonferroni multiple comparison test where a value of $p < 0.05$ was taken as statistically significant.

4.2. Results and discussion

4.2.1. Dual functionalised MCM-48 with average size of 400 nm.

4.2.1.1. Surface modification with QAS.

After the successful synthesis and characterisation of spherical MCM-48 MSNs with average size of 400 nm (Chapter 3), the surface of these materials was modified with two different QASs, QC18 and QC14 (**Figure 4.5** and **Figure 4.6**). Two types of samples were synthesised: MCM-48 with average size of 400 nm modified with

QC18 (QC18/MCM-48@400) and MCM-48 with average size of 400 nm modified with QC14 (QC14/MCM48@400). In order to confirm the successful surface modification, the samples were characterised by DRIFT, ζ-potential, TGA and elemental analysis measurements.

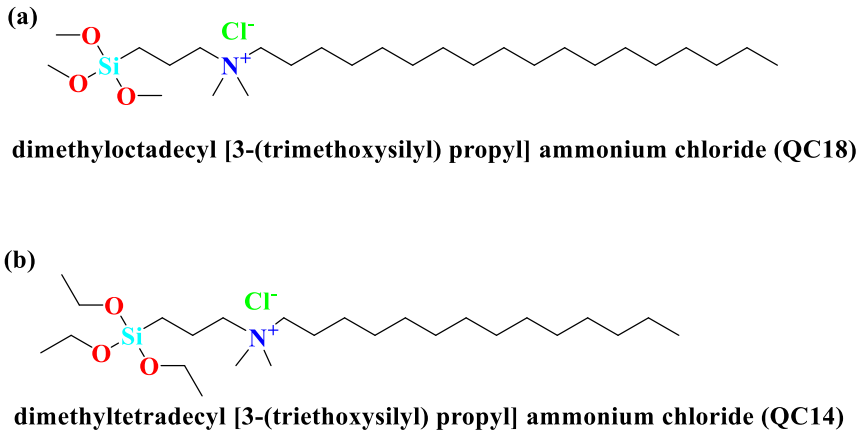

Figure 4.5. Chemical structure of (a) QC18 and (b) QC14.

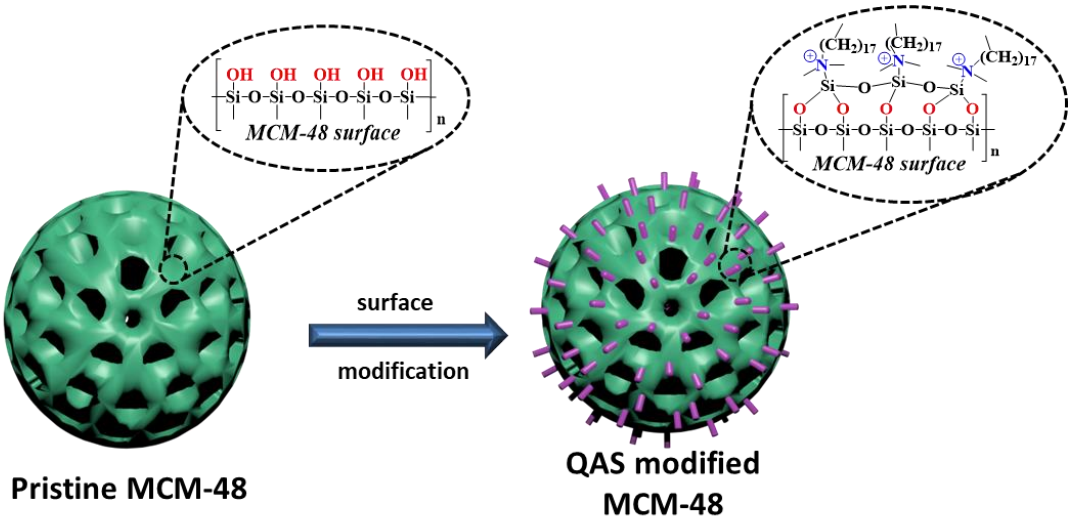

Figure 4.6. QAS-modified MCM-48 showing the covalently attached QAS molecules on the surface of MCM-48.

The DRIFT spectra for the pristine MCM-48@400, QC18/MCM-48@400 and QC14/MCM-48@400 are shown in **Figure 4.7**. All samples present the characteristic absorption peaks for the SiO_2 materials: Si–O–Si bending vibration (465 cm^{-1}), Si–O–Si symmetric stretching (800 cm^{-1}), Si–OH asymmetric vibration (940 cm^{-1}), Si–O asymmetric vibration (1080 cm^{-1}), H–O–H bending vibration (1635 cm^{-1}) and –OH stretching (3400 cm^{-1}). However, the QAS-modified samples showed three additional peaks. These peaks represent the alkyl chain of the QASs and prove that the silica nanoparticles were successfully decorated by QASs. The peak at 1465 cm^{-1} corresponds to the C−H bending vibration and the peaks at 2850 and 2950 cm^{-1} correspond to the C−H stretching. Furthermore, the broad −OH peak at 3400 cm^{-1} for the pristine MCM-48@400 is more intense compared to the QAS-modified MCM-48@400 because of the free −OH groups on the surface and within the pore channel system of pristine MCM-48@400. There is also a significant reduction in the

intensity of the O-H peak in the QAS-modified MCM-48 spectra. As shown in **Figure 4.3** and **Figure 4.6** for the reactions taking place during the surface modification, the $-Si(OCH_3)_3$ groups of the QASs can be covalently bonded with the free −OH groups on the surface of the pristine MCM-48. Therefore, the −OH bending vibration (1635 cm^{-1}) and −OH stretching (3400 cm^{-1}) for the QAS-modified MCM-48 will give very low signal as most of the available hydroxyl groups reacted with the QASs.

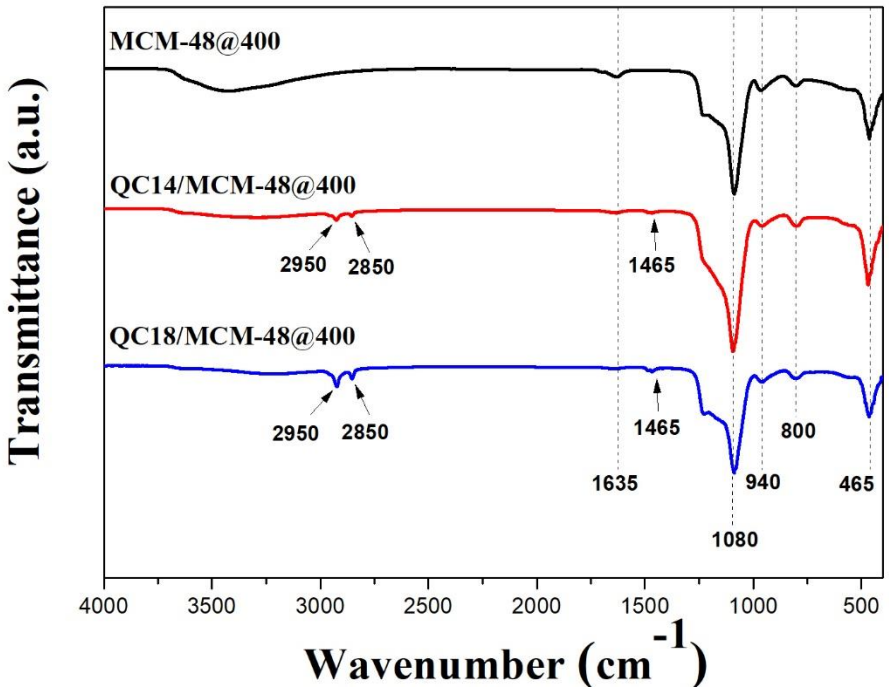

Figure 4.7. DRIFT spectra for pristine MCM-48@400, QC18/MCM-48@400 and QC14/MCM-48@400.

Table 4.1. Wavenumbers for samples: pristine MCM-48@400, QC18/MCM-48@400 and QC14/MCM-48@400.

Wavenumber (cm^{-1})	Assignment
465	Si-O-Si bending vibration
800	Si-O-Si symmetric stretching
940	Si-OH asymmetric vibration
1080	Si-O asymmetric vibration
1465	C−H bending vibration
1635	H-O-H bending vibration
2850	C−H stretching
2950	C−H stretching
3400	–OH stretching

Further information about the surface properties of the modified and unmodified materials was obtained via ζ-potential measurements (**Table 4.2**). The ζ-potential is an electrokinetic potential parameter in colloidal dispersions indirectly determined by the surface charge of particles when suspended in polar media.[33] Through the manipulation of ζ-potential, we can get information regarding the stability of colloidal dispersions. Colloids with high absolute number of ζ-potential are electrically stabilised while colloids with low values of ζ-potential tend to form aggregates. ζ-potential values from ±30 to ±40 mV indicate moderate stability while values from ±40 to ±60 mV indicate good stability. The surface of the pristine MSN is positively charged at pH below its isoelectric point (IEP=pH 2.0) and negatively charged above the IEP.[34]. Therefore, the ζ-potential for the pristine MCM-48 at pH 1.5 is slightly positive at 3 mV. In the pH range from 4 to 9.5, the ζ-potential for the pristine MCM-48 was shifted to negative values between -28 and -34 mV due to the existence of the negatively charged hydroxyl groups on the surface of MCM-48.

This behaviour implies that the pristine NPs have moderate stability in this pH range. On the other hand, at the pH range from 1.5 to 9.5, the ζ-potential for the QAS modified nanoparticles was shifted significantly to positive values due to the presence of the positively charged quaternary ammonium groups on the surface of the materials instead of the negatively charged hydroxyl groups. Taking into consideration the high values of ζ-potential for the QAS modified materials (between +30 mV and +60 mV), we can hypothesise that the modified nanoparticles have good stability in colloidal dispersions. In addition, the shift of ζ-potential to high positive values implies that the QASs were successfully grafted on the surface of MCM-48.

Table 4.2. ζ-potential measurements for the pristine MCM-48@400, QC18/MCM-48@400 and QC14/MCM-48@400.

pH value	Pristine MCM-48 @400 (mV)	QC18/MCM-48 @400 (mV)	QC14/MCM-48 @400 (mV)
1.5	3.0 ±1	32.5 ±2	30.1 ±1
4	-31.0 ±2	63.3 ±2	49.2 ±1
7.5	-28.3 ±1	52.8 ±1	43.0 ±2
9.5	-33.9 ±1	50.1 ±1	35.8 ±1

Further confirmation of the successful surface modification comes from the elemental analysis. The QC18/MCM-48@400 and QC14/MCM-48@400 showed significant increment of % C, % H and % N compared to the pristine MCM-48@400. This result can be explained from the presence of the alkyl functional groups and the positively charged nitrogen groups of the covalently attached QAS moieties on the surface of the pristine nanoparticles (**Table 4.3**).

Table 4.3. Elemental analysis for the pristine MCM-48@400, QC18/MCM-48@400 and QC14/MCM-48@400.

Sample	Elemental analysis (wt. %)		
	C	H	N
Pristine MCM-48@400	1.08	0.53	0
QC18/MCM-48@400	20.24	3.95	1.00
QC14/MCM-48@400	12.80	2.63	0.73

The thermogravimetric analysis (TGA) was used to evaluate the amount of QAS grafted on the surface of the MSNs when heated under N_2 atmosphere up to 800 ^oC (**Figure 4.8**). The pristine MCM-48 was calcinated up to 800 ^oC and its weight decreased only by 4% mainly because of thermodesorption of physically adsorbed water inside the pristine material.[35] The silica NPs have very high thermal stability and almost keep their weight constant up to 800 ^oC at least. However, when QC18/MCM-48@400 and QC14/MCM-48@400 nanoparticles were calcinated to 800 ^oC, they lost 28.3% and 19.2% of their initial weight, respectively. Both QC18- and QC14-modified MCM-48 presented 3% weight loss between 30 ^oC and 130 ^oC because of thermodesorption of physically adsorbed water inside the pore channel system of the materials. The further 25.3% or 16.2% weight loss between 200 ^oC and 800 ^oC is attributed to the calcination of the grafted QC18 or QC14 groups, respectively.

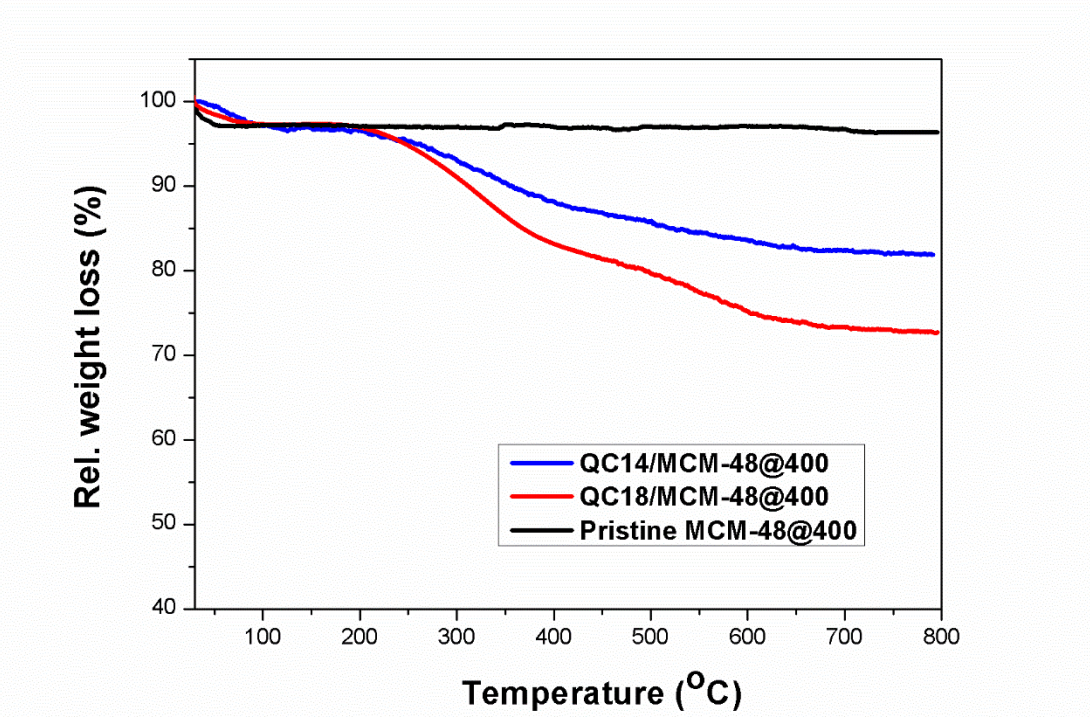

Figure 4.8. TGA curves for the pristine MCM-48@400, QC18/MCM-48@400 and QC14/MCM-48@400.

Significant differences between the two types of modified materials (QC18 and QC14 modification) at the TGA, ζ-potential measurements and elemental analysis are caused by two main reasons. Firstly, there are four extra $–CH_2$ groups in the alkyl chain of the QC18 molecule compared to the QC14 molecule (**Figure 4.5**). Therefore, we expected higher weight loss and higher % of C and H for the QC18/MCM-48@400 at the TGA measurements and elemental analysis. Secondly, the QC18 compound was commercially available at 99% purity while the QC14 compound is commercially unavailable and as a result was synthesised in-house. The dimethyltetradecyl [3-(triethoxysilyl) propyl] ammonium chloride (QC14) was synthesised by reacting 1.97 x 10^{-2} moles of N, N-dimethyltetradecylamine with 2.08

x 10^{-2} moles of 3-chloropropyltriethoxy silane at 110 ^{o}C for 48 h (**Figure 4.2**). After the reaction, the colour of the solution became yellow-brown and the viscosity increased confirming the quaternisation reaction (**Figure 4.9**).

Figure 4.9. QC14 synthesis: solution before (left) and after (right) the reaction.

^{1}H-NMR spectroscopy was used in order to confirm the successful synthesis of the QC14 (**Figure 4.10**). The ^{1}H-NMR spectrum of the product (QC14) showed two additional peaks at 3.38 ppm [$(-N^{+}-(CH_3)_2]$ and 3.46 ppm ($-N^{+}-CH_2$) because of the quaternization. However, the presence of the peaks at 3.54 ppm ($-CH_2-Cl$) and 2.2 ppm [$-N-(CH_3)_2$] after 48 hours of reaction indicate that there were residual N,N-dimethyltetradecylamine and 3-chloropropyltriethoxy silane. Thus, during the surface modification of the MCM-48 with QC14, the available hydroxyl groups on the MCM-48 surface can react both with the 3-chloropropyltriethoxy silane and the QC14. As a result, the surface of the QC14/MCM-48@400 was covered with QC14 molecules and 3-chloropropyltriethoxy silane molecules. Our hypothesis is in agreement and supported by the decreased amount of nitrogen in elemental analysis

and the decreased positive values in ζ-potential measurements for the QC14 functionalised silica compared to the QC18 functionalized silica since part of the QC14/MCM-48@400 surface is covered by 3-chloropropyltriethoxy silane (absence of positively charged nitrogen and lower molecular weight compared to QC14). Furthermore, the lower weight loss on the TGA curve for the QC14 functionalised silica compared to the QC18 functionalized silica can be attributed to the lower molecular weight of the QC14 and 3-chloropropyltriethoxy silane molecules grafted on the surface of QC14/MCM-48@400.

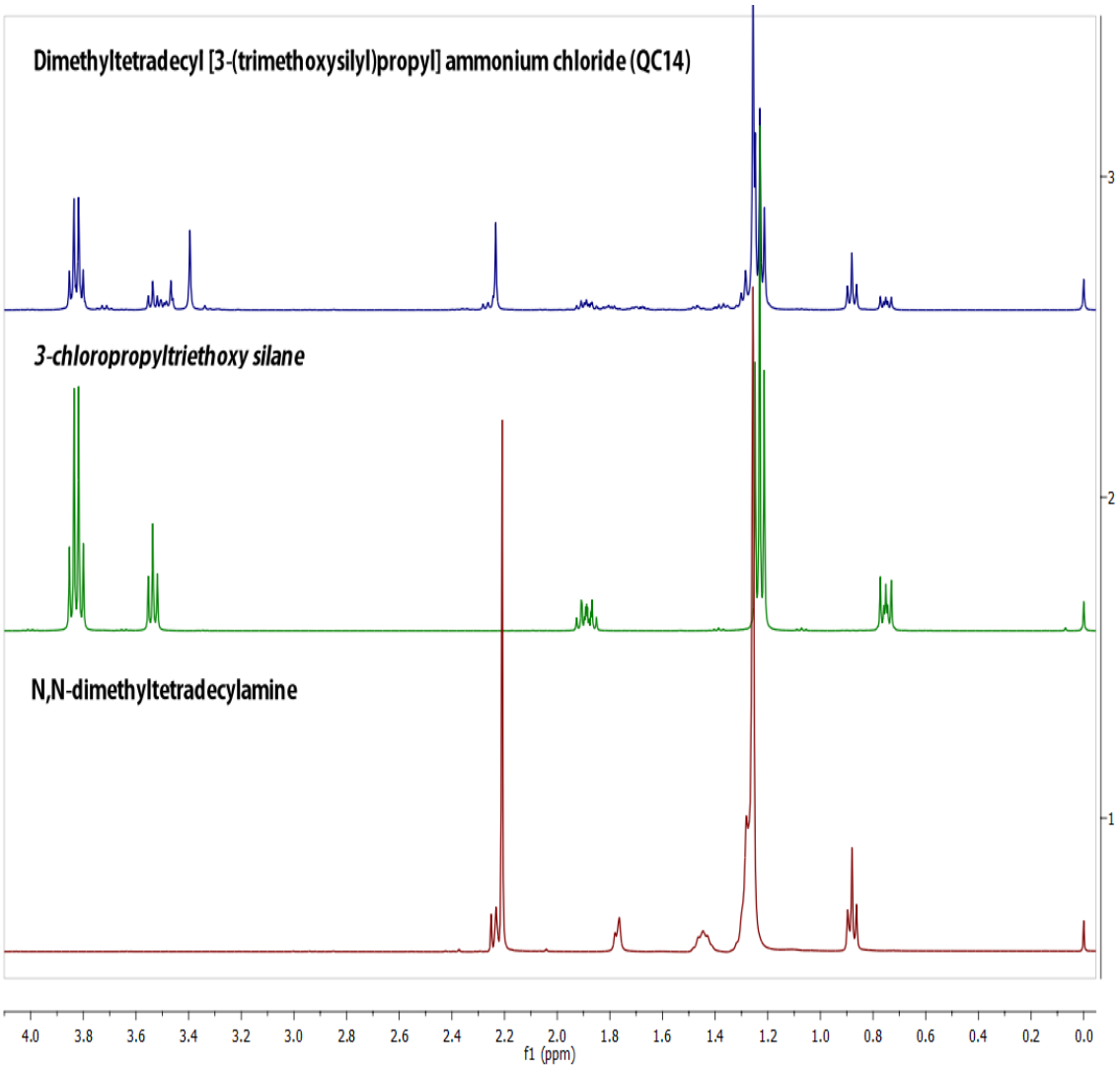

Figure 4.10. ^{1}H-NMR spectra of dimethyltetradecyl[3-(triethoxysilyl)propyl] ammonium chloride (QC14, product), 3-chloropropyltriethoxy silane (reactant) and N,N-dimethyltetradecylamine (reactant).

4.2.1.2. Encapsulation of biocide.

Encapsulation is an important technology that finds applications in pharmaceutical industry, food industry, energy storage systems, etc. by using materials such as mesoporous silica nanoparticles, polymeric capsules, hydrogels, etc. as hosts.[36,37] In our approach for the encapsulation of Parmetol S15 biocide, the two different types

of modified MCM-48 were dispersed directly *via* sonication in the commercially available liquid biocide Parmetol S15 and left under vacuum overnight. After the recovery of the light yellow solid materials with the encapsulated biocide (**Figure 4.11**), the samples were tested with the TGA and the amount of the loaded biocide was measured.

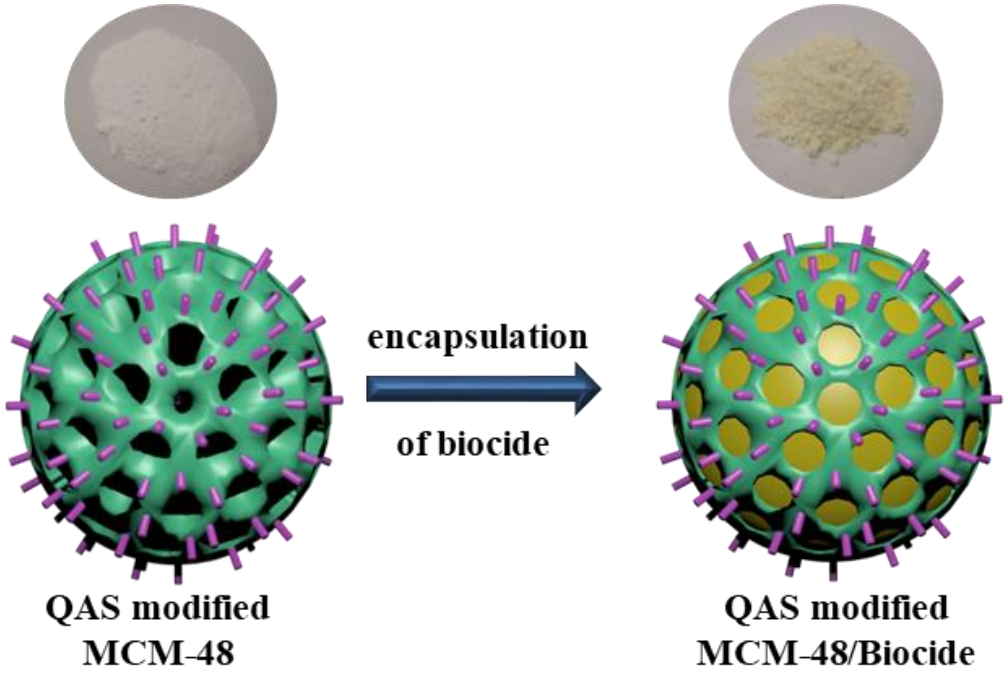

Figure 4.11. Encapsulation of biocide in the QAS-modified MCM-48 and solid materials before and after the encapsulation.

The TGA curves of the QAS-modified MCM-48 loaded with the Parmetol S15 were compared with the TGA curves of the unloaded QAS-modified MCM-48 (**Figure 4.12**). The loaded QC18-modified MCM-48 with Parmetol (QC18/Parm/MCM-48@400) showed 26.9 wt % additional weight loss in comparison with the unloaded

QC18/MCM-48@400 due to the encapsulated biocide. The loaded QC14-modified MCM-48 with Parmetol (QC14/Parm/MCM-48@400) exhibited 31.5 wt % further weight loss in comparison with the unloaded QC14/MCM-48@400, which is also attributed to encapsulated biocide. The TGA curves confirmed the successful encapsulation of the biocide inside the MSNs. During the surface modification, the –$Si(OCH_3)_3$ groups of the quaternary silane are covalently bonded with –OH groups close to the opening of the pores thus blocking some of the pores for biocide ingress. Moreover, in the case of the QC18 modified MSNs, the blockage of the pores is higher due to its larger molecular size. This can explain the 4.6 wt % lower amount of encapsulated biocide inside the QC18/Parm/MCM-48@400 compared to the amount encapsulated inside the QC14/Parm/MCM-48@400.

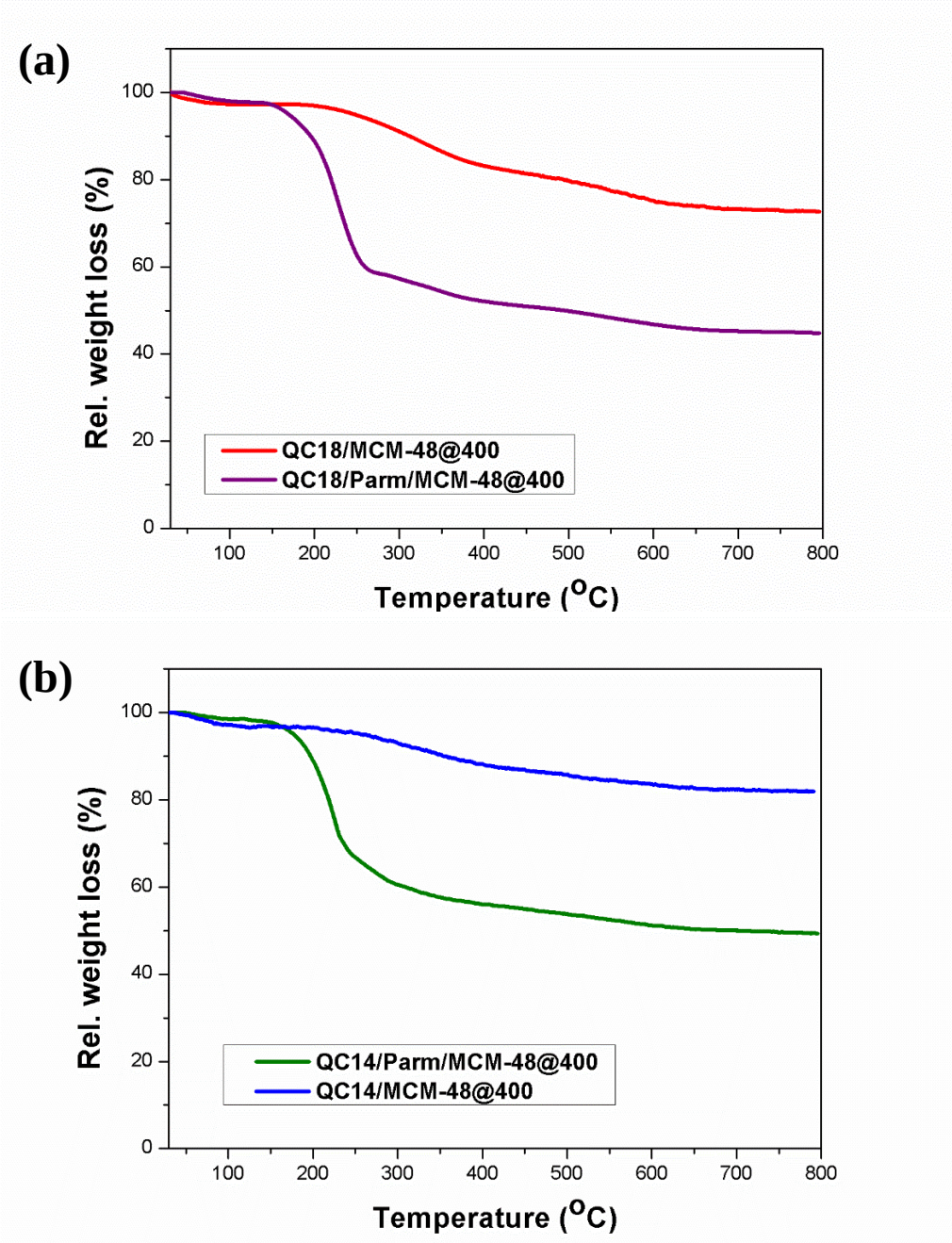

Figure 4.12. TGA curves for (a) the loaded/unloaded QC18-modified MCM-48 and (b) the loaded/unloaded QC14-modified MCM-48.

4.2.1.3. Determination of MIC.

In our first attempts to evince the antibacterial activity of the synthesised NPs, we used a protocol for the determination of the minimum inhibitory concentration (MIC) for the modified materials against Gram-positive *S. aureus* and Gram-negative *E. coli* bacteria. The samples we used for the MIC protocol were: QC18/Parm/MCM-48@400, QC14/Parm/MCM-48@400, QC18/MCM-48@400 and QC14/MCM-48@400. The initial highest concentration of modified NPs used for the protocol was adjusted to 1 mg/ml because above this concentration a significant amount of NPs were precipitating during the 24 hours screening. The MIC was calculated as the minimum concentration which resulted in maintenance or reduction of the initial inoculum of bacteria.

As can been seen from the **Table 4.4**, the dual functionalised NPs QC18/Parm/MCM-48@400 and QC14/Parm/MCM-48@400 presented significantly low values of MIC against Gram-positive (3.91 mg/L and 1.95 mg/L, respectively) and Gram-negative bacteria (31.25 mg/L both materials) while the single functionalised QC18/MCM-48@400 and QC14/MCM-48@400 showed no inhibition of bacteria growth for the used concentration of 1 mg/ml. Possible explanation of that result could be the lower number of active groups on the surface of the single functionalised QC18/MCM-48@400 and QC14/MCM-48@400 while the dual functionalised QC18/Parm/MCM-48@400 and QC14/Parm/MCM-48@400 with the encapsulated biocide are more effective due to the release of the biocide which means much more active groups against the bacteria.

Furthermore, the covalently attached QASs on the surface of the single functionalised NPs are more likely to show their antibacterial effectiveness when they are in direct contact with the bacteria cell membrane which is not favourable according to this protocol since the NPs are dispersed in solution. For that reason, a more representative assessment of the antibacterial properties of the synthesised materials was essential with a protocol that could provide reliable results from the direct contact of exposed bacteria on the QAS-modified surfaces of the NPs (more information in the following section).

Table 4.4. Determination of MIC values for the QC18/Parm/MCM-48@400, QC14/Parm/MCM-48@400, QC18/MCM-48@400 and QC14/MCM-48@400.

Sample Number	MIC *S. aureus* (mg/L)	MIC *E. coli* (mg/L)
QC18/Parm/MCM-48@400	3.91	31.25
QC14/Parm/MCM-48@400	1.95	31.25
QC18/MCM-48@400	> 1 mg/mL	> 1 mg/mL
QC14/MCM-48@400	> 1 mg/mL	> 1 mg/mL

4.2.1.4. Antibacterial performance.

In order to evaluate the antibacterial performance of a compound or a surface, there are either qualitative or quantitative tests. The qualitative tests (such as bacterial imaging experiments and fluorescence microscopic observations) are providing only a rough idea of the presence or absence of substances with anti-microbial activity since the images are focusing only on a specific area of the exposed sample. On the other hand, quantitative methods have higher impact and provide more reliable

results since they rely on the counting of all the viable bacteria after exposure for certain time to the potential anti-microbial compound or surface. In the antibacterial assays for our samples, we used a quantitative method and we counted the number of viable bacteria (according to the colony-forming unit, CFU) at the end of the experiment.

Furthermore, the antibacterial assays are chosen according to type of the exposed material. In our case, we wanted to evaluate the anti-microbial activity of mesoporous silica nanoparticles which is very challenging due to the porosity of the materials. These porous materials can easily absorb small chemical compounds such as dyes which are used in the bacterial imaging experiments and the fluorescence microscopic observations. In fact, we tried to use two types of imaging techniques but without success due to the porosity of the exposed materials. At the beginning, we thought that it was good idea to apply a protocol that uses the crystal violet dye in order to visualise the adhered alive bacteria (the crystal violet dye attach and stain only the alive bacteria). Unfortunately, this protocol was not applicable for the materials we synthesised and the visualisation of differences between the treated-untreated samples was not possible since all of them presented a deep purple colour due to the absorbed dye onto the exposed mesoporous nanoparticles (either pristine or modified). In addition, we applied a protocol that uses two fluorescent dyes for monitoring the viability of bacterial populations (LIVE/DEAD™ BacLight™ Bacterial Viability Kit); red colour for dead bacteria and green colour for alive bacteria. Unfortunately, we experienced similar problems with the crystal violet protocol and both fluorescent dyes were absorbed into the exposed mesoporous materials.

According to the protocol we used for the evaluation of the antibacterial activity of synthesised materials, 22mm x 22mm glass slides were coated with a spin coater by using 1 mL of nanoparticles dispersed in ethanol solution (2 wt %) and tested against Gram-negative *E. Coli* and Gram-positive *S. aureus* (**Figure 4.13**). The pristine MCM-48@400 was used as a negative control since no antibacterial activity is expected from this material. The relative number of viable bacteria adhered on the glass slide coated with pristine MCM-48@400 was defined as 100%.

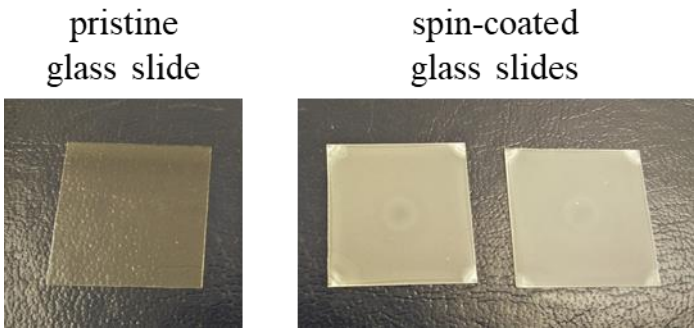

Figure 4.13. Glass slides used for the antibacterial tests. Pristine glass slide (left) and spin-coated glass slides covered with modified NPs.

As can been seen from **Figure 4.14** and **Figure 4.15**, the QC18 and QC14 modified MCM-48 reduced the number of the viable bacteria *E. Coli* by 89% and 77% respectively compared to the pristine MCM-48 while the two types of modified MSNs with the encapsulated Parmetol S15 presented excellent and enhanced antibacterial performance by killing all the exposed bacteria during the test resulting in 100% reduction compared to the pristine MCM-48.

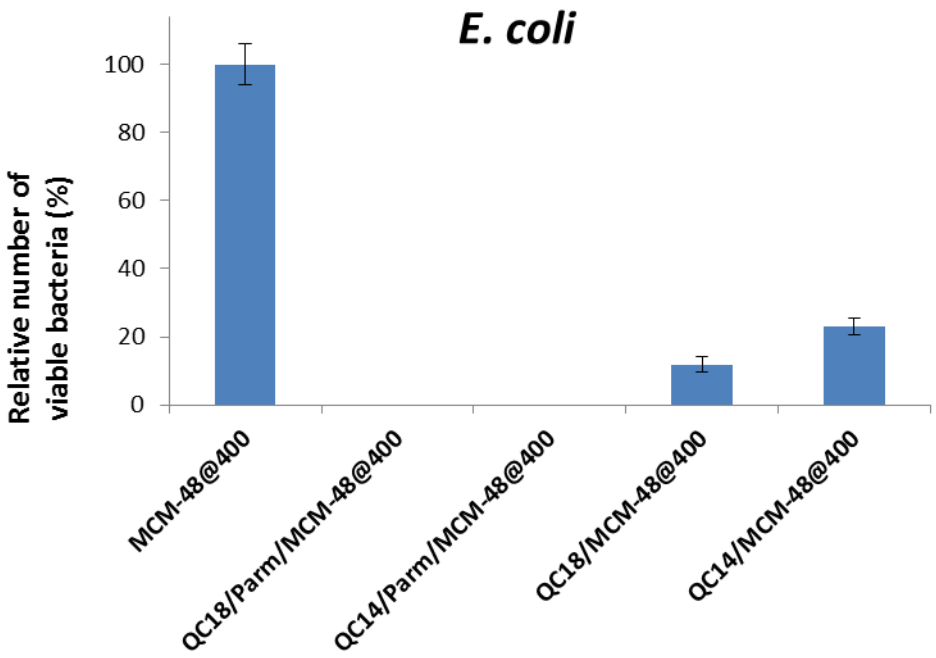

Figure 4.14. Relative number of viable bacteria (*E. coli*) after testing on glass slides spin-coated with pristine MCM-48@400, loaded/unloaded QC18 and QC14 modified MCM-48@400. Statistically significant differences between the samples ($p < 0.0005$).

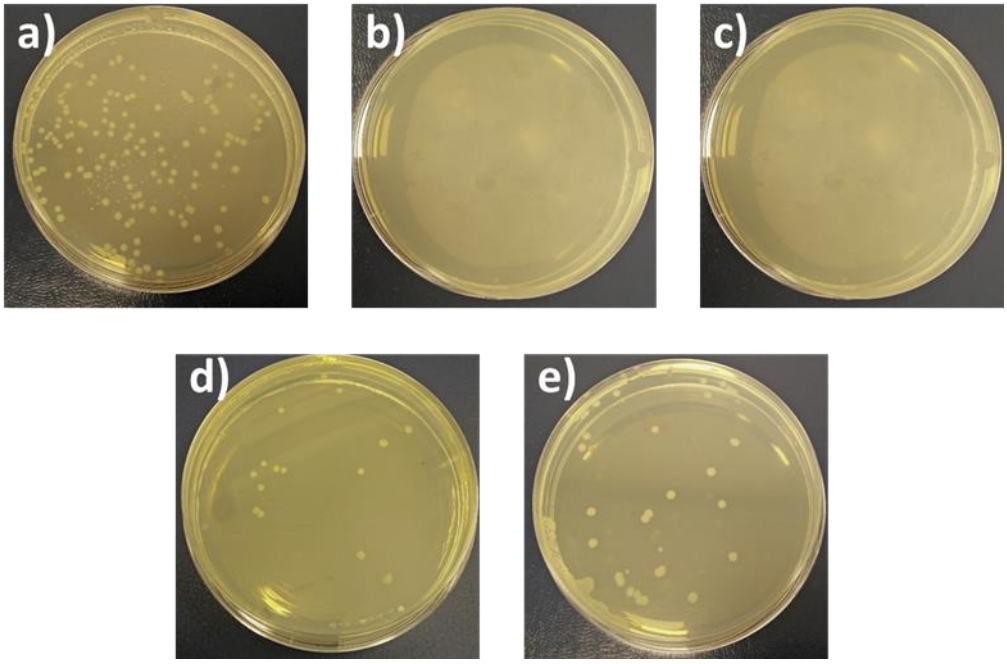

Figure 4.15. Representative photographs of *E. coli* colonies grown on agar plates after overnight incubation, exposed on glass slides coated with a) pristine MCM-48@400, b) QC18/Parm/MCM-48@400 and QC14/Parm/MCM-48@400, c) QC18/MCM-48@400 and d) QC14/MCM-48@400.

Figure 4.16 and **Figure 4.17** show the antibacterial performance of the pristine and modified MCM-48 against the Gram-positive bacteria *S. aureus*. The QC18 and QC14 modified MCM-48 reduced the relative number of viable bacteria by 94% and 78% respectively. The QC18 and QC14 modified MCM-48 and loaded with the additional biocide Parmetol S15 exhibited 100% reduction by killing all the exposed bacteria at the end of the experiment. In the antibacterial tests against both types of bacteria, there is a statistically significant ($p < 0.0005$) increase in antibacterial activity when the pristine MCM-48 are either modified only with QAS or modified with QAS and loaded with Parmetol S15.

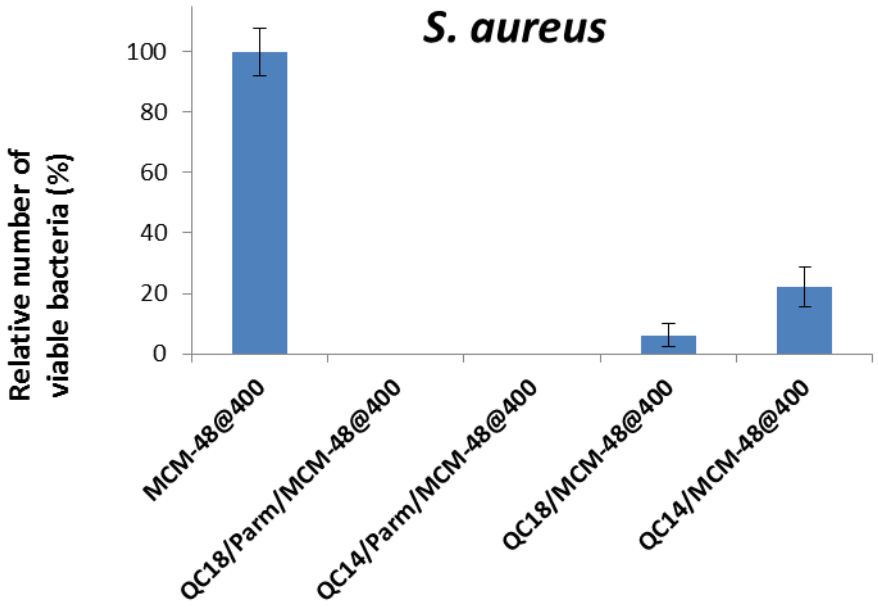

Figure 4.16. Relative number of viable bacteria (*S. aureus*) after testing on glass slides spin-coated with pristine MCM-48@400, loaded/unloaded QC18 and QC14 modified MCM-48@400. Statistically significant differences between the samples ($p < 0.0005$).

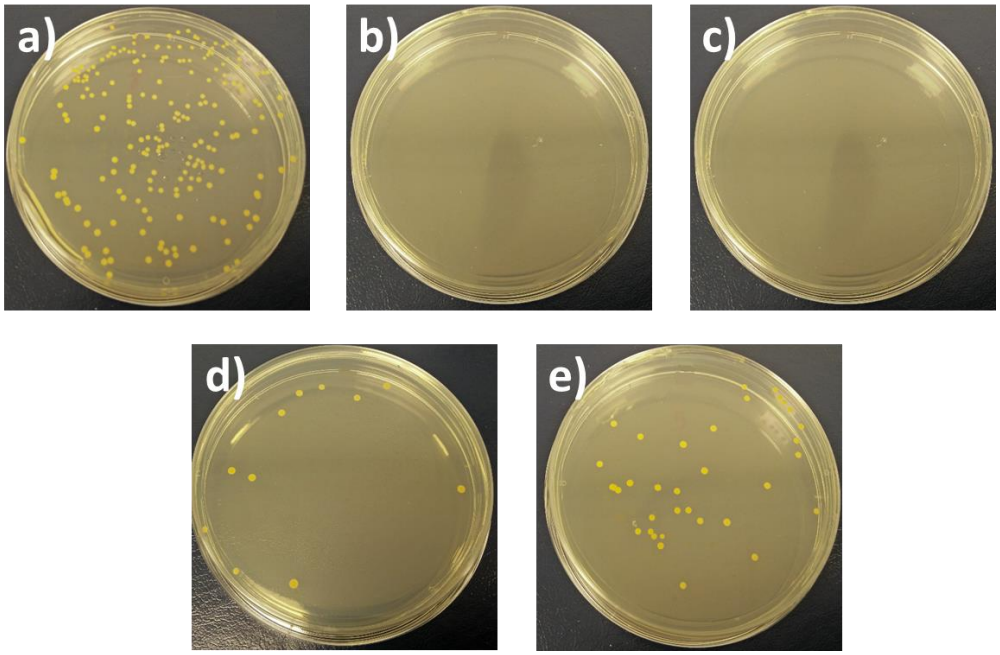

Figure 4.17. Representative photographs of *S. aureus* colonies grown on agar plates after overnight incubation, exposed on glass slides coated with a) pristine MCM-48@400, b) QC18/Parm/MCM-48@400, c) C14/Parm/MCM-48@400, d) QC18/MCM-48@400 and e) QC14/MCM-48@400.

It is noteworthy that the QC18/MCM-48@400 presented higher antibacterial performance against *E. coli* and *S. aureus* in comparison with the QC14/MCM-48@400. As mentioned previously, the surface of the QC14/MCM-48@400 is covered with QC14 molecules and 3-chloropropyltriethoxy silane molecules because after the quaternisation reaction of the QC14 there was residual 3-chloropropyltriethoxy silane. Therefore, the QC18/MCM-48@400 has higher amount of quaternary ammonium groups than the QC14/MCM-48@400 which is confirmed by the elemental analysis (**Table 4.3**). There are several studies supporting that increased number of quaternary ammonium groups results in increasing the antibacterial performance of the compound.[38,39] In addition, according to the killing mechanism of the QAS, the longer the alkyl chain length of

the quaternary compound the easier it penetrates the cell membrane and causes the death of the bacteria. As a consequence, the QC18/MCM-48@400 exhibited increased antibacterial performance compared to the QC14/MCM-48@400. The results from the antibacterial tests against *S. aureus* and *E. coli* come as a confirmation of the dual synergetic antibacterial effect of the QAS-modified MCM-48 with the encapsulated Parmetol S15. The antibacterial effect will be permanent even after the release of the encapsulated biocide because of the presence of the covalently attached QAS on the nanoparticle surface.

4.2.2. QAS modified MCM-48 with average size of 120 nm.

4.2.2.1. Surface modification with QAS.

Spherical MCM-48 MSNs with average size of 120 nm were successfully synthesised and characterised in the previous chapter (Chapter 3). In this section, we describe the surface modification of these materials with two different QASs, QC18 and QC14. The samples that we synthesised were: MCM-48 with average size of 120 nm modified with QC18 (QC18/MCM-48@120) and MCM-48 with average size of 120 nm modified with QC14 (QC14/MCM48@120). The synthesised samples were characterised by DRIFT, ζ-potential, TGA and elemental analysis measurements in order to confirm the successful surface modification.

The DRIFT spectra for pristine MCM-48@120, QC18/MCM-48@120 and QC14/MCM-48@120 are shown in **Figure 4.18**. All the samples presented absorption peaks associated to SiO_2 materials: two absorption peaks at 1090 cm^{-1}

and 802 cm^{-1} can be assigned to asymmetric and symmetric Si-O-Si stretching vibrations, respectively, the peak at 960 cm^{-1} is attributed to asymmetric vibration of Si-OH bonding, the peak at 466 cm^{-1} corresponds to Si-O-Si bending vibration, the peak at 1632 cm^{-1} is due to H-O-H bending vibration and the broad peak at 3400 cm^{-1} is assigned to –OH stretching.

Although, there are significant differences between the spectra of the samples. The QC18/MCM-48@120 and QC14/MCM-48@120 samples which are surface modified with organic QASs showed three additional peaks. These peaks are associated with the alkyl chain of QASs and prove that the MCM-48 surface was successfully decorated by QASs. The peak at 1465 cm^{-1} corresponds to the C−H bending vibration and the peaks at 2850 and 2950 cm^{-1} correspond to the C−H stretching. Furthermore, the pristine MCM-48@120 spectrum shows a broad peak at 3400 cm^{-1} assigned to –OH stretching while the QAS modified MCM-48@120 have no peak or significantly decreased peak in this region. In order to obtain the DRIFT spectra, the samples were dried at 100 ^{o}C under high vacuum (for the removal of humidity or physically adsorbed water). Therefore, we can assume that the intense broad peak at 3400 cm^{-1} for the MCM-48@120 is mostly present because of the existence of silanol groups on the surface and within the pore channel system of the material. During the surface modification of MCM-48@120 with QC18 and QC14, the free –OH groups on the surface of the pristine MCM-48@120 react with the $-Si(OCH_3)_3$ groups of the QASs and form covalent bonds. Therefore, the QC18/MCM-48@120 shows no peak and the QC14/MCM-48@120 shows very weak peak at 3400 cm^{-1} since most of the available hydroxyl groups reacted with the QASs.

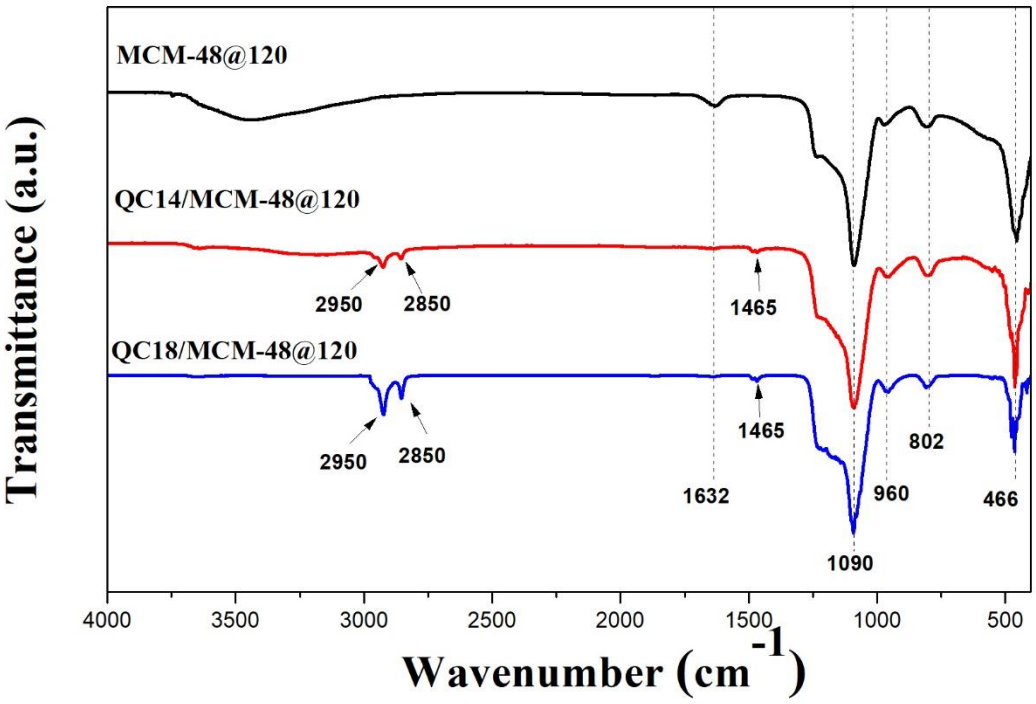

Figure 4.18. DRIFT spectra for pristine MCM-48@120, QC18/MCM-48@120 and QC14/MCM-48@120.

Table 4.5. Wavenumbers for samples: pristine MCM-48@400, QC18/MCM-48@400 and QC14/MCM-48@400.

Wavemumber (cm^{-1})	Assignment
466	Si-O-Si bending vibration
802	Si-O-Si symmetric stretching
960	Si-OH asymmetric vibration
1090	Si-O asymmetric vibration
1465	C−H bending vibration
1632	H-O-H bending vibration
2850	C−H stretching
2950	C−H stretching
3400	–OH stretching

Additional information regarding the surface modification of the pristine MCM-48@120 with QASs was obtained by ζ-potential measurements (**Table 4.6**). Equal amounts of powders from three samples (MCM-48@120, QC18/MCM-48@120 and QC14/MCM-48@120) were dispersed in solutions at pH range from 1.5 to 9.5 and the ζ-potential of the colloidal dispersions was measured. As we expected, the pristine MCM-48@120 were positively charged below their isoelectric point (IEP=pH 2.0) and negatively charged above pH 2 due to the existence of the negatively charged hydroxyl groups on the surface of MCM-48.[34] The ζ-potential values for the pristine MCM-48@120 at pH from 4 to 9.5 were ranging between -30 and -35 mV which is an indication of moderate stability of colloidal dispersions. On the contrary, the ζ-potential values for the QC18/MCM-48@120 and QC14/MCM-48@120 materials were shifted to high positive values in the whole pH range from 1.5 to 9.5. The significant shift of ζ-potential from negative to positive values implies that the positively charged QASs are covalently attached on the surface of pristine MCM-48@120 and the surface modification was successful. In addition, the QAS modified NPs showed higher absolute ζ-potential values (between 32 and 64 mV) compared to the pristine NPs at the whole pH range indicating their better colloidal stability in general.

Table 4.6. ζ-potential measurements for the pristine MCM-48@120, QC18/MCM-48@120 and QC14/MCM-48@120.

pH value	Pristine MCM-48 @120 (mV)	QC18/MCM-48 @120 (mV)	QC14/MCM-48 @120 (mV)
1.5	2.6 ±1	34.2 ±3	32.5 ±2
4	-30.0 ±2	64.4 ±1	52.0 ±1
7.5	-33.2 ±1	53.5 ±2	43.6 ±2
9.5	-35.0 ±1	51.5 ±1	39.2 ±2

Elemental analysis provides further evidence of the successful surface modification of the pristine NPs. **Table 4.7** shows the carbon, hydrogen and nitrogen contents of pristine MCM-48@120, QC18/MCM-48@120 and QC14/MCM-48@120. The pristine MCM-48@120 showed the presence of negligible amount of carbon and hydrogen. The QC18/MCM-48@120 and QC14/MCM-48@120 presented significant increment of carbon, hydrogen and nitrogen in comparison with the pristine NPs. The increased percentage of carbon, hydrogen and nitrogen can be attributed to the presence of the alkyl functional groups and the positively charged nitrogen groups of the covalently attached QAS moieties on the surface of the pristine MCM-48@120.

Table 4.7. Elemental analysis for the pristine MCM-48@120, QC18/MCM-48@120 and QC14/MCM-48@120.

Sample	Elemental analysis (wt %)		
	C	**H**	**N**
Pristine MCM-48@120	2.14	0.63	0
QC18/MCM-48@120	20.24	3.95	1.00
QC14/MCM-48@120	14.62	2.98	0.71

The synthesised materials were further analysed with TGA measurements in order to estimate the amount of grafted QASs on the surface of the pristine NPs. The samples were calcinated under N_2 atmosphere up to 800 ^oC and their weight loss was measured. The pristine MCM-48@120 showed only one major region of weight loss, below 120 ^oC. They presented 2% weight loss below this temperature which is attributed to thermodesorption of physically adsorbed water inside the pristine material.[35] No further weight loss was observed up to 800 ^oC which is an indication of their high thermal stability. The QC18/MCM-48@120 and QC14/MCM-48@120 lost 26.7% and 17.9% of their initial weight, respectively, after calcination under N_2 atmosphere up to 800 ^oC. The QAS modified NPs showed 2% weight loss between 30 and 120 ^oC because of physically adsorbed water inside the materials. Between the calcination temperatures of 230 ^oC and 800 ^oC, the QC18/MCM-48@120 and QC14/MCM-48@120 presented 24.7% and 15.9% further weight loss, respectively, because of the calcination of the grafted QC18 or QC14 groups on the surface of the materials.

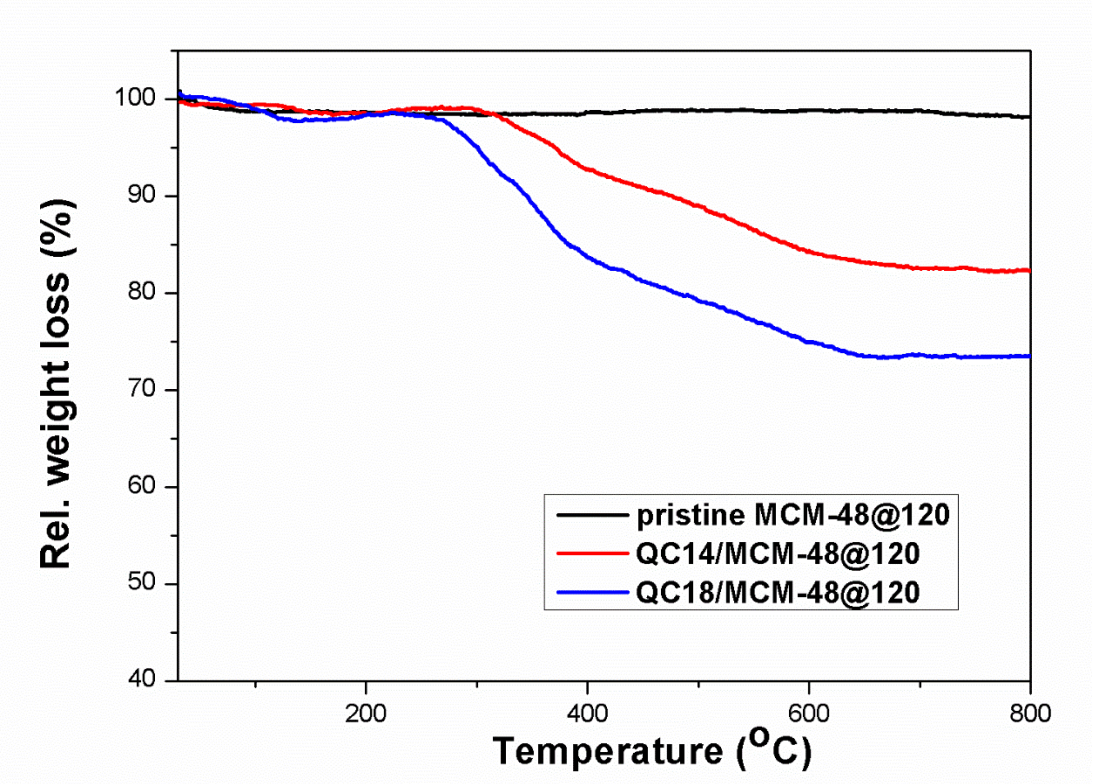

Figure 4.19. TGA curves for the pristine MCM-48@120, QC18/MCM-48@120 and QC14/MCM-48@120.

In the characterisation of the materials by DRIFT, ζ-potential, elemental analysis and TGA, significant differences between the two types of QAS modified MCM-48 were observed. The QC18 molecule has higher molecular weight compared to the QC14 molecule due to the existence of four additional $–CH_2$ groups in the alkyl chain of the QC18 molecule. Thus, the higher mass loss and higher percentage of carbon and hydrogen are expected from the TGA and elemental analysis, as well as, the higher intensity of peaks associated to the C−H vibrations from the DRIFT spectra. Furthermore, as we discussed before in this chapter for the QC14/MCM-48@400, the surface of the QC14/MCM-48@120 was similarly covered with QC14 molecules

and 3-chloropropyltriethoxy silane molecules (absence of positively charged nitrogen and lower molecular weight compared to QC14). As a result, the percentage of carbon, hydrogen and nitrogen from the elemental analysis for the QC14/MCM-48@120 was lower compared to the QC18/MCM-48@120 and the QC14/MCM-48@120 material showed lower weight loss in the TGA, lower positive values of ζ-potential and lower intensity of peaks associated to the C−H vibrations from the DRIFT spectra.

4.2.2.2. Antibacterial performance.

The spherical MCM-48 with smaller average size of 120 nm (MCM-48@120) were surface modified with the two types of QASs and tested against Gram negative and Gram positive bacteria in order to investigate if there is size-dependency at the antibacterial properties of silica-QAS core-shell NPs. There are a few publications in the literature claiming that the antibacterial efficacy of functionalised nanoparticles increases with decreasing size of nanoparticles.[40–43] For the evaluation of the antibacterial activity of synthesised materials, 22mm x 22mm glass slides were coated with a spin coater by using 1 mL of either pristine or modified nanoparticles dispersed in ethanol solution (2 wt %) and tested against Gram-negative *E. Coli* and Gram-positive *S. aureus*. The pristine MCM-48@120 was used as a negative control since no antibacterial activity is expected from this material. The relative number of viable bacteria adhered on the glass slide coated with pristine MCM-48@120 was defined as 100%.

Figure 4.20 illustrates the relative number of viable bacteria *E. coli* and **Figure 4.21** shows representative photographs of *E. coli* colonies grown on agar plates after exposure on glass slides spin-coated with pristine MCM-48@120, QC18/MCM-48@120 and QC14/MCM-48@120. As can been seen from these two figures, the QAS modified MCM-48 presented significant antibacterial properties. Specifically, the QC18/MCM-48@120 and QC14/MCM-48@120 reduced the number of viable bacteria by 94% and 83%, respectively, in comparison with the pristine MCM-48@120.

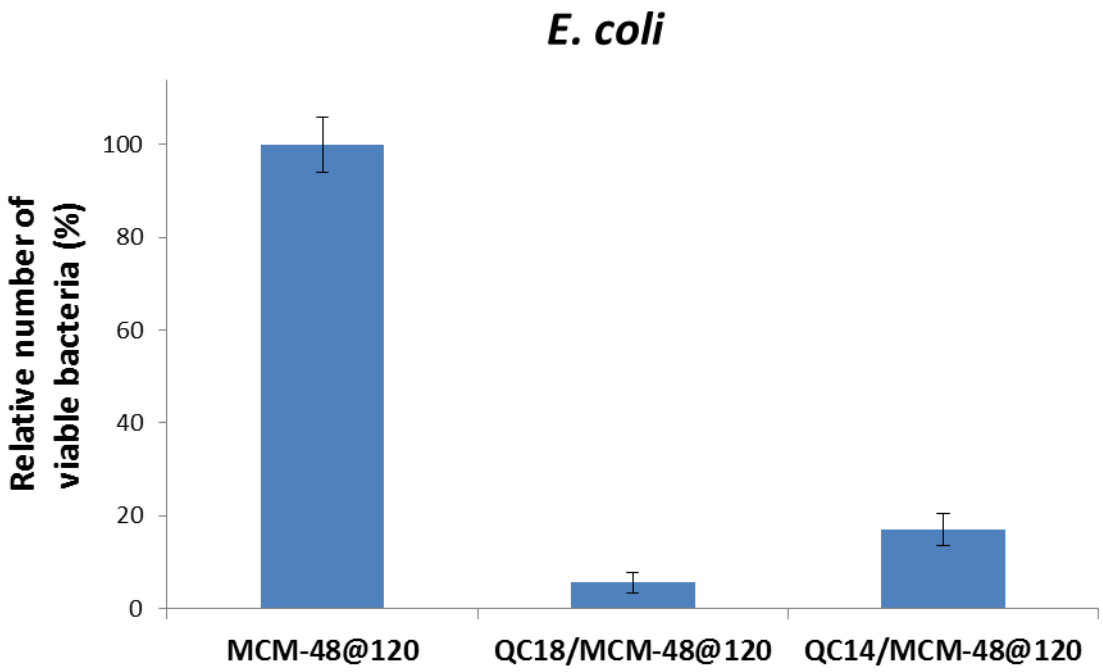

Figure 4.20. Relative number of viable bacteria (*E. coli*) after testing on glass slides spin-coated with pristine MCM-48@120, QC18/MCM-48@120 and QC14/MCM-48@120. Statistically significant differences between the samples ($p < 0.0005$).

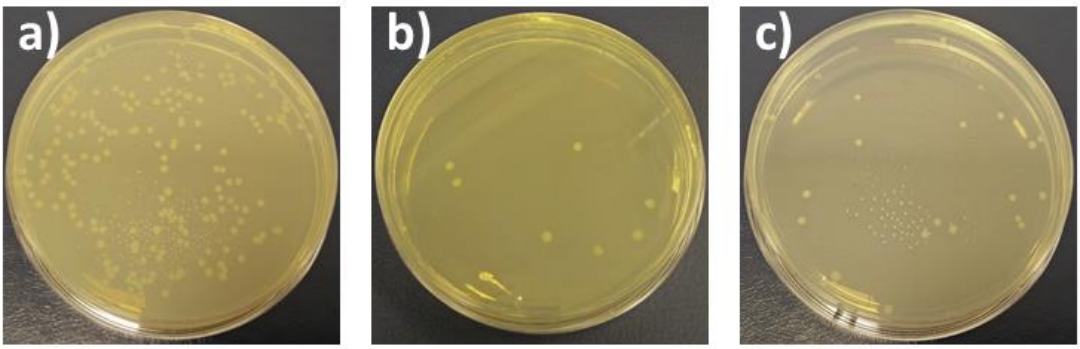

Figure 4.21. Representative photographs of *E. coli* colonies grown on agar plates after overnight incubation, exposed on glass slides coated with a) pristine MCM-48@120, b) QC18/MCM-48@120 and c) QC14/MCM-48@120.

Figure 4.22 shows the relative number of viable bacteria *S. aureus* and **Figure 4.23** shows representative photographs of *S. aureus* colonies grown on agar plates after exposure on glass slides spin-coated with pristine MCM-48@120, QC18/MCM-48@120 and QC14/MCM-48@120. The QC18/MCM-48@120 and QC14/MCM-48@120 exhibited high antibacterial properties by killing 97% and 87%, respectively, of the exposed *S. aureus* bacteria.

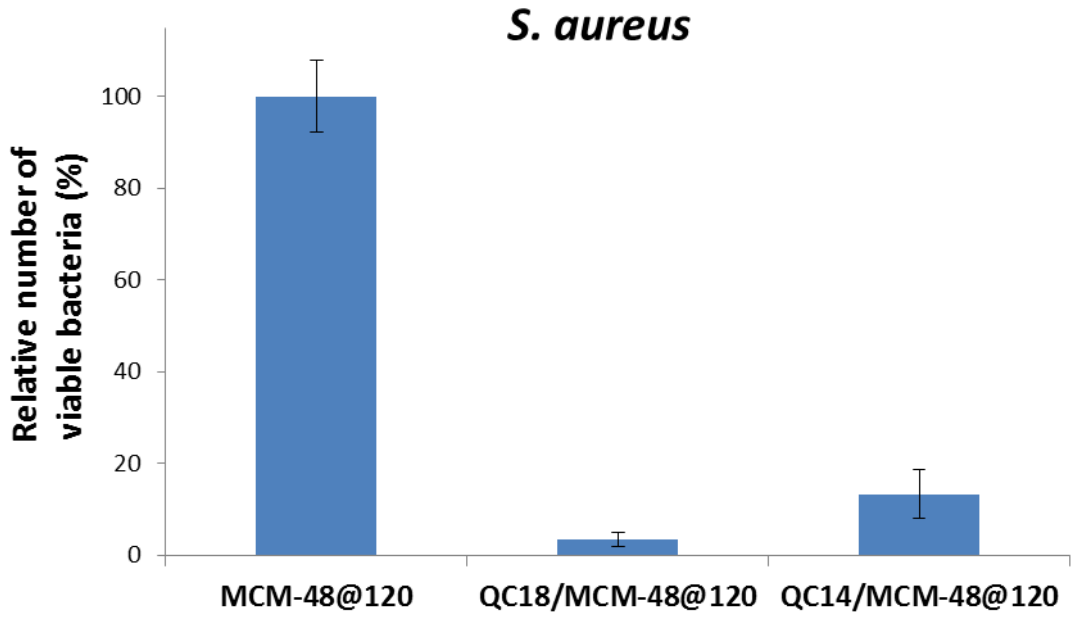

Figure 4.22. Relative number of viable bacteria (*S. aureus*) after testing on glass slides spin-coated with pristine MCM-48@120, QC18/MCM-48@120 and QC14/MCM-48@120. Statistically significant differences between the samples ($p < 0.0005$).

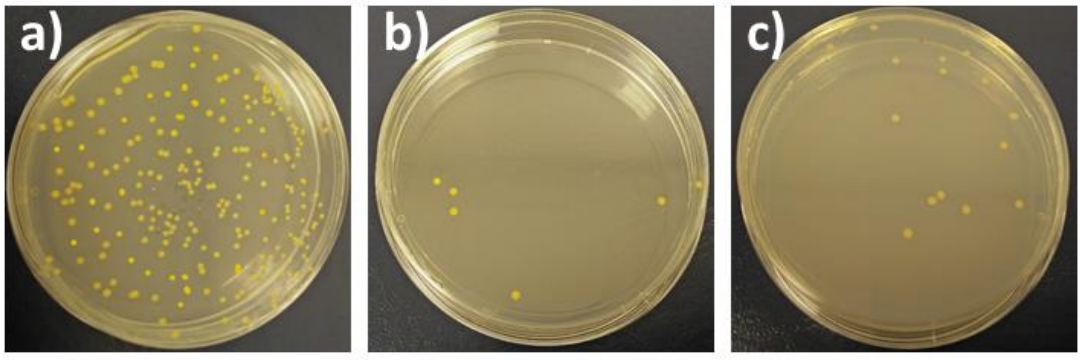

Figure 4.23. Representative photographs of *S. aureus* colonies grown on agar plates after overnight incubation, exposed on glass slides coated with a) pristine MCM-48@120, b) QC18/MCM-48@120 and c) QC14/MCM-48@120.

The two types of QASs used for the surface modification provide antibacterial properties to the functionalised materials against both types of bacteria, Gram-negative *E. coli* and Gram-positive S. *aureus*. Between the two modified NPs, the QC18/MCM-48@120 demonstrated superior antibacterial performance compared to the QC14/MCM-48@120 against both types of bacteria. One possible explanation is that the longer alkyl chains of the QC18 molecules provide better antibacterial properties to the functionalised materials compared to the shorter alkyl chains of the QC14 molecules. It has been found that QAS with alkyl chain length from C8 and higher present high antimicrobial activity.[27] Furthermore, according to the killing mechanism of the QAS, the longer the alkyl chain length of the quaternary compound the easier it penetrates the cell membrane and causes the death of the bacteria.[22,23] Moreover, as we discussed above in this chapter, the QC14/MCM-48@120 surface is covered with QC14 molecules and 3-chloropropyltriethoxy silane molecules which results in lower number of quaternary ammonium groups for this material (confirmed from elemental analysis, **Table 4.7**) and leads to decreased antibacterial performance. There are several studies supporting that increased number of quaternary ammonium groups results in increasing the antibacterial performance of the compound.[38,39]

Moreover, the QAS modified NPs with average size of 120 nm demonstrated slightly higher antibacterial efficacy in comparison with their counterparts with average size of 400 nm. In the *E. coli* tests, the QC18/MCM-48@400 and QC14/MCM-48@400 killed 89% and 77%, respectively, of the exposed bacteria while the QC18/MCM-48@120 and QC14/MCM-48@120 killed 94% and 83%, respectively, of the exposed bacteria. In the *S. aureus* tests, the QC18/MCM-48@400 and QC14/MCM-

48@400 killed 94% and 78%, respectively, of the exposed bacteria while the QC18/MCM-48@120 and QC14/MCM-48@120 killed 97% and 87%, respectively, of the exposed bacteria. As mentioned earlier, there are a few studies supporting that it is possible to increase the antibacterial efficacy of silica-QAS core-shell NPs by decreasing their size. Probably because the smaller antibacterial agents have enlarged surface area compared to larger antibacterial agents, leading to enhanced antibacterial performance based on the same amount.[40–43] **Figure 4.24** shows representative images for *S. aureus* and *E. coli* bacteria, MCM-48@400 and MCM-48@120. The size of *S. aureus* bacteria is ranging between 0.5 and 1 μm in diameter while the size for *E. coli* is ranging between 1 and 3 μm in length and approximately 0.3 μm in diameter. As we reported in chapter 3, the size for MCM-48@400 is ranging between 200 and 600 nm in diameter and for MCM-48@120 is ranging between 90 and 170 nm in diameter. Thus, MCM-48@120 have significantly lower size than the two types of bacteria and it is easier for the QAS modified MCM-48@120 to penetrate and cause disruption to the cell membrane of the bacteria. On the other hand, it is more challenging for the QAS modified MCM-48@400 to achieve similar effect since their size is bigger and very similar with the size of the bacteria, especially with *S. aureus*.

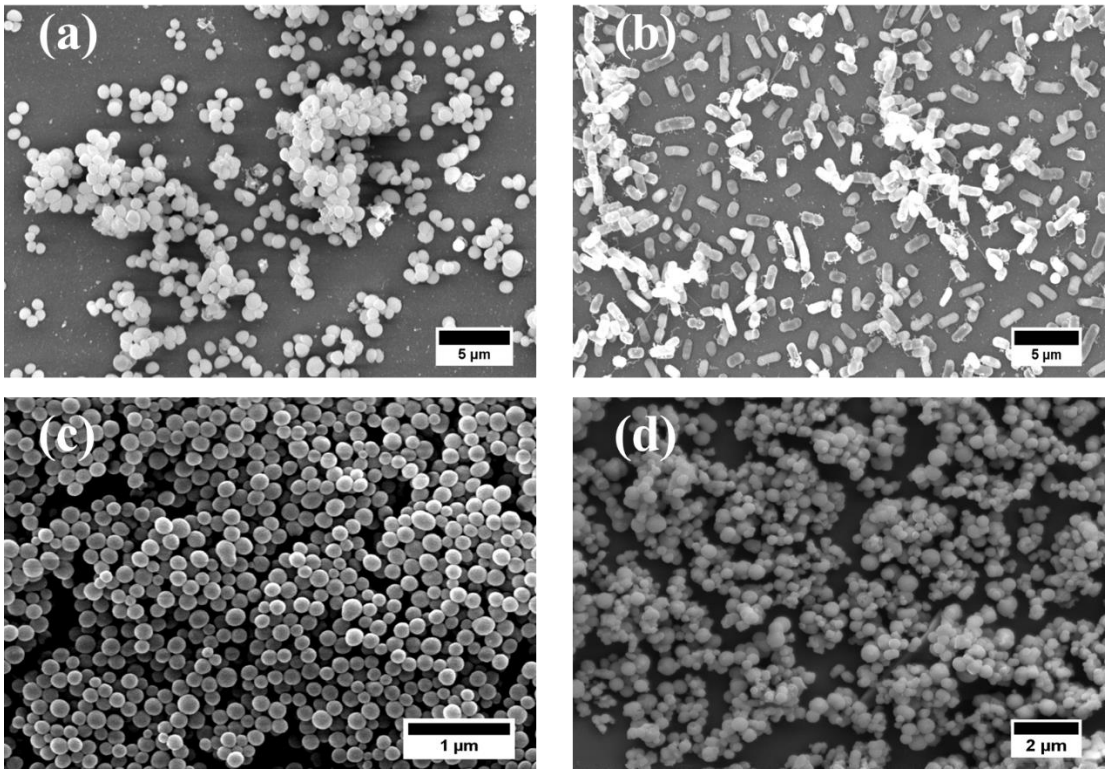

Figure 4.24. SEM images for (a) *S. aureus* bacteria, (b) *E. coli* bacteria, (c) MCM-48@400 and (d) MCM-48@120.

References

[1] J. A. Callow, M. E. Callow, *Nat. Commun.* **2011**, *2*, 244.

[2] M. E. Callow, J. A. Callow, *Biologist* **2002**, *49*, 10.

[3] M. P. Schultz, J. A. Bendick, E. R. Holm, W. M. Hertel, *Biofouling* **2011**, *27*, 87.

[4] I. Fitridge, T. Dempster, J. Guenther, R. de Nys, *Biofouling* **2012**, *28*, 649.

[5] D. M. Yebra, S. Kiil, K. Dam-Johansen, *Prog. Org. Coatings* **2004**, *50*, 75.

[6] E. Almeida, T. C. Diamantino, O. de Sousa, *Prog. Org. Coatings* **2007**, *59*, 2.

[7] IMO, *Int. Marit. Organ.* **2002**, *44*, 1.

[8] J. R. Adams, A. Antoniadou, C. O. Hunt, P. Bennett, I. W. Croudace, R. N. Taylor, R. B. Pearce, G. P. Earl, N. C. Flemming, J. Moggeridge, T. Whiteside, K. Oliver, A. J. Parker, *Int. J. Naut. Archaeol.* **2013**, *42*, 60.

[9] M. Lejars, A. Margaillan, C. Bressy, *Chem. Rev.* **2012**, *112*, 4347.

[10] H. Gao, D. Wen, G. B. Sukhorukov, *J. Mater. Chem. B* **2015**, *3*, 1888.

[11] Z. Zheng, Z. Chang, G.-K. Xu, F. McBride, A. Ho, Z. Zhuola, M. Michailidis, W. Li, R. Raval, R. Akhtar, D. Shchukin, *ACS Nano* **2017**, *11*, 721.

[12] Z. Zheng, M. Schenderlein, X. Huang, N. J. Brownbill, F. Blanc, D. Shchukin, *ACS Appl. Mater. Interfaces* **2015**, *7*, 22756.

[13] H. Gao, O. A. Goriacheva, N. V. Tarakina, G. B. Sukhorukov, *ACS Appl.*

Mater. Interfaces **2016**, *8*, 9651.

[14] E. M. Shchukina, D. G. Shchukin, *Adv. Drug Deliv. Rev.* **2011**, *63*, 837.

[15] M. Andersson Trojer, L. Nordstierna, J. Bergek, H. Blanck, K. Holmberg, M. Nydén, *Adv. Colloid Interface Sci.* **2015**, *222*, 18.

[16] F. Maia, A. P. Silva, S. Fernandes, A. Cunha, A. Almeida, J. Tedim, M. L. Zheludkevich, M. G. S. Ferreira, *Chem. Eng. J.* **2015**, *270*, 150.

[17] G. Sørensen, A. L. Nielsen, M. M. Pedersen, S. Poulsen, H. Nissen, M. Poulsen, S. D. Nygaard, *Prog. Org. Coatings* **2010**, *68*, 299.

[18] M. Tischer, G. Pradel, K. Ohlsen, U. Holzgrabe, *ChemMedChem* **2012**, *7*, 22.

[19] Y. Xue, H. Xiao, Y. Zhang, *Int. J. Mol. Sci.* **2015**, *16*, 3626.

[20] K. Hegstad, S. Langsrud, B. T. Lunestad, A. A. Scheie, M. Sunde, S. P. Yazdankhah, *Microb. Drug Resist.* **2010**, *16*, 91.

[21] J. Y. Maillard, *Symp. Ser. Soc. Appl. Microbiol.* **2002**, 16S.

[22] T. Tashiro, *Macromol. Mater. Eng.* **2001**, *286*, 63.

[23] A. Davies, M. Bentley, B. S. Field, *J. Appl. Bacteriol.* **1968**, *31*, 448.

[24] B. Gottenbos, H. C. Van Der Mei, F. Klatter, P. Nieuwenhuis, H. J. Busscher, *Biomaterials* **2002**, *23*, 1417.

[25] N. Nurdin, G. Helary, G. Sauvet, *J. Appl. Polym. Sci.* **1993**, *50*, 663.

[26] M. J. Saif, J. Anwar, M. A. Munawar, *Langmuir* **2009**, *25*, 377.

[27] N. Yoshihiro, H. Hiroyuki, T. Takahiko, K. Hiroki, H. Tokunaru, S. Isao, *Appl. Environ. Microbiol.* **1984**, *47*, 513.

[28] K. Schumacher, M. Grün, K. . Unger, *Microporous Mesoporous Mater.* **1999**, *27*, 201.

[29] K. Schumacher, P. I. Ravikovitch, A. Du Chesne, A. V Neimark, K. K. Unger, *Langmuir* **2000**, *16*, 4648.

[30] T.-W. Kim, P.-W. Chung, V. S.-Y. Lin, *Chem. Mater.* **2010**, *22*, 5093.

[31] T. N. Borodina, D. O. Grigoriev, M. A. Carillo, J. Hartmann, H. Moehwald, D. G. Shchukin, *ACS Appl. Mater. Interfaces* **2014**, *6*, 6570.

[32] P. Majumdar, E. Lee, N. Gubbins, D. A. Christianson, S. J. Stafslien, J. Daniels, L. Vanderwal, J. Bahr, B. J. Chisholm, *J. Comb. Chem.* **2009**, *11*, 1115.

[33] J. Antonio Alves Júnior, J. Baptista Baldo, *New J. Glas. Ceram.* **2014**, *04*, 29.

[34] S.-H. Wu, C.-Y. Mou, H.-P. Lin, *Chem. Soc. Rev.* **2013**, *42*, 3862.

[35] M. Kruk, M. Jaroniec, R. Ryoo, Sang Hoon Joo, *Chem. Mater.* **2000**, *12*, 1414.

[36] D. G. Shchukin, E. Shchukina, *Curr. Opin. Pharmacol.* **2014**, *18*, 42.

[37] Z. Zheng, X. Huang, M. Schenderlein, D. Borisova, R. Cao, H. Möhwald, D. Shchukin, *Adv. Funct. Mater.* **2013**, *23*, 3307.

[38] R. Kügler, O. Bouloussa, F. Rondelez, *Microbiology* **2005**, *151*, 1341.

[39] C. Z. Chen, N. C. Beck-Tan, P. Dhurjati, T. K. van Dyk, R. A. LaRossa, S. L. Cooper, *Biomacromolecules* **2000**, *1*, 473.

[40] J. Song, H. Kong, J. Jang, *Colloids Surfaces B Biointerfaces* **2011**, *82*, 651.

[41] J. Song, H. Kong, J. Jang, *Chem. Commun. (Camb).* **2009**, 5418.

[42] J. Jang, Y. Kim, *Chem. Commun.* **2008**, 4016.

[43] H. Kong, J. Jang, *Langmuir* **2008**, *24*, 2051.

Chapter 5:

Antibacterial/Antifouling Coatings Based on Dual Functionalised MSNs

5.1. Introduction

At present, the commercially available antifouling coatings are either biocide-releasing or not-biocide-releasing based antifouling coatings.[1] Each system experiences advantages and disadvantages. For instance, the not-biocide-releasing antifouling coatings can prevent or inhibit the attachment of bacteria and the formation of biofilms but without achieving 100% efficiency. On the other hand, the biocide-releasing coatings are more effective but their antifouling activity has being diminished during their lifetime.[2,3] Usually, the biocides are simply embedded and dispersed molecularly in the polymer matrix of the coating and the antifouling action becomes short due to premature depletion of the active substance to the surrounding environment. Therefore, excessive amounts of biocides are required in order to maintain the antifouling activity of the coating for longer period which may pollute the marine environment and harm non target species.[4] One method to address this problem is the encapsulation, a technique that has been used successfully in the past for drug delivery, biomedical systems, protection against corrosion and energy storage systems.[5–10] Encapsulation provides a methodology to decrease and control the release rate of the biocides and, at the same time, protect them from the surrounding environment.[11–14]

During recent years, an increased attention has been paid to the engineered nanoparticles (ENPs), as potential antibacterial-antifouling inhibitors due to their unique physicochemical properties. Low concentrations of nanoparticles in coating formulations exhibit enhanced properties as compared to conventional microscale fillers in the coatings. Enhanced properties include mechanical and optical

characteristics, antibacterial/antifouling activity and wettability, amongst others that can be improved by modifying nanoparticles in the coating formulations.[15–18] Most commonly used ENPs for antibacterial and antifouling applications are based on functionalised carbon nanotubes, TiO_2, ZnO, chitosan and silver nanoparticles.[19–21] However, the use of ENPs based on silica nanoparticles as functional fillers for antibacterial/antifouling coating is not well studied yet, especially with enhanced dual functionalisation.

In this chapter, we are focused on the development of novel nanostructured coatings for antibacterial/antifouling applications. For this purpose, we synthesised dual functionalised mesoporous silica nanoparticles (MSNs) as functional fillers for the coatings.[22] The surface of the MSNs was modified with two different types of quaternary ammonium salts (QASs) having effective antibacterial/antifouling properties.[23,24] The QASs provide to the coating formulations the necessary hydrophobic properties and almost permanent antibacterial/antifouling effect due to the covalent attachment on the surface of MSNs. Afterwards, the QAS-modified MSNs were loaded with a liquid biocide (Parmetol S15) in order to achieve an enhanced dual antibacterial/antifouling effect.

The synthesised nanoparticles were added into a biocide-free paint and applied on PVC panels (**Figure 5.1**). The nanoparticles were dispersed homogeneously in the paint and increased the surface roughness and hydrophobic properties of the paints. Furthermore, the paints resulted in low toxicity against non-target species and excellent antibacterial and antifouling properties in a six-month field test trial under Red Sea water conditions. Through our work, we demonstrate the formulation of

novel antibacterial/antifouling paints for long term applications that can be used as low toxic and environmental friendly alternative of TBT-loaded paints. Our paints combine two basic approaches of the paint industry (biocide-releasing and not-biocide-releasing) in one formulation. The modified MSNs can provide permanent antibacterial/antifouling properties to the coating formulations due to the existence of the chemically attached QAS groups on the nanoparticles surface (not-biocide-releasing approach), whereas, the encapsulated biocide results in an enhanced dual antibacterial/antifouling performance (biocide-releasing approach).

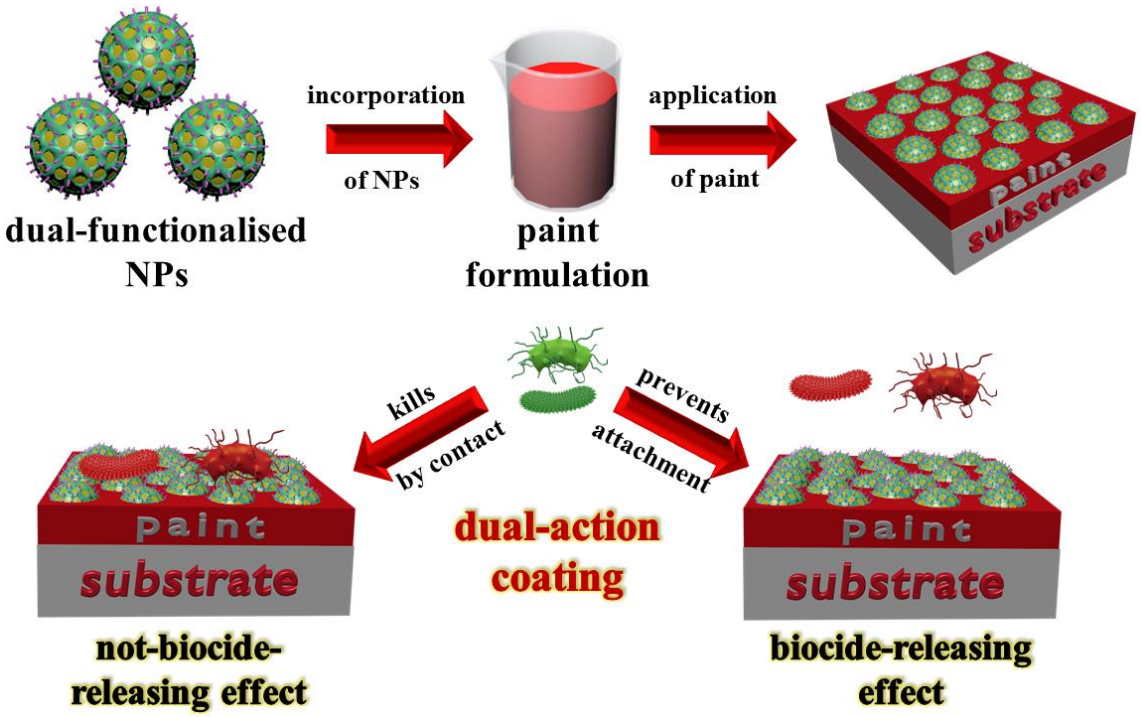

Figure 5.1. Schematic illustration for the formulation of paints based on dual functionalised NPs.

5.2. Experimental

5.2.1. Preparation of coating formulations containing modified mesoporous silica nanoparticles.

For the preparation of the test paints, as-synthesised modified MCM-48@400 were suspended mechanically via a homogeniser (Bio-Gen PRO200, Pro Scientific) in a polymeric paint matrix. The polymeric paint matrix (pristine paint, self-polishing coating based on silyl acrylate and resin binders) was developed by Jotun and it is a solvent based biocide-free coating formulation. The concentration of the nanoparticles in the paints was adjusted to either 2 or 5 wt % and four different paint formulations with two concentrations of active nanocontainers were prepared. Paint 1: pristine paint + 2 or 5 wt % QC18/Parm/MCM-48@400, Paint 2: pristine paint + 2 or 5 wt % QC14/Parm/MCM-48@400, Paint 3: pristine paint + 2 or 5 wt % QC18/MCM-48@400 and Paint 4: pristine paint + 2 or 5 wt % QC14/MCM-48@400.

5.2.2. Antibacterial activity of coating formulations containing modified MCM-48.

For the evaluation of the antibacterial properties of coating formulations, 5cm x 5cm PVC plates were coated with the pristine paint and the nanocontainer-doped paints (**Figure 5.2**) and tested against Gram-positive *S. aureus* and Gram-negative *E. coli* bacteria according to ISO 22196:2011 protocol.[25] Firstly, the *E. coli* (ATCC 10536)

and *S. aureus* (ATCC 25923) strains were grown on nutrient broth agar (NB) for 24 h at 37 ºC. The test inoculum was prepared by transferring one colony of the test bacteria in a small amount of 1/500 NB and after serial dilutions the bacterial concentration was between 2.5 x 10^5 and 10 x 10^5 colony forming unit per ml (CFU/ml). The coated PVC test specimens were placed in sterile Petri dishes and inoculated by 0.4 ml of the test inoculum. A sterile polypropylene film cover (4cm x 4cm) was placed on top of the liquid and the inoculum was spread to its edges. The inoculated specimens were incubated at 35 ºC for 24 h under humid conditions (above 90%). After the incubation, the remaining bacteria on the test specimens and the cover film were completely recovered in 10 ml of the required recovery solution. 100 µl of the recovery solution with the surviving test bacteria was added to 100 µl of NB medium in a proprietary oxygen biosensor 96-well round bottom microplate containing 50 µl of 2000 ppm tris(bathophenanthroline)ruthenium (II) chloride adsorbed to controlled-pore glass in a PDMS matrix (OBS). A thin film of petroleum oil was placed on top of the liquid to limit oxygen exchange from the air to the liquid. The plate was incubated in a Becton-Dickinson DTX880 fluorescence microplate reader at 37°C for 16 hours and the fluorescence (Ex: 450 nm, Em: 630 nm) of the OBS was read out from the bottom every 10 min. The time-to-threshold (3 times above background) was determined for each sample as compared to a calibration curve of a ten-fold serial dilution of the test bacteria from 1x10^8 to 1x10^1 CFU's of bacteria. The growth of *S. aureus* and *E. coli* was determined according to the following equation:

$$Bacteria\ growth\ (\%) = \left(1 - \left(\frac{A - B}{A}\right)\right) \times 100$$

where A is the calculated number of CFU's in the control sample based on the calibration curve (PVC panel covered with pristine paint without any biocides) and B is the calculated number of CFU's in the tested sample (PVC panel covered with pristine paint which contains the synthesised modified nanoparticles).

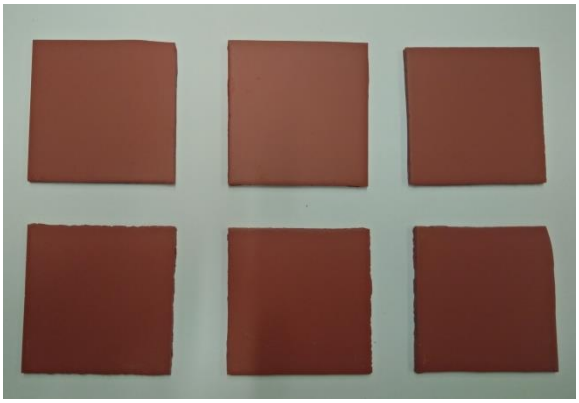

Figure 5.2. 5cm x 5cm PVC plates coated with the pristine paint and the nanocontainer-doped paints, used for the antibacterial tests.

5.2.3. Anti-macrofouling assay.

In order to obtain information for the anti-macrofouling activity, tissue culture plates (size 6 wells) were coated with the pristine and the nanocontainer-doped paints and tested against the *Brachidontes pharaonis* mussels (~2 cm length), (**Figure 5.3**). They were collected in the North Beach of Eilat (29°32'N 34°57'E) and placed in aerated acclimation aquarium containing filtered seawater (FSW, 0.45 μm) 48 hours

prior to the experiment. Only mussels that produced byssus threads in the acclimation aquarium have been placed in coated culture plates for 72 hours, with 12 individuals per treatment. After 72 hours, the mussels' attachment was examined under a dissecting microscope and the number of developed byssus threads was counted. Mussels were then transferred to a recovery test with untreated plates (contained only FSW, 0.45 μm) for 72 hours, and then similarly examined for attachment and byssus threads. The anti-macrofouling efficacy of the paints was presented as percentage of mussels attached after the 72 hours of exposure in the coated plates. Information for the toxicity of the paints against the mussels was obtained from the percentage of mussels attached after the 72 hours of exposure in the recovery test. During the test, ambient temperature, photoperiod (light:dark cycle of 12:12 h), pH (8.18 ± 0.03), and salinity (S = 40.5 ± 0.5) were kept controlled.[26] The average of byssus threads was presented after square root transformation of the raw data.

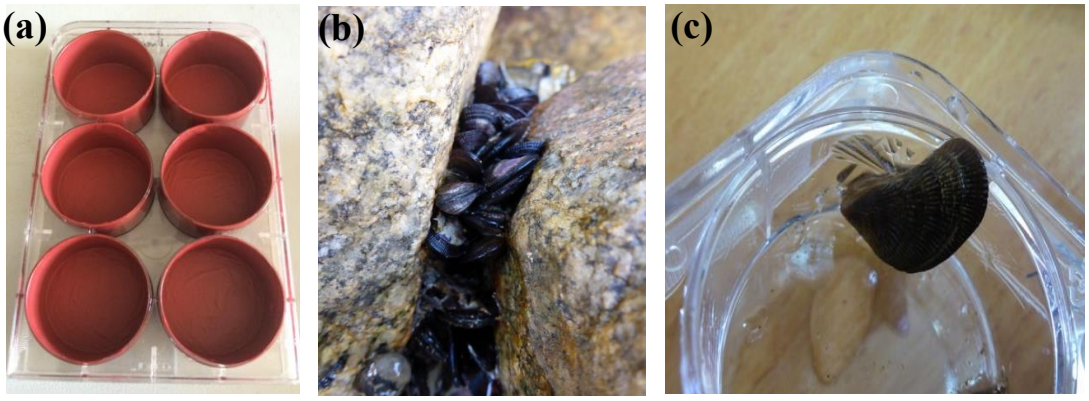

Figure 5.3. Tissue culture plate (size 6 wells) coated with paint for the anti-macrofouling tests (a), Red Sea *Brachidontes pharaonis* mussels attached on a rock (b) and Red Sea *Brachidontes pharaonis* mussel attached on the wall of a tissue culture plate (c).

5.2.4. Non-target toxicity test.

The toxicity of the paints was evaluated by a brine shrimp toxicity assay. Eggs of *Artemia salina* were hatched in aerated seawater at 30°C for 24-30 hours. After hatching, the nauplii were transferred in tissue culture plates (size 6 wells, each containing 10 animals, n=60) coated with the pristine and the nanocontainer-doped paints, and incubated at 24±2°C for 24 hours. The percentage of nauplii mortality (lack of mobility) was then recorded.[27,28]

5.2.5. Antifouling activity of coating formulations containing modified MCM-48 (Field Test).

In order to evaluate the antifouling performance of the nanocontainer-loaded paints, we carried out a field test trial in northern Red Sea, Eilat, Israel. PVC panels of 7 cm x 10 cm coated with five different types of paints (pristine paint and paints 1-4) were immersed in Eilat, northern Gulf of Aqaba (Israel) for a six months field test in order to achieve a realistic assessment of their antifouling properties. PVC panels coated with pristine paint were used as control samples. The coated PVC panels were placed on a floating structure made of a stainless steel frame on which two PVC boards were attached and submerged at a depth of 8-9 m (**Figure 5.4**). Each panel was attached by nuts to two stainless steel bolts. The panels were photographed underwater monthly during the exposure period and the percentage of fouling covering the panels was determined by using the image analysis software Image J.[29] The quantification of the fouling and the biofilm provided an overview of the coatings performance.

Figure 5.4. Immersed floating structure in Eilat (northern Red Sea) with the experimental panels at the day of deployment and during the underwater photographs.

5.3. Results and discussion

5.3.1. Distribution of modified nanoparticles in the coating formulations.

The homogeneous dispersion of the modified nanoparticles inside the coating formulations is very critical for the performance of the coating since poor distribution of the nanoparticles and big aggregates may undermine its antifouling properties. For this reason, we used the FIB-SEM technique in order to obtain cross section images and investigate the dispersion of the different types of nanoparticles inside the pristine paint (**Figure 5.5**). The cross section image for the pristine paint showed the existence of nonhomogeneous particles with several sizes within the range of a few hundred nm to 7 μm. The pristine paint mainly consists of the polymeric matrix (binder) but the addition of pigments and different types of

additives is essential in order to improve the properties of the paint such as colour, viscosity, opacity, etc. Therefore, the variation of particles' size and morphology can be attributed to the different components of the initial coating formulation. On the other hand, the cross-section images of the nanocontainer-modified paints present clearly uniform spherical silica nanoparticles homogeneously dispersed in the polymeric matrix.

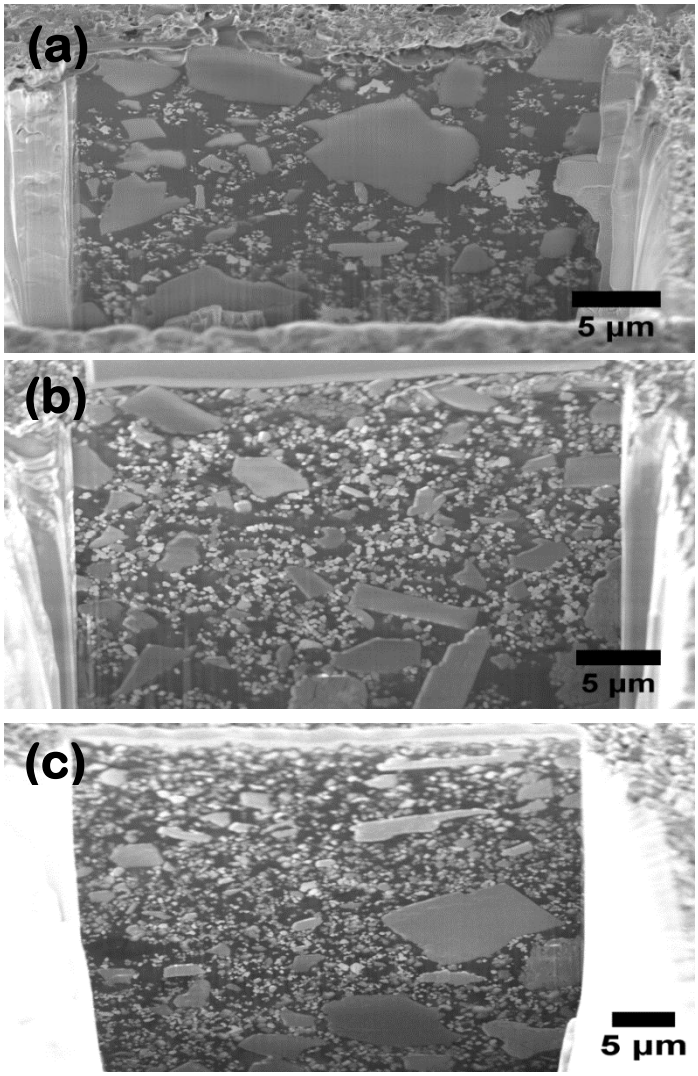

Figure 5.5. Cross section images (FIB-SEM) for the (a) pristine paint without any modified nanoparticles inside, (b) paint 1 containing 5 wt % QC18/Parm/MCM-48@400 and (c) paint 3 containing 5 wt % QC18/MCM-48@400.

Further confirmation of the good dispersity of the nanoparticles in the paints was achieved by using a grindometer according to the ISO 1524 protocol (**Figure 5.6**). The fineness of grind for the nanocontainer-treated coatings was between 18 and 22 μm, whereas for the pristine paint was 18 μm (**Table 5.1**). The nanocontainer-doped paints 1 and 2 presented similar values fineness of grind with the pristine paint while paints 3 and 4 containing the single functionalised NPs presented slightly higher values. This behaviour will be explained with more details in the following section for the surface roughness of coated PVC plates.

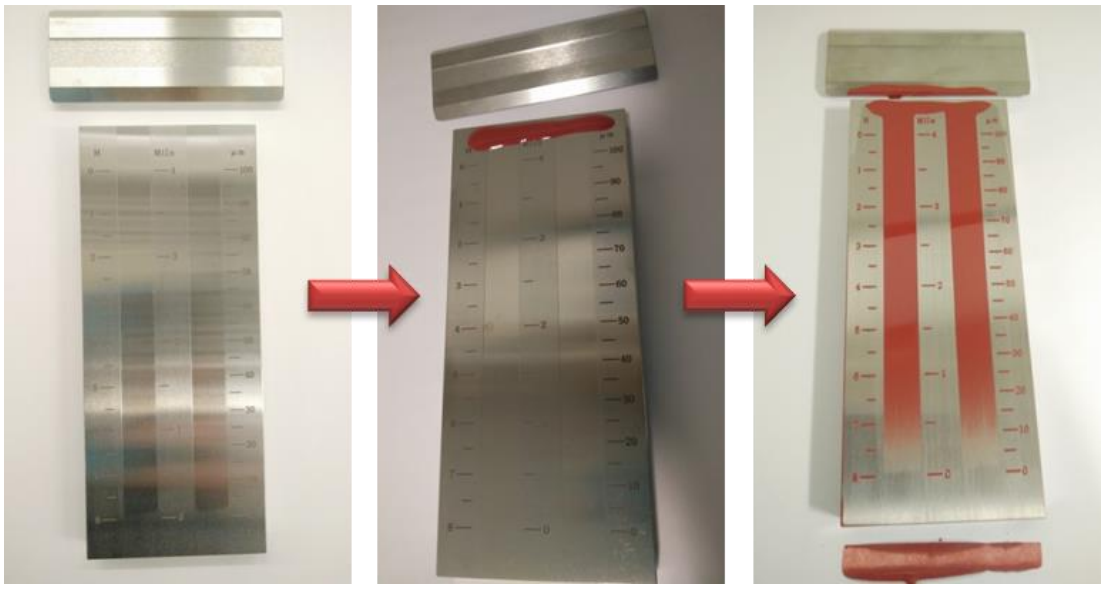

Figure 5.6. Quick indication of the particle size distribution for the synthesised coating formulations by using a two channel grindometer.

Table 5.1. Fineness gauge values for the pristine paint, paint 1: pristine paint + 5 wt % QC18/Parm/MCM-48@400, paint 2: pristine paint + 5 wt % QC14/Parm/MCM-48@400, paint 3: pristine paint + 5 wt % QC18/MCM-48@400 and paint 4: pristine paint + 5 wt % QC14/MCM-48@400.

Sample	Fineness of Grind (μm)
Pristine Paint	18 ±1
Paint 1	18 ±1
Paint 2	19 ±1
Paint 3	21 ±1
Paint 4	22±2

5.3.2. Surface roughness.

The formulated paints were applied on 5cm x 5cm PVC plates and the average surface roughness of the treated substrates was measured by a contact stylus profiler (AMBIOS XP-Plus Stylus Profiler). **Figure 5.7** shows the average roughness values of PVC plates coated with the formulated paints for 3 mm projected area. The addition of the nanoparticles in the pristine paint increased the surface roughness of the coated plates. The average roughness for the pristine paint was 440 nm, it was between 650-700 nm for the paints 1 and 2 containing the dual functionalised nanocontainers (QAS-modified nanoparticles loaded with biocide) and between 1000-1120 nm for the paints 3 and 4 containing the single functionalised nanocontainers (QAS-modified nanoparticles). It is common that the addition of the extra solid component to the pristine coating formulation increases coating roughness, especially in the case of the nanoparticles where aggregates can be

formed easily during the mixing process and their separation is challenging. Variation of the roughness values for the nanocontainer-doped paints can be explained by the different types of nanoparticles in the formulations. The paints 3 and 4 contain QAS-functionalised nanoparticles. The surface modification increases the aggregation between the nanoparticles since the QAS molecules can be covalently attached with neighbouring nanoparticles which results in the formation of aggregates. Paints 1 and 2 contain QAS-modified nanoparticles loaded with an additional biocide. Before the encapsulation process, the modified nanoparticles were stirred under sonication in the liquid biocide for several minutes and, as a result, most of the aggregates were broken. Hence, lower amount of aggregates results in lower values of surface roughness. The average roughness measurements are consistent with the obtained values for the fineness of grind (**Table 5.1**) where the paints 3 and 4 showed higher size of solid materials compared with the paint 1 and 2.

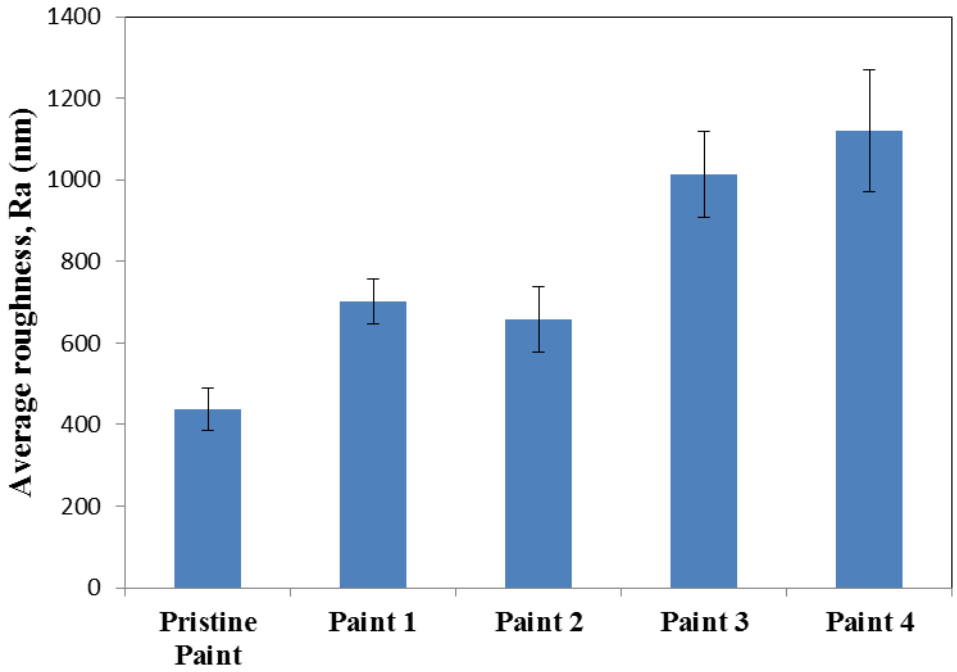

Figure 5.7. Surface roughness values of PVC panels coated with the pristine paint, paint 1: pristine paint + 5 wt % QC18/Parm/MCM-48@400, paint 2: pristine paint + 5 wt % QC14/Parm/MCM-48@400, paint 3: pristine paint + 5 wt % QC18/MCM-48@400 and paint 4: pristine paint + 5 wt % QC14/MCM-48@400. The samples were measured with a contact stylus profiler (AMBIOS XP-Plus Stylus Profiler), projected area was 3 mm.

In order to achieve a more realistic assessment of the surface roughness values for the treated substrates with the formulated paints, the coated panels were tested with a 3D non-contact optical profiler (Talysurf CCI-HD). This optical profiler allows scanning larger areas compared to the stylus profiler with high speed and extraordinary sensitivity. Stylus type profilers are usually relatively slow especially if 3D roughness parameters are defined. Optical methods are therefore preferable. As can been seen in **Figure 5.8**, 3D surface roughness profiles for the coated substrates were obtained for scanned area of 100 mm^2. The values of the average roughness for the treated substrates under study are provided in

Table 5.2. The paints 1 & 2 and the pristine paint showed similar values of average roughness ranging from 2.18 to 2.84 μm while paints 3 and 4 showed values at 4.62 and 5.76 μm, respectively. It seems that the addition of the dual functionalised NPs (paints 1 & 2) in the pristine paint had no significant influence in the roughness of the coatings. As for the paints 3 and 4 containing the single functionalised NPs, the roughness of the coatings was increased by the addition of the QAS-modified NPs. These results are in consistency with the results obtained from the stylus profiler and the fineness of grid for the paints. Therefore, the 3D non-contact optical profiler provides further evidence that the dual functionalised NPs are better dispersed in the pristine paint compared to the single functionalised NPs. As discussed previously, possible explanation for this behavior of the formulated paints is the sonication process prior to the encapsulation of the biocide. Probably, some of the aggregates created during the surface modification are breaking from the strong sonication which allows the dual functionalised NPs to be dispersed more homogeneously in the pristine paint.

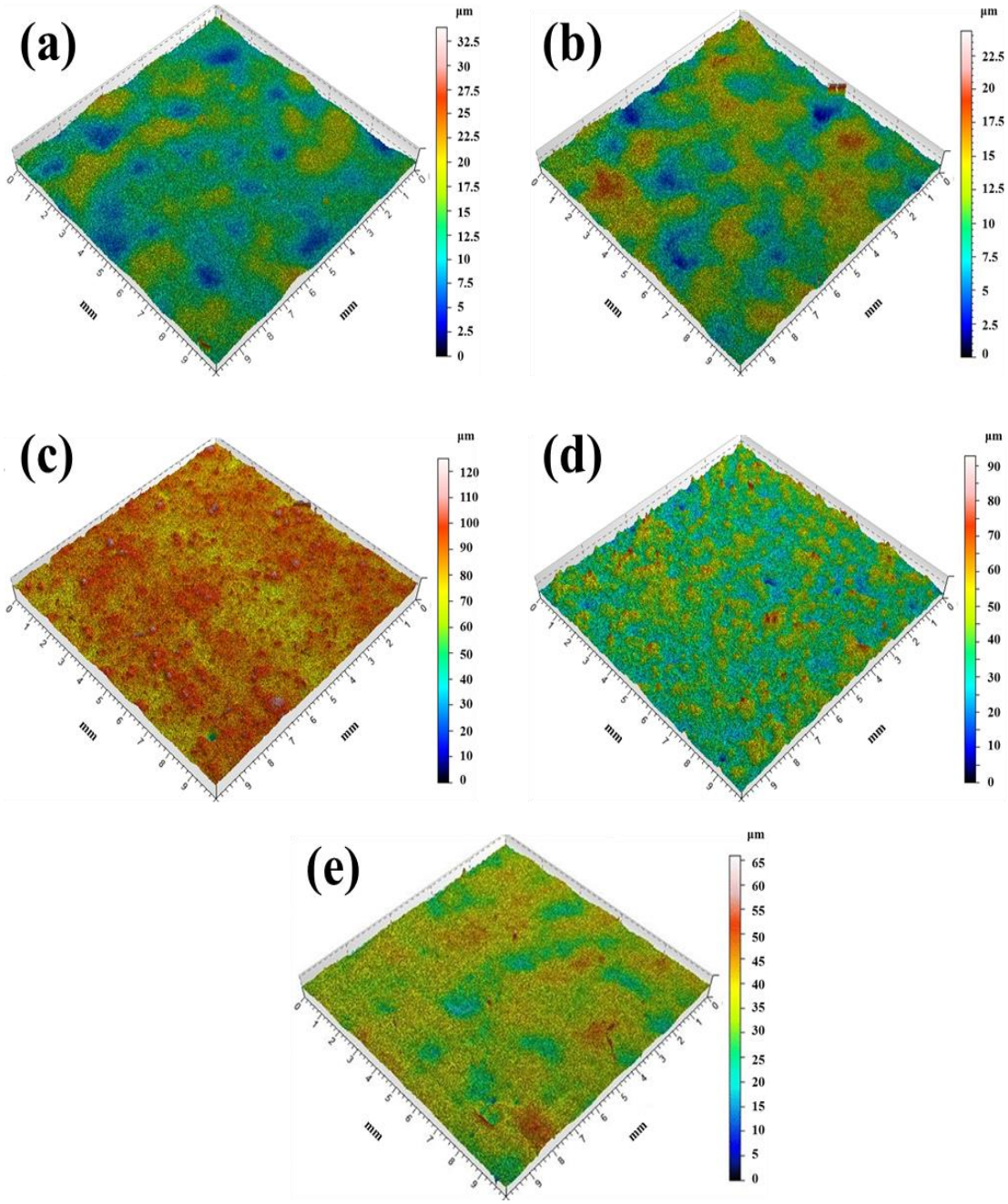

Figure 5.8. 3D surface roughness for PVC panels coated with (a) paint 1: pristine paint + 5 wt % QC18/Parm/MCM-48@400, (b) paint 2: pristine paint + 5 wt % QC14/Parm/MCM-48@400, (c) paint 3: pristine paint + 5 wt % QC18/MCM-48@400, (d) paint 4: pristine paint + 5 wt % QC14/MCM-48@400 and (e) pristine paint. The samples were measured with a 3D non-contact optical profiler (Talysurf CCI-HD), scanned area was 100 mm^2.

Table 5.2. Average roughnes values for PVC panels coated with the pristine paint, paint 1: pristine paint + 5 wt % QC18/Parm/MCM-48@400, paint 2: pristine paint + 5 wt % QC14/Parm/MCM-48@400, paint 3: pristine paint + 5 wt % QC18/MCM-48@400 and paint 4: pristine paint + 5 wt % QC14/MCM-48@400. The samples were measured with a 3D non-contact optical profiler (Talysurf CCI-HD), scanned area 100 was mm^2.

Sample	Scanned Area (mm^2)	Average Roughness, Sa (µm)
Pristine Paint	100	2.84
Paint 1	100	2.24
Paint 2	100	2.18
Paint 3	100	4.62
Paint 4	100	5.76

5.3.3. Contact angle measurements.

Figure 5.9 illustrates the contact angle values for the treated PVC panels and **Figure 5.10** shows contact angles of water droplets on the coated substrates. The pristine paint showed contact angle value of 84° which is within the hydrophobic region. However, the formulated paints 1-4 displayed contact angle values above 90°. The contact angles for the paints 1, 2, 3 and 4 were 96°, 94°, 106° and 104°, respectively. The addition of the modified nanoparticles affected the wettability properties of the pristine paint and the four nanocontainer-loaded paints exhibited higher hydrophobicity. The increased hydrophobicity of the formulated paints can be explained from the functionalisation of the NPs. Both QASs used for the surface modification and the biocide Parmetol S15 used for the encapsulation are highly hydrophobic compounds. Thus, the addition of the functionalised NPs increased the hydrophobicity of the paints. Another possible explanation of the increased contact

angle values for the formulated paints could be the increased surface roughness of the nanocontainer-doped paints, especially for paints 3 and 4. As we showed earlier, paints 3 and 4 exhibited higher values of surface roughness compared to the pristine paint and paints 1 and 2. It is well documented in the literature that surface roughness has a considerable influence on the contact angle.[30,31] The so-called Wenzel equation predicts that by introducing roughness to a surface will either increase the hydrophilicity or hydrophobicity of the sample, depending on whether the initial tested surface is hydrophilic or hydrophobic, respectively.[30,32] Characteristic example is the lotus leaf which is covered with a hydrophobic wax and in combination with the bumps on the leaf surface give a contact angle of 162°.[33] Furthermore, when a liquid droplet comes in contact with a rough surface, the liquid will form either a homogeneous interface with the solid surface or a composite interface with air pockets trapped between the solid surface and the liquid. In the case of the composite interface, the water droplet sits on patchwork of solid and air leading to a composite solid–liquid–air interface. The more air trapped in the interface, the higher the contact angle will be.[30,31]Therefore, the increased surface roughness of the paints 3 and 4 could lead to increased trapped air below the water droplet resulting in increased contact angle values.

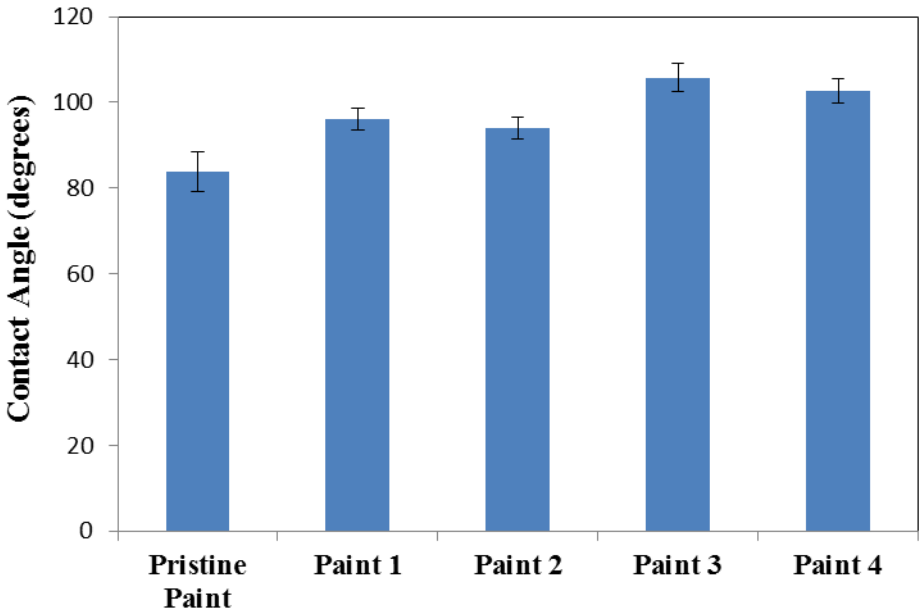

Figure 5.9. Contact angle values for PVC panels coated with the pristine paint, paint 1: pristine paint + 5 wt % QC18/Parm/MCM-48@400, paint 2: pristine paint + 5 wt % QC14/Parm/MCM-48@400, paint 3: pristine paint + 5 wt % QC18/MCM-48@400 and paint 4: pristine paint + 5 wt % QC14/MCM-48@400.

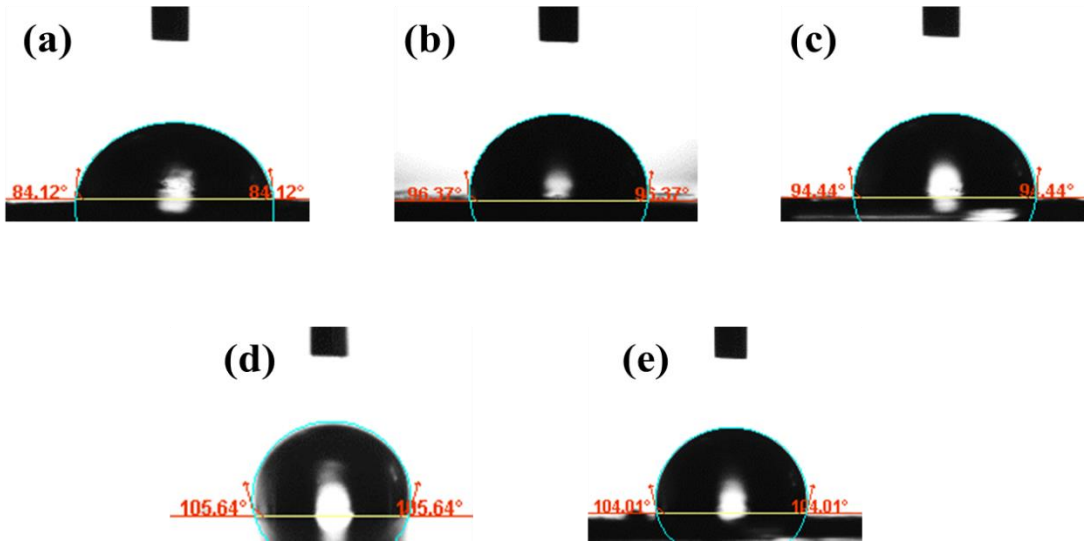

Figure 5.10. Contact angle images for water droplets on coated PVC panels with the (a) pristine paint, (b) paint 1: pristine paint + 5 wt % QC18/Parm/MCM-48@400, (c) paint 2: pristine paint + 5 wt % QC14/Parm/MCM-48@400, (d) paint 3: pristine paint + 5 wt % QC18/MCM-48@400 and (d) paint 4: pristine paint + 5 wt % QC14/MCM-48@400.

5.3.4. Antibacterial performance of PVC plates coated with the nanocontainer-doped paints.

For the evaluation of the antibacterial activity of the nanocontainer-doped paints, 50 mm x 50 mm PVC plates were coated with the pristine paint and paints 1-4 and tested against Gram-negative *Escherichia Coli* and Gram-positive *Staphylococcus Aureus* according to the ISO 22196:2011 protocol. The PVC panels coated with the pristine paint were used as control samples and the number of viable bacteria on these surfaces after 24 hours of incubation was defined as 100% growth. **Figure 5.11** illustrates the antibacterial properties of PVC panels coated with the paints 1-4 and the pristine paint against *E. coli* bacteria. Paint 3 (containing QC18-modified NPs) and paint 4 (containing QC14-modified NPs) reduced the number of viable bacteria by 86 and 79%, respectively, as compared to the pristine paint. Moreover, paint 1 and 2 (containing the QAS-modified NPs loaded with biocide) showed excellent antibacterial performance against *E. coli* by killing 99% of the exposed bacteria during the test. The results are in consistency with our previous studies on the antibacterial properties of the modified NPs with average size of 400 nm in powder form (chapter 4), where the QC18/MCM-48@400 exhibited better antibacterial performance than the QC14/MCM-48@400 and the dual functionalised NPs killed all of the bacteria at the end of the experiments. It is noteworthy to mention that the initial bacterial concentration that was applied on the surfaces coated with the pristine paint for the *E. coli* test was 10^5 CFU/ml but the 100% growth for the control sample (pristine paint) at the end of the experiment corresponded to 10^4 CFU/ml indicating also antibacterial activity of the pristine paint. This fact made more difficult to observe higher antibacterial properties of the paints 1-4 but even

under these conditions the paints 1 and 2 containing the NPs with the dual functionality showed significantly enhanced performance compared to paints 3 and 4 confirming their dual synergetic effect. Additionally, all of the paints including the control samples (coated with the pristine paint) killed all of the *S. aureus* bacteria at the end of the experiment indicating their high antibacterial properties. In this case, the antibacterial properties of the pristine paint made it difficult to observe any differences between the tested samples.

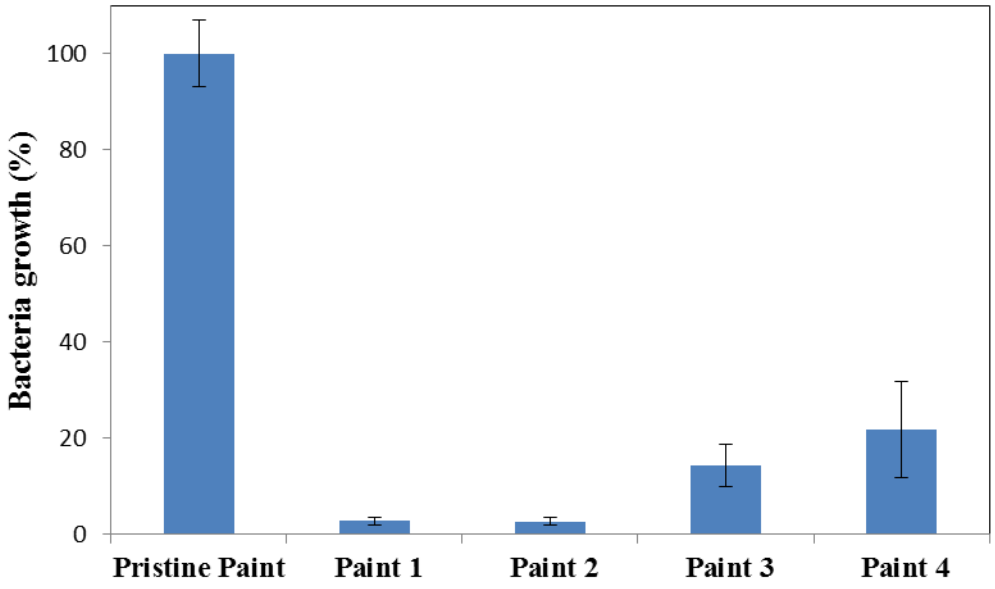

Figure 5.11. Bacteria growth (*E. coli*) after testing on PVC panels coated with the pristine paint, paint 1: pristine paint + 5 wt % QC18/Parm/MCM-48@400, paint 2: pristine paint + 5 wt % QC14/Parm/MCM-48@400, paint 3: pristine paint + 5 wt % QC18/MCM-48@400 and paint 4: pristine paint + 5 wt % QC14/MCM-48@400 by using the ISO 22196:2011 protocol.

5.3.5. Anti-macrofouling and toxicity assays for the nanocontainer-doped paints.

The percentage of attached mussels on the coated plates after 72 hours of exposure, related to the anti-macrofouling performance of the paints, is presented in **Figure 5.12** and **Figure 5.13** shows the average number of byssus threads (produced from the mussels in order to attach themselves to solid surfaces) at the attached mussels. About 50% of the mussels were attached on the plates coated with the pristine paint, whereas the paints 3 and 4 revealed a better anti-macrofouling effect yielding 33% attachment. On the other hand, paints 1 and 2 revealed the highest anti-macrofouling performance and completely inhibited the attachment of the mussels. The QAS-modified NPs (paint 3 and 4) increased the anti-macrofouling efficacy of the pristine paint indicating their antifouling properties. The dual functionalised NPs (paint 1 and 2) provided remarkably high anti-macrofouling properties to the pristine paint and all of the exposed mussels were not able to attach to the nanocontainer-doped coatings.

In the recovery test, the surviving mussels were transferred to new tissue culture plates with clean fresh water in order to test their adhesion and mortality similarly with the exposure test on coated tissue culture plates. Paints 3 and 4 containing the QAS-modified NPs showed similar recovery values with the pristine paint while paints 1 and 2 containing the dual functionalised NPs exhibited higher recovery values, especially for paint 2 where all of the mussels were able to settle. Therefore, we can assume that the added NPs in the paint have non-toxic effect against the mussels (since the mussels were able to produce byssus threads normally and use

them to attach themselves to the new tissue culture plates) and, at the same time, they prevent mussels' attachment.

Furthermore, the fact that 50 to 100% of the mussels were able to recover immediately after media replenishment implying that the toxicity of the paints did not cause any irreversible damage to the test organisms. The paints consist of several chemical compounds which can be released during the test. Therefore, the mussels close their shells with increasing concentration of these active compounds as a self-defence mechanism to isolate their tissues from the environment.[34]

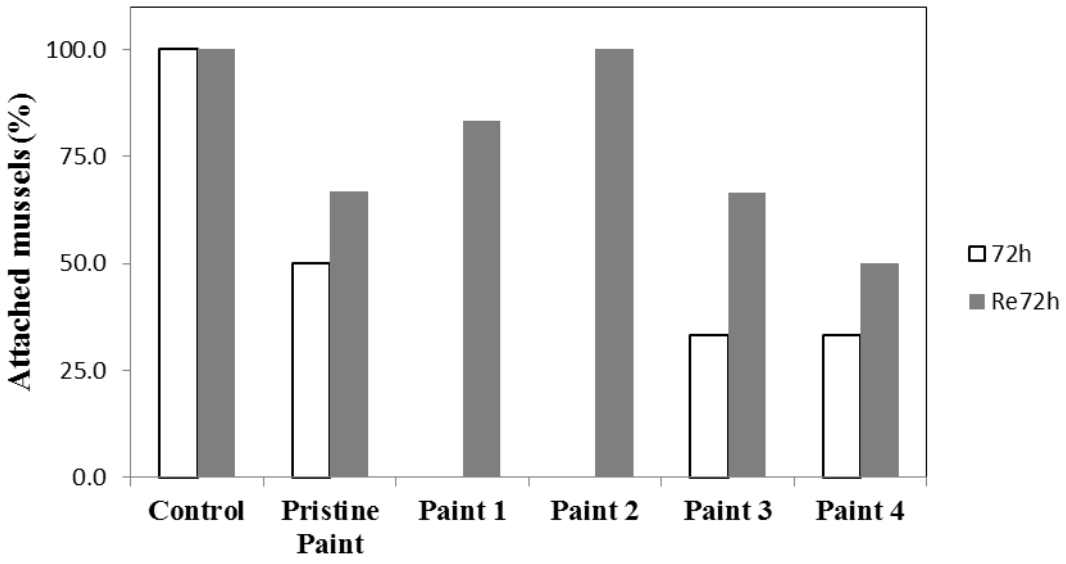

Figure 5.12. Efficacy anti-macrofouling assays of pristine paint, paint 1: pristine paint + 5 wt % QC18/Parm/MCM-48@400, paint 2: pristine paint + 5 wt % QC14/Parm/MCM-48@400, paint 3: pristine paint + 5 wt % QC18/MCM-48@400 and paint 4: pristine paint + 5 wt % QC14/MCM-48@400 tested against the Red Sea *Brachidontes pharaonis* mussels: number of settled mussels. Blank bars indicate results after 72 hours of exposure to treated plates and grey bars after 72 hours in recovery assay.

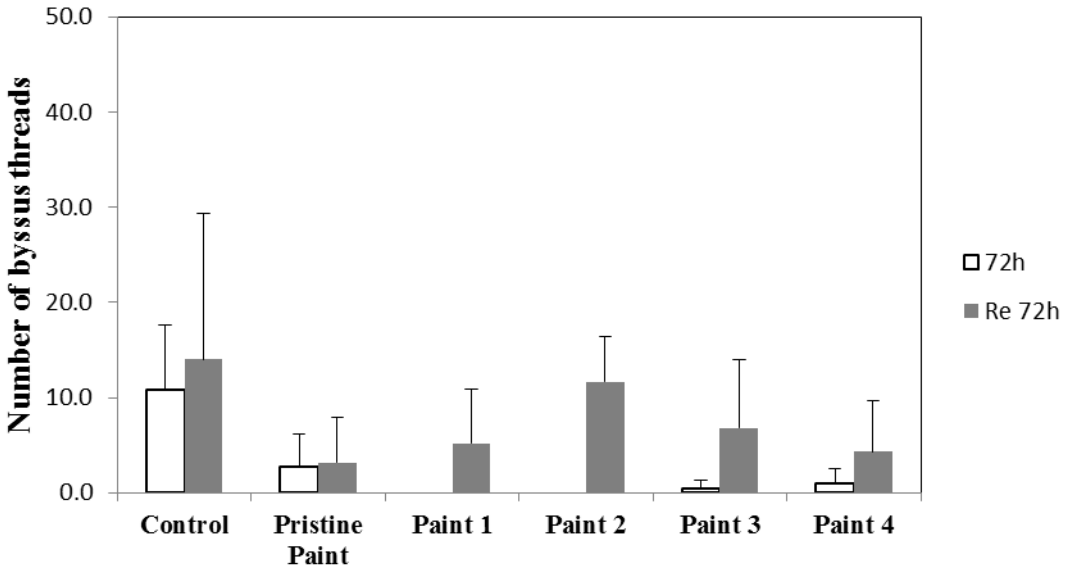

Figure 5.13. Efficacy of anti-macrofouling assays of pristine paint, paint 1: pristine paint + 5 wt % QC18/Parm/MCM-48@400, paint 2: pristine paint + 5 wt % QC14/Parm/MCM-48@400, paint 3: pristine paint + 5 wt % QC18/MCM-48@400 and paint 4: pristine paint + 5 wt % QC14/MCM-48@400 tested against the *Brachidontes pharaonis* mussels: average number of byssus threads following square root transformation in settled mussels. Blank bars indicate results after 72 hours of exposure to treated plates and grey bars after 72 hours in recovery assay.

Further information for the toxicity of the paints was obtained by a brine shrimp toxicity assay (**Figure 5.14**). The *A. salina* toxicity assay indicated that paints 1, 3 and 4 caused lower mortality than the pristine paint (control). Only paint 2 exhibited slightly higher toxicity than the pristine paint. In chapter 3, we demonstrated that the amount of the encapsulated biocide in the QC14-modified NPs (nanocontainers of paint 2) is slightly higher compared to the encapsulated biocide in the QC18-modified NPs (nanocontainers of paint 1). *A. salina* is filter-feeder and can readily ingest small chemical compounds, even fine particles smaller than 50 μm.[35] Therefore, the higher concentration of biocide in the paint 2 could explain its higher

toxicity in comparison with the paint 1. However, if we take into consideration the statistical errors, we can imply that the toxicity of paints 1-4 fall within the toxicity range of the pristine paint, hence, there is not significant increase in the toxicity of the paints against brine shrimp nauplii by the addition of the four different types of modified nanoparticles, especially for the paints 1, 3 and 4.

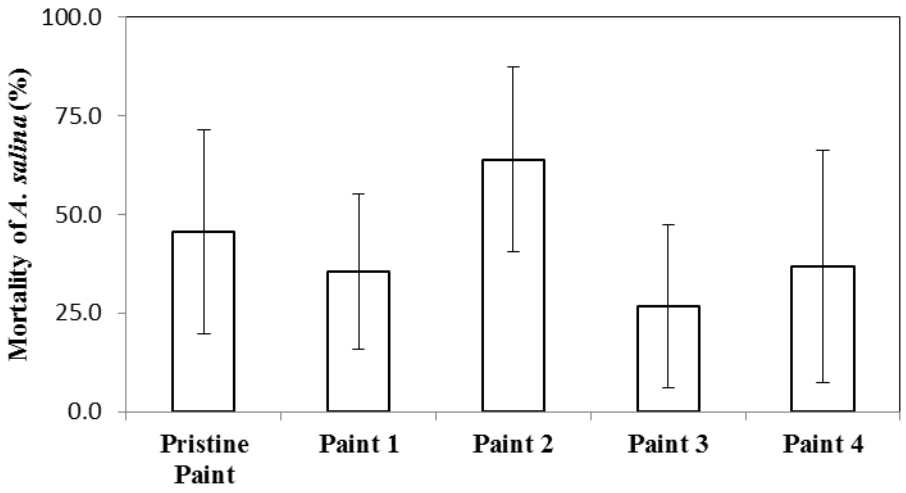

Figure 5.14. Toxicity assays of pristine paint, paint 1: pristine paint + 5 wt % QC18/Parm/MCM-48@400, paint 2: pristine paint + 5 wt % QC14/Parm/MCM-48@400, paint 3: pristine paint + 5 wt % QC18/MCM-48@400 and paint 4: pristine paint + 5 wt % QC14/MCM-48@400 tested on *Artemia salina* nauplii.

5.3.6. Antifouling performance of coated PVC panels with the nanocontainer-doped paints.

In order to evaluate the antifouling performance of the nanocontainer-loaded paints, we carried out a field test trial in northern Red Sea, Eilat, Israel. The concentration of

the nanoparticles in the paints was adjusted to either 2 or 5 wt % and four different paint formulations with two concentrations of active nanocontainers were prepared. Paint 1: pristine paint + 2 or 5 wt % QC18/Parm/MCM-48@400, Paint 2: pristine paint + 2 or 5 wt % QC14/Parm/MCM-48@400, Paint 3: pristine paint + 2 or 5 wt % QC18/MCM-48@400 and Paint 4: pristine paint + 2 or 5 wt % QC14/MCM-48@400. Through this field test, a more realistic assessment for the antifouling performance of the formulated paints was achieved. The coated PVC panels were stayed immersed in natural sea water for six months and we obtained valuable results for the antifouling properties of the nanocontainer-doped paints.

Underwater photographs of the exposed PVC panels coated with the pristine paint and paints 1-4 containing 5 wt % of modified nanoparticles in the first day of immersion and after 6 months of exposure in Red Sea are presented in **Figure 5.15**. **Figure 5.16** shows the biofouling coverage for each month of exposure during the six months field test trial. The biofouling coverage on the surface of the control sample coated with the pristine paint was 49% at the end point of this field test. The biofouling coverage of the panels with four nanocontainer-doped paints (5 wt % concentration of modified nanoparticles) was significantly lower, below 10%. Paints 3 and 4 containing the QAS-modified nanoparticles presented 8.6 and 10% of biofouling coverage, respectively. Paints 1 and 2 containing the modified nanoparticles with the dual functionality showed enhanced performance, 6.9 and 8% of biofouling coverage, respectively. Even after the release of the encapsulated biocide, the covalently attached QAS groups on the surface of the nanoparticles continue to provide antifouling properties to the coating formulations prolonging their lifetime antifouling performance.

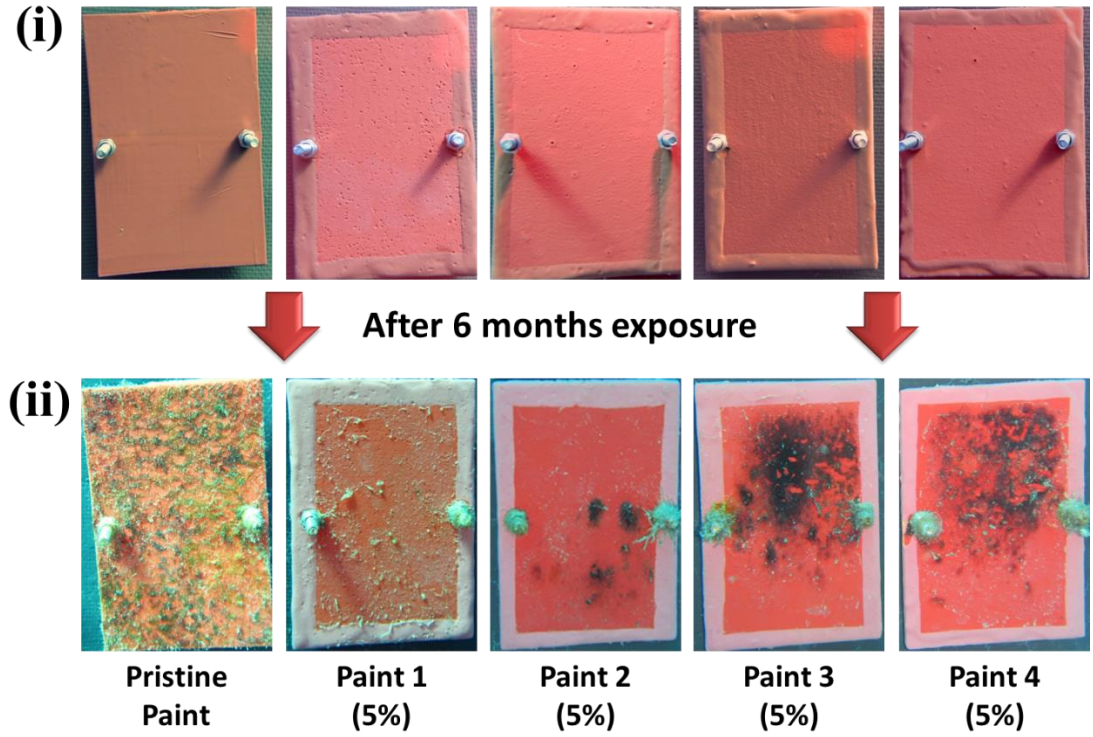

Figure 5.15. Underwater photographs of PVC panels during the field test trial (Eilat, northern Red Sea) for the first day of deployment (i) and after 6 months of exposure (ii). The PVC panels are coated with five different paints: pristine paint, paint 1: pristine paint + 5 wt % QC18/Parm/MCM-48@400, paint 2: pristine paint + 5 wt % QC14/Parm/MCM-48@400, paint 3: pristine paint + 5 wt % QC18/MCM-48@400 and paint 4: pristine paint + 5 wt % QC14/MCM-48@400.

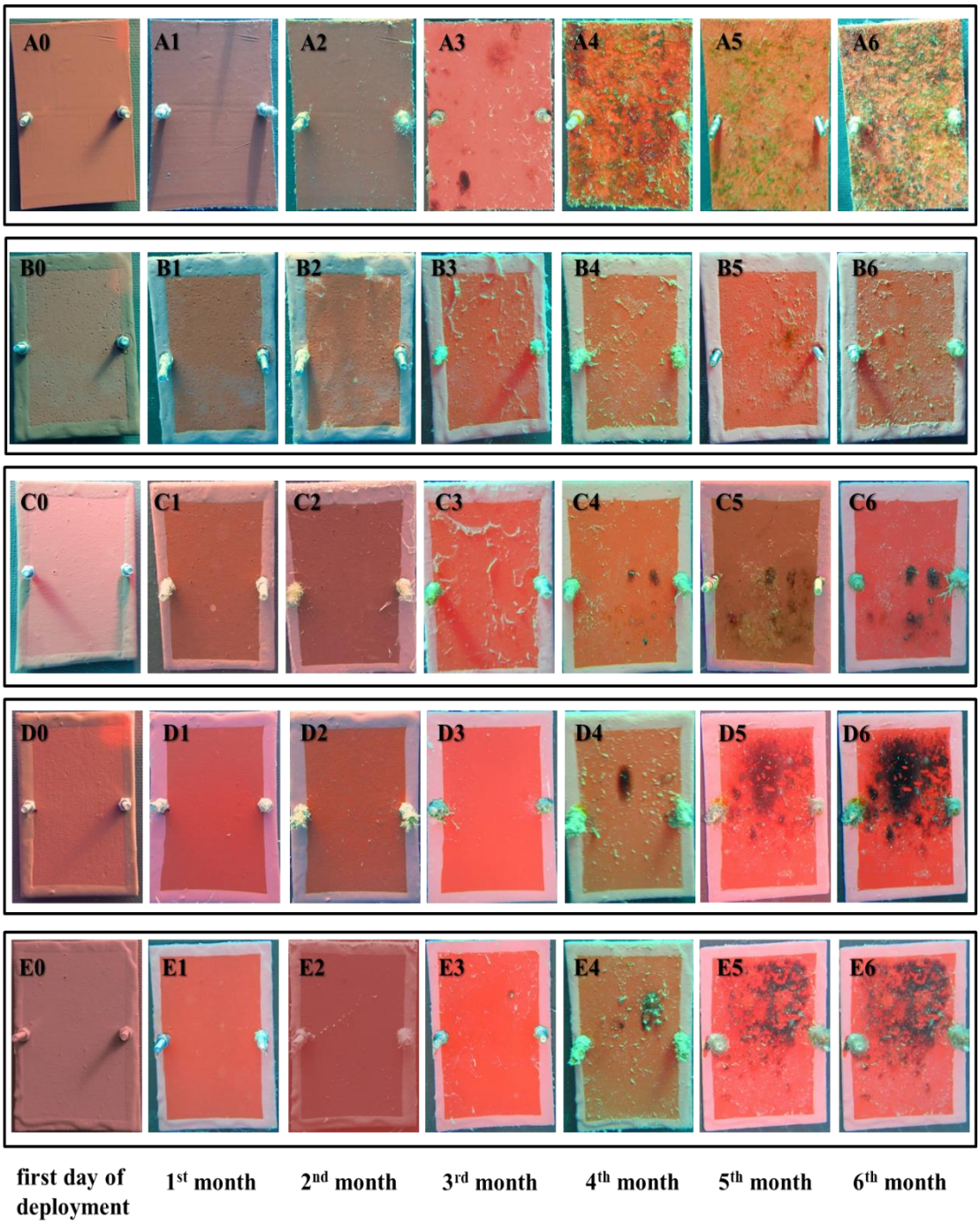

Figure 5.16. Underwater photographs of PVC panels during the field test trial (Eilat, northern Red Sea) for the first day of deployment and every month of exposure during the six months period. The PVC panels are coated with the pristine paint and modified paints 2, 3 and 4 containing 5 wt % nanoparticles: (A) pristine paint, (B) paint 1: pristine paint + 5 wt % QC18-modified MCM-48 loaded with Parmetol S15 (C) paint 2: pristine paint + 5 wt % QC14-modified MCM-48 loaded with Parmetol S15, (D) paint 3: pristine paint + 5 wt % QC18-modified MCM-48 and (E) paint 4: pristine paint + 5 wt % QC14-modified MCM-48.

Figure 5.17 presents photographs of exposed PVC panels coated with the pristine paint and paints 1-4 containing 2 wt % modified nanoparticles in the first day of deployment and after 6 months of exposure in Red Sea. **Figure 5.18** shows the biofouling coverage for each month of exposure during the six months field test trial. Even after decreasing the concentration of the nanoparticles in the coating formulations from 5 to 2 wt %, the paints 1-4 continued showing notably lower biofouling coverage compared to the pristine paint at the end of the 6 months field test trial. In particular, the biofouling coverage after six months of exposure in the Red Sea for the pristine paint was 49%, whereas the paints 1, 2, 3 and 4 presented 7.5%, 13.9%, 10.5% and 17.4% of biofouling coverage, respectively.

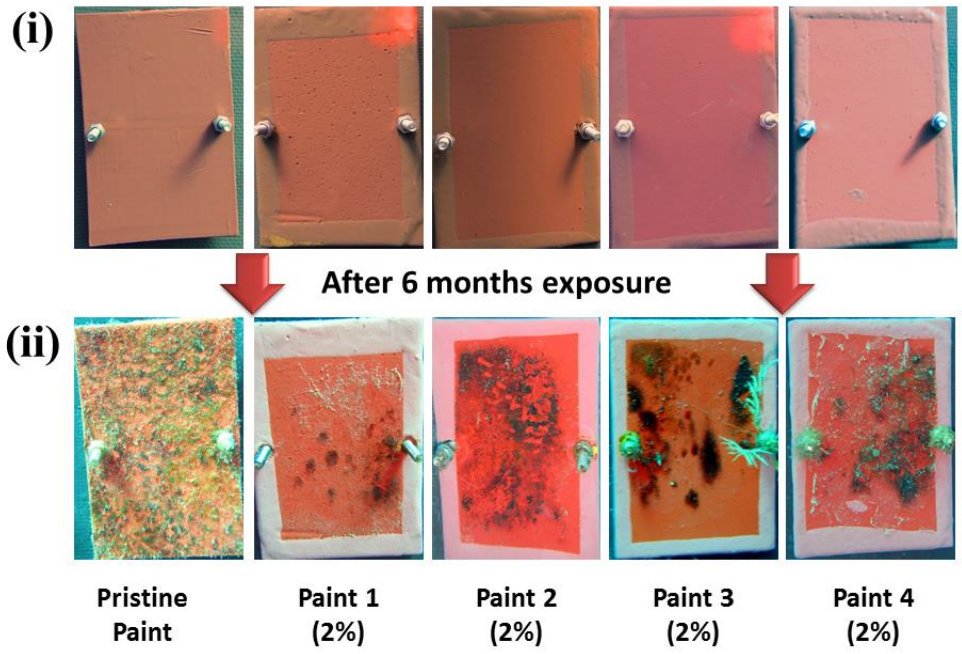

Figure 5.17. Underwater photographs of PVC panels during the field test trial (Eilat, northern Red Sea) for the first day of deployment (i) and after 6 months of exposure (ii). The PVC panels are coated with five different paints: pristine paint, paint 1: pristine paint + 2 wt % QC18/Parm/MCM-48@400, paint 2: pristine paint + 2 wt % QC14/Parm/MCM-48@400, paint 3: pristine paint + 2 wt % QC18/MCM-48@400 and paint 4: pristine paint + 2 wt % QC14/MCM-48@400.

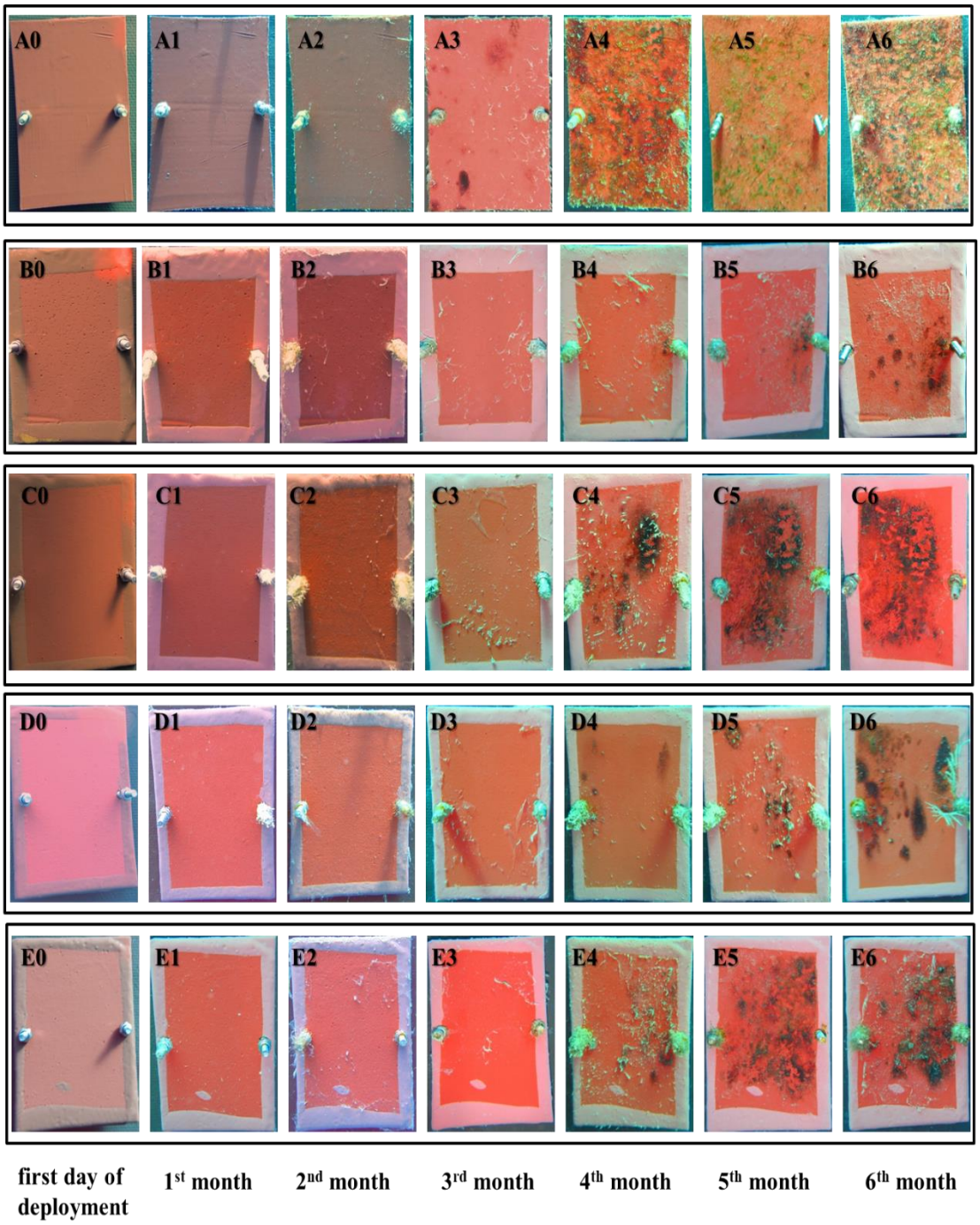

Figure 5.18. Underwater photographs of PVC panels during the field test trial (Eilat, northern Red Sea) for the first day of deployment and every month of exposure during the six months period. The PVC panels are coated with the pristine paint and modified paints 2, 3 and 4 containing 2 wt % nanoparticles: (A) pristine paint, (B) paint 1: pristine paint + 2 wt % QC18-modified MCM-48 loaded with Parmetol S15 (C) paint 2: pristine paint + 2 wt % QC14-modified MCM-48 loaded with Parmetol S15, (D) paint 3: pristine paint + 2 wt % QC18-modified MCM-48 and (E) paint 4: pristine paint + 2 wt % QC14-modified MCM-48.

At the end of the field test, the biofouling coverage on the surfaces of the coated PVC panels with 2 wt % NPs concentration is consistent with the biofouling coverage on the surfaces of the coated PVC panels with 5 wt % concentration. Similarly, paints 1 and 2 containing the QAS-modified nanoparticles with the additional encapsulated biocide exhibited higher antifouling properties compared to paints 3 and 4 containing the counterpart NPs with the single functionalisation. However, the antifouling performance of the paints 1-4 has been decreased by reducing the amount of the incorporated NPs from 5 to 2 wt %.

Furthermore, the antifouling performance of paint 1 compared to paint 2 and of paint 3 compared to paint 4 was higher using either 2 or 5 wt % modified NPs. Paints 1 and 3 contain NPs that are surface modified with the quaternary ammonium salt QC18, whereas the NPs for paints 2 and 4 are surface modified with QC14. The main difference between them is that the QC18 has 18 carbons alkyl chain length while the QC14 has 14 carbons alkyl chain length. Additionally, during the surface modification of the MCM-48 with QC14 (as we discussed in chapter 4), the available hydroxyl groups on the MCM-48 surface can react both with the 3-chloropropyltriethoxy silane and the QC14. As a result, the surface of the QC14/MCM-48@400 was covered with QC14 molecules and 3-chloropropyltriethoxy silane molecules. Therefore, we can assume that the lower amount of QASs groups on the surface of the QC14/MCM-48@400 compared to the QC18/MCM-48@400 provided strong influence to the antifouling properties of the paints and undermined the antifouling efficacy for the paint 4, especially for lower concentration in the coating formulations.

Figure 5.19 illustrates the visual appearance of PVC panels coated with the pristine paint and the two paints with the best performance (paint 1 containing 2 and 5 wt % QC18-modified NPs loaded with biocide) for the first day of deployment and every month of exposure during the 6 months field test trial. During the first three months of exposure, the control coating and the two experimental coatings showed qualitatively similar accumulation of biofouling. After longer exposure duration, the effect of the incorporated dual functionalised NPs in the paints can be observed more clearly. In particular, between the fourth and sixth month of exposure in the Red Sea, the biofouling accumulation for the pristine paint increased significantly as compared to the two nanocontainer-loaded paints and reached 49% coverage (**Figure 5.19**, A4-A6 panels). On the other hand, the biofouling accumulation for the paint 1 containing 2 and 5 wt % dual functionalised NPs increased slowly and after 6 months of exposure the coverage was 6.9% for the paint 1 with 5% concentration (**Figure 5.19**, B6 panel) and 7.5% for the paint 1 with 2% concentration (**Figure 5.19**, C6 panel).

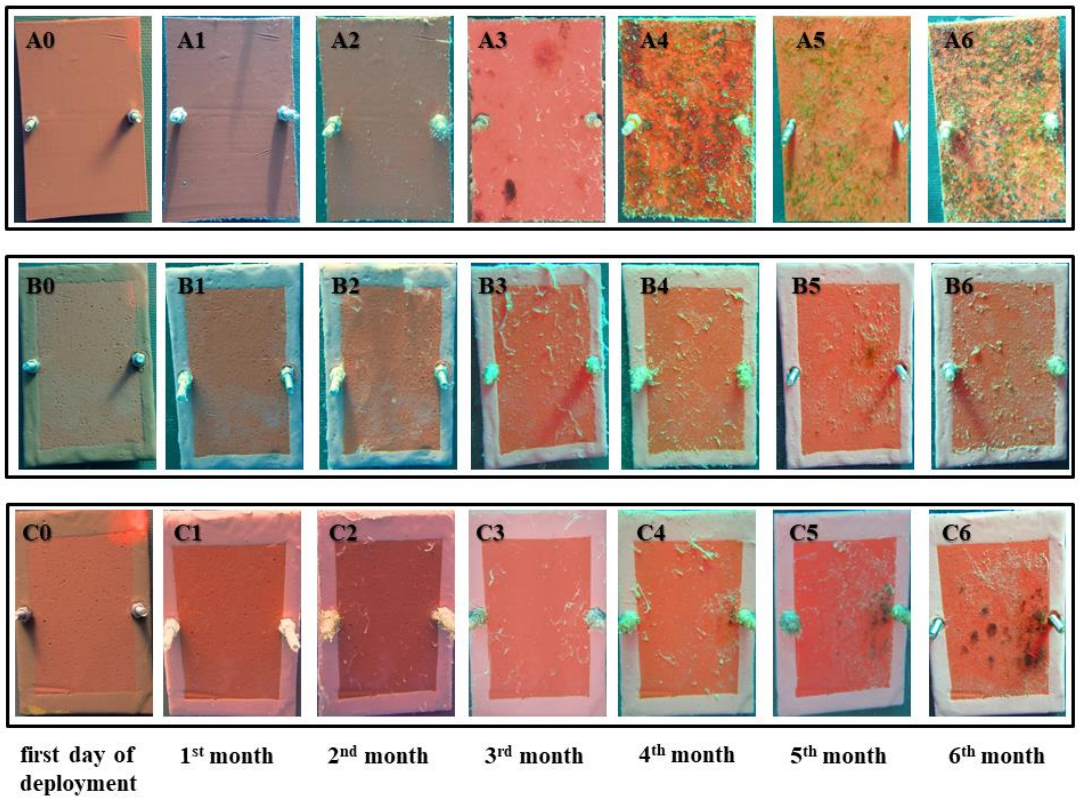

Figure 5.19. Underwater photographs of PVC panels during the field test trial (Eilat, northern Red Sea) for the first day of deployment and every month of exposure during the six months period. The PVC panels are coated with the pristine paint and the two modified paints with the best performance: (A) pristine paint, (B) paint 1: pristine paint + 5 wt % QC18-modified MCM-48 loaded with Parmetol S15 and (C) paint 1: pristine paint + 2 wt % QC18-modified MCM-48 loaded with Parmetol S15.

References

[1] A. G. Nurioglu, A. C. C. Esteves, G. de With, *J. Mater. Chem. B* **2015**, *3*, 6547.

[2] B. R. Knowles, P. Wagner, S. Maclaughlin, M. J. Higgins, P. J. Molino, *ACS Appl. Mater. Interfaces* **2017**, *9*, 18584.

[3] M. Lejars, A. Margaillan, C. Bressy, *Chem. Rev.* **2012**, *112*, 4347.

[4] M. Andersson Trojer, L. Nordstierna, J. Bergek, H. Blanck, K. Holmberg, M. Nydén, *Adv. Colloid Interface Sci.* **2015**, *222*, 18.

[5] D. Borisova, H. Möhwald, D. G. Shchukin, *ACS Nano* **2011**, *5*, 1939.

[6] M. Graham, J. A. Coca-Clemente, E. Shchukina, D. Shchukin, *J. Mater. Chem. A* **2017**, *5*, 13683.

[7] H. Gao, O. A. Goriacheva, N. V. Tarakina, G. B. Sukhorukov, *ACS Appl. Mater. Interfaces* **2016**, *8*, 9651.

[8] Z. Zheng, Z. Chang, G.-K. Xu, F. McBride, A. Ho, Z. Zhuola, M. Michailidis, W. Li, R. Raval, R. Akhtar, D. Shchukin, *ACS Nano* **2017**, *11*, 721.

[9] H. Gao, D. Wen, G. B. Sukhorukov, *J. Mater. Chem. B* **2015**, *3*, 1888.

[10] D. V. Andreeva, D. Fix, H. Möhwald, D. G. Shchukin, *J. Mater. Chem.* **2008**, *18*, 1738.

[11] G. Sørensen, A. L. Nielsen, M. M. Pedersen, S. Poulsen, H. Nissen, M. Poulsen, S. D. Nygaard, *Prog. Org. Coatings* **2010**, *68*, 299.

[12] M. Yang, L. Gu, B. Yang, L. Wang, Z. Sun, J. Zheng, J. Zhang, J. Hou, C. Lin, *Appl. Surf. Sci. jou* **2017**, *426*, 185.

[13] F. Maia, A. P. Silva, S. Fernandes, A. Cunha, A. Almeida, J. Tedim, M. L. Zheludkevich, M. G. S. Ferreira, *Chem. Eng. J.* **2015**, *270*, 150.

[14] S. V. Lamaka, D. G. Shchukin, D. V. Andreeva, M. L. Zheludkevich, H.

Möhwald, M. G. S. Ferreira, *Adv. Funct. Mater.* **2008**, *18*, 3137.

[15] M. S. Selim, M. A. Shenashen, S. A. El-Safty, S. A. Higazy, M. M. Selim, H. Isago, A. Elmarakbi, *Prog. Mater. Sci.* **2017**, *87*, 1.

[16] M. Wouters, C. Rentrop, P. Willemsen, *Prog. Org. Coatings* **2010**, *68*, 4.

[17] S. Mallakpour, E. Khadem, *Prog. Polym. Sci.* **2015**, *51*, 74.

[18] Y. Lvov, E. Abdullayev, *Prog. Polym. Sci.* **2013**, *38*, 1690.

[19] J. H. Jhaveri, Z. V. P. Murthy, *Desalination* **2016**, *379*, 137.

[20] Q. Li, S. Mahendra, D. Y. Lyon, L. Brunet, M. V. Liga, D. Li, P. J. J. Alvarez, *Water Res.* **2008**, *42*, 4591.

[21] M. J. Hajipour, K. M. Fromm, A. Akbar Ashkarran, D. Jimenez de Aberasturi, I. R. de Larramendi, T. Rojo, V. Serpooshan, W. J. Parak, M. Mahmoudi, *Trends Biotechnol.* **2012**, *30*, 499.

[22] M. Michailidis, I. Sorzabal-Bellido, E. A. Adamidou, Y. A. Diaz-Fernandez, J. Aveyard, R. Wengier, D. Grigoriev, R. Raval, Y. Benayahu, R. A. D'Sa, D. Shchukin, *ACS Appl. Mater. Interfaces* **2017**, *9*, 38364.

[23] M. Tischer, G. Pradel, K. Ohlsen, U. Holzgrabe, *ChemMedChem* **2012**, *7*, 22.

[24] Y. Xue, H. Xiao, Y. Zhang, *Int. J. Mol. Sci.* **2015**, *16*, 3626.

[25] *International Organization for Standardization. Measurement of Antibacterial Activity on Plastics and Other Non-Porous Surfaces. ISO 22196:2011*, **n.d.**

[26] E. Gutner-Hoch, R. Martins, T. Oliveira, F. Maia, A. Soares, S. Loureiro, C. Piller, I. Preiss, M. Weis, S. Larroze, T. Teixeira, J. Tedim, Y. Benayahu, *J. Mar. Sci. Eng.* **2018**, *6*, 6.

[27] J. D. Solis, P. N., Wright, C. W., Anderson, M. M., Gupta, M. P., & Phillipson, *Planta Med.* **1993**, *59*, 250.

[28] B. S. Nunes, F. D. Carvalho, L. M. Guilhermino, G. Van Stappen, *Environ.*

Pollut. **2006**, *144*, 453.

[29] C. A. Schneider, W. S. Rasband, K. W. Eliceiri, *Nat. Methods* **2012**, *9*, 671.

[30] Y. C. Jung, B. Bhushan, *Nanotechnology* **2006**, *17*, 4970.

[31] D. Quéré, *Phys. A Stat. Mech. its Appl.* **2002**, *313*, 32.

[32] R. N. Wenzel, *Ind. Eng. Chem.* **1936**, *28*, 988.

[33] C. NEINHUIS, *Ann. Bot.* **1997**, *79*, 667.

[34] V. Wilsanand, A. B. Wagh, M. Bapuji, *Indian J. Mar. Sci.* **1999**, *28*, 280.

[35] M. Ates, J. Daniels, Z. Arslan, I. O. Farah, *Environ. Monit. Assess.* **2013**, *185*, 3339.

Chapter 6: Conclusions

6.1. Conclusions Chapter 3

The aim of this part of the thesis is to develop spherical MCM-48 mesoporous silica nanoparticles (MSNs) as potential carriers of antibacterial and antifouling compounds. For that reason, we synthesised and characterised MCM-48 MSNs with two different average sizes and morphological properties by using two different experimental procedures.

According to the first experimental procedure, spherical MCM-48 particles with average size of 400 nm were developed. As revealed from the XRD studies, the synthesised material showed highly ordered mesostructure which can be assigned to the typical cubic space group *Ia3d*, characteristic for mesoporous materials with 3D cubic structure. From the N_2 isotherms, the samples showed high BET surface area (1180-1300 m^2/g), high pore volume (0.8 cm^3/g) and narrow pore size distribution with average pore diameter at 3.2 nm. The scanning electron microscopy (SEM) and the transmission electron microscopy (TEM) were used to evaluate the morphological properties of the samples. The samples showed spherical morphology in the range of 200-600 nm and some of the nanoparticles were aggregated and fused together. Furthermore, a regular well-ordered mesopores arrangement was observed over the whole particle surface. In addition, the diffuse reflectance infrared Fourier transform (DRIFT) spectroscopy and the thermogravimetric analysis (TGA) revealed that the surfactant was removed successfully during the calcination process and the synthesised samples have high thermal stability up to 800 ^oC.

From the second experimental procedure, monodispersed spherical MCM-48 with average size of 120 nm were developed. The XRD analysis showed that the synthesised material has highly ordered 3D cubic mesostructure which was assigned to the *Ia3d* cubic space group, typical for MCM-48 MSNs. From the interpretation of the N_2 isotherms, the synthesised samples showed high BET surface area (1050-1120 m^2/g), high pore volume (1.27 cm^3/g) and narrow pore size distribution with average pore diameter at 3.5 nm. For the morphological studies, the SEM images showed that the nanoparticles have spherical shape with no aggregation in the range of 90-170 nm with average size at 120 nm. The scanning transmission electron microscopy (STEM) images confirmed the spherical monodispersity of the nanoparticles as well as a regular well-ordered mesostructure extended over the whole particle. The TGA and the DRIFT analysis showed that the final material after calcination at 550 ^oC was template-free and the binary system of surfactants was removed completely.

The two different experimental procedures resulted in spherical MCM-48 MSNs with excellent morphological and structural properties. The high loading capacity for both materials and their size of pores makes them excellent candidates for loading and releasing of active molecules with antibacterial/antifouling properties. Furthermore, their high surface area and existence of free –OH groups on their surface are great characteristics for further surface modification. More details regarding these characteristics are discussed in Chapter 4.

6.2. Conclusions Chapter 4

In this chapter, functional fillers for antibacterial/antifouling coatings with advanced performance were developed, characterised and tested against bacteria. For that purpose, spherical MCM-48 MSNs with average size of 400 nm (MCM-48@400) were modified with quaternary ammonium salts {either dimethyloctadecyl [3-(trimethoxysilyl) propyl] ammonium chloride (QC18) or dimethyltetradecyl [3-(triethoxysilyl) propyl] ammonium chloride (QC14)} revealing strong covalent bonds between the QASs and the surface of the nanoparticles. The surface functionalisation was confirmed by DRIFT, TGA, elemental analysis and ζ-potential measurements. The DRIFT spectra for the QC18/MCM-48@400 and QC14/MCM-48@400 showed 3 additional peaks confirming the presence of C-H bonds due to the attached QASs on the MCM-48@400 surface. The TGA curves showed 19-28 wt % further weight loss for the modified MCM-48@400 due to the QASs calcination. The ζ-potential values for the QC18/MCM-48@400 and QC14/MCM-48@400 presented significant change from negative to positive values after the modification of the negatively charged silica with positively charged quaternary ammonium groups. The elemental analysis provided further evidence for the successful surface modification from the significant increment of carbon, hydrogen and nitrogen at the modified materials.

In order to achieve dual synergetic effect, the QAS modified MCM-48@400 were loaded with one additional biocide for an enhanced dual antibacterial/antifouling effect. The encapsulation of the biocide Parmetol S15 was confirmed by the TGA curves where the QC18/Parm/MCM-48@400 and QC14/Parm/MCM-48@400

presented 31.5% wt. and 26.9% wt. of weight loss, respectively, compared to the QC18/MCM-48@400 and QC14/MCM-48@400, respectively. In the antibacterial tests, all of the synthesised modified nanoparticles exhibited high antibacterial performance confirming their dual activity. In the case of the dual functionalised QC18/Parm/MCM-48@400 and QC14/Parm/MCM-48@400, all the exposed bacteria were dead at the end of the experiments for both antibacterial tests against Gram-negative and Gram-positive bacteria. Furthermore, the single functionalised QC18/MCM-48@400 and QC14/MCM-48@400 presented 77-89% reduction against Gram-negative bacteria and 78-94% reduction against Gram-positive bacteria.

Furthermore, spherical MCM-48 with smaller average size of 120 nm (MCM-48@120) were surface modified with the two types of QASs and tested against Gram-negative and Gram-positive bacteria in order to investigate if there is size-dependency at the antibacterial properties of silica-QAS core-shell NPs. The synthesised materials (QC18/MCM-48@120 and QC14/MCM-48@120) were characterised by DRIFT, TGA, elemental analysis and ζ-potential measurements. The results from the characterisation techniques were similar with their counterparts with average size of 400 nm. Both QC18/MCM-48@120 and QC14/MCM-48@120 showed three additional peaks at the DRIFT spectra due to the presence of C-H bonds from the attached QASs on the MCM-48@120 surface. The TGA curves showed 18-27 wt % further weight loss for the modified MCM-48@120 due to the QASs calcination. The ζ-potential values for the QC18/MCM-48@120 and QC14/MCM-48@120 shifted significantly from negative to positive values after the modification of the negatively charged silica with positively charged quaternary

ammonium groups. At the elemental analysis, the modified materials exhibited significant increment of carbon, hydrogen and nitrogen compared to pristine MCM048@120.

In the antibacterial tests, the QC18/MCM-48@120 and QC14/MCM-48@120 presented 83-94% reduction against Gram-negative bacteria and 87-97% reduction against Gram-positive bacteria, respectively. Both of the modified NPs with average size of 120 nm showed increased antibacterial properties compared to their counterparts with average size of 400 nm. Specifically, the QC18/MCM-48@400 and QC14/MCM-48@400 presented 77-89% reduction against Gram-negative bacteria and 78-94% reduction against Gram-positive bacteria, respectively. These results implying that there is size-dependency at the antibacterial properties and possibly smaller size of modified NPs could provide better antibacterial properties. Probably because the smaller antibacterial agents have enlarged surface area compared to larger antibacterial agents, leading to enhanced antibacterial performance based on the same amount.

6.3. Conclusions Chapter 5

Four different types of modified mesoporous silica nanoparticles: (i) QC18/Parm/MCM-48@400, (ii) QC14/Parm/MCM-48@400, (iii) QC18/MCM-48@400 and (iv) QC14/MCM-48@400 were used as functional fillers for antibacterial/antifouling coating formulations. The functionalised nanoparticles were homogeneously dispersed in the paints as shown from the cross-sectional images of the paints. Afterwards, PVC plates were coated with the nanocontainer-doped paints and their surface properties were tested. The addition of the nanoparticles in the paints increased the average roughness of the treated PVC panels. Furthermore, all of the nanocontainer-treated paints revealed increased hydrophobicity compared to the pristine paint and the contact angle values were between 94 and 106° comparing to 84° of the pristine paint.

50 mm x 50 mm PVC plates were coated with the nanocontainer-doped paints and tested against two types of bacteria (*E. coli* and *S. aureus*). Paints 1 and 2 containing the dual functionalised nanoparticles (QAS-modified and loaded with Parmetol S15) demonstrated excellent antibacterial properties against *E. coli* resulting in 99% reduction of viable bacteria compared to the pristine paint while paints 3 and 4 containing the single functionalised nanoparticles (QAS-modified) showed 86 and 79% reduction, respectively. In the case of the antibacterial tests against *S. aureus*, all of the paints revealed high antibacterial efficiency by killing all the exposed bacteria at the end of the test (after 16 hours of exposure). Moreover, the incorporation of the modified nanoparticles in the paints increased their anti-macrofouling properties. Paints 1 and 2 inhibited 100% of the mussels' attachment

whereas 33% of the mussels attached to paints 3 and 4 and 50% to the pristine paint (after 72 hours of exposure). In the mussels' recovery tests, the modified paints presented similar or higher recovery as compared to the control sample confirming that the addition of the modified nanoparticles to the pristine paint has non-toxic effect against the mussels. The nanocontainer-doped paints presented toxicity similar to the pristine paint against *A. salina* brine shrimps (model organism for toxicity tests) confirming that the modified nanoparticles are non-toxic against them.

The antifouling properties of the modified paints were evaluated by a six-month field test trial in Red Sea. The concentration of the modified nanoparticles in the coating formulations was adjusted to either 2 or 5 wt %. The biofouling coverage after six months of exposure in the Red Sea was 49% for the pristine paint. On the contrary, all of the panels treated with the four nanocontainer-doped paints presented considerably lower biofouling coverage for both concentrations (either 2 or 5 wt %) and the dual functionality of paints 1 and 2 was confirmed. In particular, paints 1, 2, 3 and 4 presented 6.9%, 8%, 8.6% and 10% biofouling coverage, respectively, when 5% of nanoparticles were used and 7.5%, 13.9%, 10.5% and 17.4% biofouling coverage, respectively, when 2 wt % of nanoparticles were used. Decreasing the concentration of the nanoparticles in the coating formulations resulted in a decrease of their antifouling properties. Among the paints, the best antifouling performance was achieved by paint 1 containing either 2 or 5 wt % of QC18-modified nanoparticles loaded with biocide. Furthermore, the QC18-modified nanoparticles provided better antifouling properties to the coating formulations compared to the QC14-modified nanoparticles.

6.4. General conclusions

The goal of this thesis is to develop novel modified nanoparticles as functional fillers for low toxic and environmentally friendly antibacterial/antifouling coatings for mobile and stationary applications in maritime, hospitals, etc. According to our approach, spherical mesoporous silica nanoparticles were synthesised, surface-modified by quaternary ammonium salts, loaded with commercial biocide Parmetol S15 and added in pristine coating formulations (specifically designed by Jotun for the BYEFOULING project, without incorporated biocides). The dual-functionalised nanoparticles were characterised by various techniques and the successful surface modification and biocide encapsulation were confirmed. The synthesised materials presented excellent antibacterial properties in powder form by killing all the exposed bacteria at the end of the tests. The work on the development of functionalised mesoporous silica nanoparticles with dual antibacterial properties was summarised in a publication featured in the journal *ACS Applied Materials & Interfaces* entitled *"Modified Mesoporous Silica Nanoparticles with a Dual Synergetic Antibacterial Effect"* (DOI: 10.1021/acsami.7b14642).[1]

Afterwards, the functionalised fillers were added homogeneously in coating formulations. The nanocontainer-doped paints showed good distribution of the functionalised nanocontainers in the coating matrix, increased hydrophobic surfaces and similar roughness values with the pristine coating formulation. Furthermore, the dual functionalised nanoparticles provided excellent anti-macrofouling properties to the paints and, at the same time, low toxicity against non-target species (mussels and brine shrimps). Finally, the formulated nanocontainer-loaded paints were applied on

PVC panels and exposed in field test trial. After six months of exposure in natural sea water conditions, the treated panels presented excellent antifouling properties and significantly lower biofouling coverage compared to the pristine coating formulation. The work on the development of nanocontainer-doped paints including their antibacterial, antifouling properties and their toxicity on non-target species was summarised in a recently submitted manuscript in the journal *Advanced Functional Materials* entitled *"Highly Effective Multifunctional Coatings Based on Functionalised Nanoparticles with Antibacterial and Antifouling Properties"*.[2] Furthermore, the output of our work was presented in several international conferences either as oral or poster presentations.[3-8]

Through our approach, we demonstrated for the first time a facile and effective formulation of antibacterial/antifouling paints containing innovative modified nanoparticles with dual functionalities in one pot. The combination of the surface modification of mesoporous silica carriers with their impregnation with conventional green biocide provides both passive (due to the covalently attached QAS) and active (due to the release of the encapsulated biocide) antifouling protection. Our novel paints combine two traditional approaches (biocide-releasing and not-biocide-releasing) of the current commercially available coatings in one formulation. The covalently attached QASs on the surface of the nanoparticles remain active even after complete release of the biocide, which considerably increases their functional lifetime in the coating formulations.

References

[1] M. Michailidis, I. Sorzabal-Bellido, E. A. Adamidou, Y. A. Diaz-Fernandez, J. Aveyard, R. Wengier, D. Grigoriev, R. Raval, Y. Benayahu, R. A. D'Sa, D. Shchukin, *ACS Appl. Mater. Interfaces* **2017**, *9*, 38364.

[2] D. S. M. Michailidis, E. Gutner-Hoch, R. Wengier, R. C. A. Onderwater, R. A. D'Sa, Y. Benayahu, *Adv. Funct. Mater.* **2018**, *recently submited manuscript*.

[3] M. Michailidis and D. Shchukin. Antimicrobial activity of quaternary ammonium-grafted MCM-48 and loaded with biocide. Summer School on Organic Electronics from Semicontactor to Biomolecular Interfaces, 14-18 September 2015, Como, Italy (*poster presentation*).

[4] M. Michailidis and D. Shchukin. Antibacterial coatings containing modified nanoparticles with dual antimicrobial effect. University of Liverpool PhD poster day, 15th December 2016, Liverpool, UK (poster presentation).

[5] M. Michailidis and D. Shchukin. Antifouling coatings containing modified nanoparticles with dual antimicrobial effect. 18th International Congress on Marine Corrosion and Fouling, 19-24 June 2016, Toulon, France (*oral presentation*).

[6] M. Michailidis, E. Gutner-Hoch, B. Benayahu and D. Shchukin. Antifouling-Antibacterial coatings containing modified mesoporous silica nanoparticles with dual effect. 7th International Colloids Conference, 18-21 June 2017, Barcelona, Spain (*poster presentation*).

[7] M. Michailidis and D. Shchukin. Antifouling/antibacterial coatings containing modified mesoporous silica nanoparticles with dual effect. 13th International Conference on Material Chemistry, 10-13 July 2017, Liverpool, UK (*oral presentation*).

[8] M. Michailidis and D. Shchukin. Antifouling/antibacterial coatings containing modified mesoporous silica nanoparticles with dual effect. Postgraduate Symposium, 12th January 2018, Liverpool, UK (*oral presentation*).

Chapter 7: Further Work

7. Further work

Mesoporous silica nanoparticles have been used extensively in the literature for several application. These materials provide great potential for dual functionalisation, especially for biomedical applications; active surface due to the existence of the –OH groups and high pore volume for encapsulation. In our studies, we demonstrated an effective way to produce dual functionalised NPs for long term antibacterial/antifouling applications by using active compounds with established effectiveness. For the surface modification, we used two different types of QASs and for the encapsulation a commercially available biocide. Nevertheless, there is a broad selection of antibacterial/antifouling compounds currently available that can be used either for the surface modification or for the encapsulation. For the surface modification either hydrophobic or hydrophilic compounds can be used and similarly for the encapsulation since the available effective antibacterial/antifouling compounds on the market can be either hydrophobic or hydrophilic compounds.

In this work, the amount of the encapsulated biocide in the functionalised NPs was determined as a percentage via TGA measurements. Other techniques such as UV-Vis can be used in order to determine the encapsulation efficiency of the biocide in the mesoporous nanocontainers and the biocide release rate for different time periods in various liquid media.

Additionally, the idea of using dual functionalisation in one material could be used in handling two different problems in the same application. For example, two major problems in maritime applications are biofouling and corrosion. It could be of great interest to modify the surface of MSNs with antifouling compounds and encapsulate

in the modified materials anticorrosion compounds. In that way, the dual-functionalised materials would provide both antifouling and anticorrosion protection to the final application.

Furthermore, in order to investigate if there is size-dependency at the antibacterial properties, we synthesised and surface modified MSNs with two different sizes. Our findings provided some evidence that the smaller the modified NPs the higher the antibacterial properties. However, we used only two sizes of modified NPs and only two types of QASs for the surface modification. Therefore, other researches could find interesting to use a broader range of nanoparticles' size and a broader range of compounds for the surface modification in order to prove further and establish the size-dependency at the antibacterial properties.

The main results documented in this thesis are disseminated in the following publications and conference presentations.

Publications directly associated with this Thesis:

- **M. Michailidis,*** I. Sorzabal-Bellido, E. A. Adamidou, Y. A. Diaz-Fernandez, J. Aveyard, R.Wengier, D. Grigoriev, R. Raval, Y. Benayahu, R. A. D'Sa and D. Shchukin.* Modified Mesoporous Silica Nanoparticles with a Dual Synergetic Antibacterial Effect. *ACS Applied Materials & Interfaces*, 2017, 9, 38364−38372.

- **M. Michailidis**,* E. Gutner-Hoch, R. Wengier, R. C. A. Onderwater, R. A. D'Sa, Y. Benayahu, D. Shchukin.* Highly Effective Multifunctional Coatings Based on Functionalised Nanoparticles with Antibacterial and Antifouling Properties. *Recently submitted manuscript to Advanced Functional Materials*.

Conference presentations directly associated with this Thesis:

- **M. Michailidis** and D. Shchukin. Antimicrobial activity of quaternary ammonium-grafted MCM-48 and loaded with biocide. Summer School on Organic Electronics from Semicontactor to Biomolecular Interfaces, 14-18 September 2015, Como, Italy (*poster presentation*).

- **M. Michailidis** and D. Shchukin. Antibacterial coatings containing modified nanoparticles with dual antimicrobial effect. University of Liverpool PhD poster day, 15th December 2016, Liverpool, UK (poster presentation).

- **M. Michailidis** and D. Shchukin. Antifouling coatings containing modified nanoparticles with dual antimicrobial effect. 18th International Congress on Marine Corrosion and Fouling, 19-24 June 2016, Toulon, France (*oral presentation*).

- **M. Michailidis**, E. Gutner-Hoch, B. Benayahu and D. Shchukin. Antifouling-Antibacterial coatings containing modified mesoporous silica nanoparticles with dual effect. 7th International Colloids Conference, 18-21 June 2017, Barcelona, Spain (*poster presentation*).

- **M. Michailidis** and D. Shchukin. Antifouling/antibacterial coatings containing modified mesoporous silica nanoparticles with dual effect. 13th International Conference on Material Chemistry, 10-13 July 2017, Liverpool, UK (*oral presentation*).

- **M. Michailidis** and D. Shchukin. Antifouling/antibacterial coatings containing modified mesoporous silica nanoparticles with dual effect. Postgraduate Symposium, 12th January 2018, Liverpool, UK (*oral presentation*).

Publications arising from work conducted during the course of this Thesis but not directly associated with it:

- Z. Zheng, Z. Chang, G.-K. Xu, A. Ho, F. McBride, Z. La, M. Michailidis, W. Li, R. Raval, R. Akhtar and D. Shchukin. Encapsulated phase change materials in solar-thermal conversion systems: understanding geometry-dependent heating efficiency and system reliability. *ACS Nano*, 2017, 11, 721-729.

- E. A. Adamidou, A. Smith, M. Michailidis, F. Blanc, D. Shchukin and A. F. Miller. Towards PEO-PPO-PEO block copolymer drug delivery: interaction with lipid vesicle membrane. *Manuscript in preparation*.

- E. A. Adamidou, A. Smith, M. Michailidis, A. F. Miller. PEO_{13}-PPO_{30}-PEO_{13} and hybrid PEO_{13}-PPO_{30}-PEO_{13}/lipid drug delivery devices for the delivery of paclitaxel. *Manuscript in preparation*